UNDERSTANDING MORPHOLOGY DEPENDENT LUMINESCENCE IN NANOSTRUCTURED SILVER FILMS: EXPERIMENTS, MODELING, AND NUMERICAL SIMULATIONS

by

LAWRENCE JOHN DAVIS III

A DISSERTATION

Presented to the Department of Physics
and the Graduate School of the University of Oregon
in partial fulfillment of the requirements
for the degree of
Doctor of Philosophy

June 2012

DISSERTATION APPROVAL PAGE

Student: Lawrence John Davis III

Title: Understanding Morphology Dependent Luminescence in Nanostructured Silver Films: Experiments, Modeling, and Numerical Simulations

This dissertation has been accepted and approved in partial fulfillment of the requirements for the Doctor of Philosophy degree in the Department of Physics by:

Dr. Hailin Wang	Chair
Dr. Miriam Deutsch	Advisor
Dr. Jens Noëkel	Inside Member
Dr. Stephen Kevan	Inside Member
Dr. Catherine Page	Outside Member

and

Kimberly Andrews Espy	Vice President for Research and Innovation/ Dean of the Graduate School

Original approval signatures are on file with the University of Oregon Graduate School.

Degree awarded June 2012

DISSERTATION ABSTRACT

Lawrence John Davis III

Doctor of Philosophy

Department of Physics

June 2012

Title: Understanding Morphology Dependent Luminescence in Nanostructured Silver Films: Experiments, Modeling, and Numerical Simulations

In this dissertation we use theoretical, computational, and experimental techniques to investigate the influence of structure and environment on the optical properties of nanoscale silver films. We have focused our study on two types of nanoscale films, those being smooth films with nanoscale thickness and chemically deposited nanostructured films. We examine the excitation of surface plasmon resonances in both types of films and study the sensitivity of these resonances to the film structure and the properties of the surrounding dielectric environment.

Using smooth films we discuss the development of methods for measurement of fluid temperature and thermo-optic coefficients based on the sensitivity of surface plasmon excitations to film thickness and permittivity of the adjacent dielectric. We then examine the role of film microstructure in determining the photoluminescent properties of chemically deposited rough silver films. We develop a physical model to describe the chemical deposition process used to fabricate the films. We also

develop a Monte Carlo algorithm to simulate the film deposition and test the model. We validate the model and simulations by comparing simulated and measured structural properties of the films across a wide range of film morphologies. We examine the dependence of the ensemble photoluminescence and surface enhanced Raman scattering on the film structure and excitation power. Our experimental and computational study of film growth and morphology allows us to understand how these light emission signals are influenced by the film microstructure. We also discuss how these signals and their sensitivity to the film microstructure and dielectric environment might be exploited for biochemical sensing applications.

CURRICULUM VITAE

NAME OF AUTHOR: Lawrence John Davis III

GRADUATE AND UNDERGRADUATE SCHOOLS ATTENDED:

University of Oregon, Eugene, Oregon
Pacific University, Forest Grove, Oregon

DEGREES AWARDED:

Doctor of Philosophy in Physics, 2012, University of Oregon
Bachelor of Science in Physics, 2005, Pacific University

AREAS OF SPECIAL INTEREST:

Optics of nanoscale metals
Plasmonics
Quantitative analysis and modeling of multi-scale complex systems and structures
Biophysics, Neuroscience

PROFESSIONAL EXPERIENCE:

Instructor, Conceptual Physics
Oregon State Penitentiary, 2012
UCORE Fellow
University of Oregon, 2011
GK-12 Fellow
University of Oregon, 2010 – 2011
Graduate Research Assistant,
University of Oregon, 2008 – 2012
Graduate Teaching Fellow,
University of Oregon, 2005 – 2008

GRANTS, AWARDS AND HONORS:

Oregon Center For Optics Proposal Contest Winner, *Quantitative Characterization of Mouse Search Patterns in Standard Learning and Memory Tests*, University of Oregon, Eugene, OR, 2010

Sigma Chi award (outstanding senior research in the physical sciences), Pacific University, Forest Grove, OR, 2005

Senior male athlete of the year (wrestling), Pacific University, Forest Grove, OR, 2005

PUBLICATIONS:

Lawrence Davis and Miriam Deutsch, "Surface Plasmon Based Thermo-optic and Temperature Sensor for Microfluidic Thermometry" Rev. Sci. Instruments, **81**, 114905, (2010).

ACKNOWLEDGEMENTS

I would like thank my advisor, Miriam for allowing me to explore while watching to make sure I did not get lost. While my path may have been lengthened by taking an exploratory route, I believe my growth as a scientist was increased proportionally.

I would like to thank my fellow students at the University of Oregon for many helpful discussions, for their efforts to maintain a healthy atmosphere in the department, and most of all for their friendship.

I would like to thank my family and closest friends for their constant support of my endevours, both mental and physical, even when they did not completely understand them.

I would like to thank my wife Liz for her unwavering support in all aspects of our life, especially in the months leading up to my defense and departure for Denali.

To the many special people in my life who expressed unwavering confidence that I would someday be writing this dedication.

TABLE OF CONTENTS

Chapter Page

I. INTRODUCTION 1

Origins of Nanoscale Optics 1
The Optical Response of Metals 3
Surface Plasmon Polaritons on Flat Interfaces 6
Coupling to Surface Plasmon Polaritons 8
Evanescent Confinement of Surface Plasmon Polaritons 12
Surface Plasmon Polariton Applications 15
Optical Circuits with Surface Plasmon Polaritons 15
Optical Sensing with Surface Plasmon Polaritons 16
Nonlinear Optics with Surface Plasmon Polaritons 17
Localized Surface Plasmons 17
Electromagnetic Field Enhancement With Localized Surface Plasmons 21
Disordered Plasmonic Nanostructures 23
Localized Surface Plasmon Polariton Applications 25
Near-Field Optical Microscopy 25
Biological Imaging and Sensing 25
Enhancement of Intensity Dependent Optical Processes 26
Surface Plasmon Enhanced Random Lasing 27
Optical Sensing Applications 27
Dissertation Chapter Outline 28

II. SURFACE PLASMON POLARITON BASED THERMO-OPTIC AND TEMPERATURE SENSING IN MICROFLUIDS 31

Introduction 31
Introduction to the Thermo-optic Coefficient 31

Chapter Page
Temperature Measurement in Microscale Fluids 33
Thermo-optic Signals in the Kretschmann Configuration 34
Origins of Thermo-Optic Signals in the Kretschmann Configuration 34
Calculation of Thermo-optic Signals in the Kretschmann Configuration 36
Experimental Setup for Measurement of Liquid Thermo-optic Coefficients 38
Thermo-Optic Sensor Calibration 40
Experimental Measurement of Liquid Thermo-Optic Coefficients 43
Experimental Procedure 43
Data Analysis and Extraction of the Thermo-optic Coefficient 45
SPP Based Microfluid Temperature Measurement 47
SPP Based Temperature Sensing Considerations 47
Detection of SPP Induced Heating 48
SPP Based Thermo-optic and Temperature Sensor Limitations 52
Sensor Range Limitations 52
Probe-induced Heating 53
Fluid Volume Limitations 55
Conclusions 57

III. MEASURING AND MODELING THREE-DIMENSIONAL STRUCTURE OF SILVER TOLLEN'S FILMS 60

Introduction 60
Motivations for Studying the Structure of Silver Tollen's Films 60
Motivations for Modeling and Simulating the Deposition and 3D Structure of Tollen's Films 62
Metallic Film Deposition Simulation Methods 65
Fabrication of Silver Tollen's Films with Varied Morphology 68
Tollen's Film Deposition Model 71
Simulation of Tollen's Film Deposition 74
Analysis of SEM Images 78
Determination of Model Parameters 82

Chapter Page
Modeling and Simulation Results 85
Comparison of Simulated and Measured Tollen's Films 85
The Tollen's Film Growth Mode 90
Determining the 3D Structure of Tollen's Films 91
Conclusions 95

IV. MORPHOLOGY DEPENDENT PHOTOLUMINESCENCE AND RAMAN SCATTERING IN SILVER TOLLEN'S FILMS 99

Introduction 99
Motivations for Studying the Photoluminescence of Tollen's Films 99
Noble Metal Nanostructure Photoluminescence 102
Noble Metal Photoluminescence 102
Blinking Behavior in Photoluminescence and SERS from Noble Metal Nanostructures 105
Temporal Decay in Photoluminescence and SERS from Noble Metal Nanostructures 108
Fabrication and Characterization of Silver Tollen's Films 110
Measurement of Photoluminescence and SERS from Tollen's Silver Films 113
Experimental Setup and Procedure 113
Removal of Background Substrate Luminescence 117
Decomposition of PL and SERS Spectra 120
Power Dependence of PL and SERS in Tollen's Silver Films 123
Morphology Dependences of PL and SERS in Tollen's Silver Films 125
Interface Density as a Predictor of Tollen's Film Emission 129
Conclusions 142

V. CONCLUSIONS 146

Future Work 148
Closing Remarks 151

Chapter Page

APPENDICES 153

A. TOLLEN'S FILM DEPOSITION SIMULATION CODE 153

B. QUANTITATIVE CHARACTERIZATION OF MOUSE SEARCH PATHS IN THE MORRIS WATER MAZE 167

Introduction 167
The Morris Water Maze as a Learning and Memory Test 170
Digitial Image Analysis Methods 175
Results 178
Conclusions 179

REFERENCES CITED 181

LIST OF FIGURES

Figure Page

1.1. Wavelength dependent real and imaginary parts of the silver dielectric functions from tabulated values [20]. 6
1.2. Diagram of surface plasmon polariton propagation at a flat metal-dielectric interface. The associated electric field are shown decaying into the adjacent media, while the magnetic field lies parallel to the interaface and perpendicular to the propagation direction. 7
1.3. Dispersion relation of a surface plasmon polariton at silver-air and silver-water interfaces calculated using tabulated values for the silver dielectric function [20]. Note the light-SPP momentum mismatch, Δk depicted for the silver water interface at a particular frequency of $\omega = 3000$THz ($\lambda_0 = 628nm.$) 9
1.4. Schematics (not to scale) of the Otto (left) and Kretschmann (right) configurations for coupling incident light to the SPP modes. Dashed lines represent the exponential decay envelopes of the evanescent fields. Note the difference in which interface supports the SPP between the two configurations. 10
1.5. Kretschmann configuration reflectance for light of wavelength 632.8nm plotted as a function of incident angle for several values of the silver film thickness, h and water as the dielectric medium. Tabulated values for the optical constants of silver were used in the calculation [20] 12
1.6. Schematic of light experiencing TIR and its interference with light out-coupled from an SPP excited by the evanescent wave associated with TIR. Dashed lines represent evanescent electric fields. Here we have shown the effect in the Kretschmann configuration. The effect in the Otto configuration is analogous. 13

Figure Page

1.7. Normalized amplitude of the SPP electric field, plotted against the distance from the interface normalized to the free space wavelength, in this case $\lambda = 632.8$nm. The solid line depicts the electric field decay envelope in the silver film while the dashed line shows the field penetration into water as the adjascent dielectric. 14
1.8. Excitation of a LSP on a metal nanosphere with $\epsilon_m < 0$ surrounded by dielectric medium with $\epsilon_s > 0$. 18
1.9. Scattering and absorption cross sections of a silver sphere with 50nm radius in water and in air. 20
1.10. True-color image of chemically deposited silver nanoparticle aggregates under white light illumination, demonstrating the variation in LSP scattering resonance with aggregate size. 21
1.11. The figure on the left shows a schematic cross section of the dipole electric field distribution produced by excitation of an LSP on a metallic nanosphere. The right figure is a scanning electron micrograph of a chemically deposited silver film. Dielectric voids in the film are highlighted by the red circles. 22
1.12. Scanning electron micrographs of chemically deposited silver nanostructures at various stages of growth morphology: (a) disperse nanoparticles, (b) isolated aggregate islands, (c) coalescing islands, (d) fractal (self-similar) films, (e) highly porous connected networks, and (f) semi-continous rough films. All images are the same magnification scale indicated by the scale bar in (a). 24
2.1. Schematic of the Kretschmann configuration (not to scale) for ATR coupling to SPPs at a flat metal-dielectric interface. Notice that the SPP is excited on the opposite side of the metal film from the which the light is incident. The dotted line indicates the direction normal to the interface, $\hat{z}$. Dashed lines represent the evanescent decay envelopes on the normal components of the electric fields. 34

2.2. Panel (a) shows the contribution to dR/dT due to the TO effect in the coupling prism plotted against prism-silver incidence angle θ. Panel (b) shows the contribution due to the TO effect and thickness changes due to thermal expansion in the metal and panel (c) shows the contribution of the TO effect in the test dielectric. All calculations were for $T = 22°C$ using $\lambda = 632.8$nm, $h_0 = 50$nm and liquid ethanol as the test dielectric. Previously published values for n_m, n_d, n_p, μ, α and the TO coefficients of silver, bk7 glass, and ethanol were used in the calculations [20,30,95,110]. 38
2.3. Diagram of the experimental setup excluding the stages to which the brass-prism system is mounted. The diagram is not to scale. Notice the clamp and o-ring system which seals the liquid inside the brass thermal reservoir. 40
2.4. Reflectance as function of incident angle for probe wavelength 632.8nm with ultra-pure water (18.2MΩ-cm resistivity) as the test dielectric at $T = 21.65$°C. Measured values are indicated by dots. The solid curve is the reflectance function obtained by a least-squares fit to the data with ϵ'_m,ϵ''_m and h as parameters. The dashed line denotes the calculated reflectance using tabulated values for the refractive index of silver [20] and $h = 50nm$ measured during deposition. Inset: Angular derivative of the reflectance calculated from the solid curve in the main figure, plotted against incident angle. 42
2.5. Calibration curve for DekTak profilometer allowing for 3nm step-height resolution. We see that actual height is consistently 1.35 times greater than measured by the DekTak for heights greater than $30nm$. 43
2.6. Reflectance as function of temperature for water (main figure) and ethanol (inset). Measured values are denoted by dots and solid traces indicate the fitted theory, which is used to determine the TO coefficient. 45

Figure Page

2.7. Reflectance as a function of incident angle plotted for several values test dielectric refractive index: 1.33 (black), 1.36, (red), 1.39 (blue), and 1.41 (green). The film thicknesses used in the calculations have been adjusted for each value so that only the effect of the increasing refractive index is compared. 49
2.8. Temperature plotted against time showing calculated values (dots) and values measured using the thermometer (triangles). The solid curve denotes a fitted exponential cooling law, with a coefficient of determination $\mathcal{R}^2 = 0.998$. Inset: Non-averaged temperature values obtained from measured reflectance (dots) and fitted exponential cooling law, with coefficient of determination $\mathcal{R}^2 = 0.757$ (solid line). 50
2.9. Reflectance values (raw data) plotted against temperature measured using ethanol as the test dielectric. Inset: Temperature derivative of the reflectance calculated using the theoretical model (solid line) and measured reflectance values from main figure (dots). 53
3.1. Photograph of Tollen's film fabrication setup with samples suspended in the Tollen's reaction solution. The photograph was taken within 1 minute after the start of deposition as indicated by the yellowing of the solution. 69
3.2. Scanning electron micrographs of silver nanoparticles deposited on glass using the the Tollen's method. Panel (a) shows a wide-view image of a sample removed 1.5 minutes after the initial yellowing of the solution. Panels (b)-(e) show high magnification images from a sample removed after 2.5 minutes, where the typical particle size is seen to be roughly $25nm$ 70
3.3. Diagram of the MC-type algorithm for simulation of Tollen's film deposition using example values of G = 1/4 and an S = 1/3. 77
3.4. Comparison of an SEM image of a silver Tollen's film (left) and the boolean image produced by brightness thresholding the image (right). The boolean image represents the 2D normal projection of the film onto the substrate plane. 79

3.5. Conservative estimate of the error in SC measurement due to sample charging, non-uniform illumination, and user bias or error. 80
3.6. The top two pixel islands show the the 4-connected and 8-connected definitions of pixel connectedness. Under the 4-connected definition the set of pixels is counted as two islands. Under the 8-connected definition the pixels are considered as one island. We have used the 4-connected definition in our analysis. The bottom two islands demonstrate how the R_g measurement assesses island compactness. The two bottom islands contain the same number of pixels, but the R_g for the compact island on the left is less than for the spatially extended island on the right. 81
3.7. Dependence of surface coverage on deposition time for experimental films (squares) and simulated films (dots). The red line is a guide to the eye only. The black solid line is an empirical fit to the $SC(t)$ data for $t < 20$ minutes. (Inset) Simulated mass density (filled voxels per unit substrate area) plotted against deposition time (dots) and exponential fit to the data (line) showing exponential growth at early times. 84
3.8. Comparison of SEM images of experimental films (top row) and 2D projections of simulated films (middle row) with equal surface coverage. White pixels represent the silver projection and black are substrate. Three-dimensional renderings of the simulated films are shown in the bottom row. The surface coverage of the films in each column are: column a)0.11, column b)0.56, column c)0.80. The scale of all images is $(3 \times 3)\mu m$ and the viewing angle for the 3D renderings is 14° off-normal. 86

3.9. Comparison of film structural data extracted from simulations and measured using SEM. Horizontal axis for all plots is surface coverage. a)Dependence of average island area on surface coverage for experimental (dots) and simulated (squares) films. b)Dependence of standard deviation in island area on surface coverage for experimental (dots) and simulated (squares) films. c)Dependence of island density on surface coverage for experimental (dots) and simulated (squares) films. d)Radius of gyration to area scaling exponent as a function of surface coverage for experimental(dots) and simulated films (squares) and for randomly filled pixels (triangles). 88
3.10. AFM images of chemically deposited silver thin films with surface coverage 0.24 (left) and 0.80 (right). 92
3.11. Schematic of the AFM tip geometry. The solid lines indicate the actual tip shape and dashed lines are references used to define the tip geometry. The tip is shown interacting with the silver film adjacent to the probe location, an effect which can introduce artifacts in the topography measured by AFM. The actual height h and the height that would be measured by the tip in the illustration, h_{min} are also shown. The boxes represent individual filled voxels in a simulated film and show how h and h_{min} can be calculated for a simulated film given a known tip geometry. 93

3.12. Three-dimensional structural properties as a function of projected 2D surface coverage determined from simulated films. Horizontal Axis on all plots is projected 2D surface coverage. a)Film roughness measured by AFM (triangles), calculated from simulated film (dots), and calculated from simulated AFM scan on simulated film (diamonds). b)Average film thickness measured by AFM (triangles), calculated from simulated film (dots), and calculated from simulated AFM scan on simulated film (diamonds). c)Volume filling fraction. d)Silver surface area per unit substrate area. Note the large variation seen in the measured AFM data demonstrating the difficulty in using AFM for characterization of these films. 96
4.1. Radiative excitation and recombination process resulting in noble metal photoluminescence. 1)Excitation of an electron from d-band to conduction band by an incoming photon. 2)Hole is scattered to wave vector smaller than k_F. 3)Radiative recombination. 103
4.2. Montage of images of a silver Tollen's film under exposure to laser light, demonstrating the flicker behavior of the PL and SERS signal. The time order of the images is left to right and top to bottom. 108
4.3. Time dependence of the combined PL and SERS spectrum at a collection wavelength of $538.8nm$. A decay of the measured power with time as well as flicker behavior are evident in the time series. The inset focuses in on the the data from $1500s - 1600s$ only. 110
4.4. Example boolean image representing the normal projection of a silver island onto the substrate plane. The interface length is highlighted in red. The interface density is defined as the ratio of this length to the total substrate area. 113
4.5. Diagram of the confocal spectroscopy setup used for measurement of PL and SERS in silver Tollen's films. The diagram is not to scale. 115

4.6. Scanning electron microscope images of Tollen's films with overlay representing the $2.6\mu m$ spot diameter of the focused excitation beam. The surface coverage values of the samples are: a)0.11, b)0.36, c)0.56, d)0.70, e)0.80, f)0.95. 117
4.7. Panel (a) shows measured film emission and glass substrate luminescence spectra from films with $SC \leq 0.26$. The bare glass substrate is labeled $SC = 0$ in the figure legend. The arrow indicates the glass luminescence peak at $564nm$, which used to determine the dependence of the glass luminescence power on SC. Panel (b) shows the height of the peak in the glass luminescence at wavelength $564nm$ normalized to the height for a bare glass slide and plotted against surface coverage. We see a linear dependence for $SC \leq 0.25$. Panel (c) shows the spectra in panel (a) after subtraction of the glass luminescence. Panel (d) shows the dependence of the glass luminescence power on excitation power. The connecting lines are a guide to the eye only. 119
4.8. Combined PL and SERS spectra of silver films deposited on glass and on silicon substrates along with the Raman spectrum from the bare silicon and the luminescence spectrum from the bare glass. The sharp lines seen in the samples containing silicon are the silicon Raman lines at wavelengths $547.0nm$ and $560.3nm$ (Raman shifts $515cm^{-1}$ and $1044cm^{-1}$, respectively) .. 121
4.9. Panel (a) shows an example measured spectrum from a silver Tollen's film with surface coverage of 0.42. The black solid line is the measured spectrum normalized to the maximum signal. The SERS peaks are labeled with their environmental contaminant sources on this measured spectrum. The blue dashed line is a 3rd order polynomial fit to the data in the hatched spectral regions away from the peaks, giving the background PL spectrum. The red dotted line is the SERS spectrum obtained by subtracting the fitted PL background from the total signal. 122

4.10. Log(PL Power) (left) and Log(SERS Power) (right) plotted against Log(P_{ex}) at wavelengths 538.8nm (black squares), 573.9nm (red dots) and 580.7nm (blue triangles). The solid lines are fits to the data at each wavelength: 538.8nm (black line), 574nm (red line) and 580.7nm (blue line). 124
4.11. Measured PL and SERS power normalized to peak value in the combined PL and SERS spectrum, and plotted against surface coverage. Panel (a) is the combined PL and SERS power, panel (b) is the PL power only and panel (c) is the SERS power. We see the relative contributions of the PL and SERS power to the total varies with surface coverage and we see a significant peak in both PL and SERS power near $SC \simeq 0.3$. Colors designate wavelength according to the legend in each panel. Connecting lines are a guide to the eye only. 127
4.12. The left panel shows the measured and simulated island number density plotted against surface coverage, showing a turn-over in island density near $SC \simeq 0.2$ due to the onset of coalescence. The sharp drop in island density near $SC \simeq 0.3$ indicates sudden significant coalescence. The right panel shows the measured island size distributions of Tollen's films before and during coalescence. The distributions change dramatically between $SC = 0.33$ and $SC = 0.42$, indicating the relatively sudden occurrence of significant coalescence..... 128
4.13. Scanning electron micrograph of a Tollen's film with $SC = 0.30$ This specific sample produced the largest PL and SERS signals of all samples measured..... 129

4.14. The top figure shows the electric field enhancement countours near two silver particles separated by $2nm$. The contours are shown for a plane that lies along the inter-particle axis and passes midway through the particles. The polarization of the incident electric field was parallel to this plane. The bottom figure shows 3D plots, where the axis perpendicular to the selected contour plane represents the electric field enhancement factor. The figure was taken from reference [197], where the enhancments were calculated for an incident wavelength of $520nm$ using the discrete dipole approximation. 131
4.15. Influence of Tollen's film morphology (controlled by growth time) on the EM field hot spot density. First column are photographs of the films, second column are SEM images, third colum is linear PL emission, and fourth column is nonlinear PL emission. This figure was taken from reference [67]..... 133
4.16. The PL and SERS power normalized to the maximum value measured at each wavelength and plotted against surface coverage. The interface density, ρ normalized to the maximum value measured in all samples is also plotted. The left panel shows the dependence for the PL and the right panel shows the dependence for SERS. We see similar behavior in the PL, SERS, and ρ across all surface coverages with a significant peak near $SC \simeq 0.3$ for all three measurements ... 134
4.17. Log(Normalized PL power) and Log(Normalized SERS power) plotted against Log(ρ). Panel a is PL at wavelengths $538.8nm$, $573.9nm$ and $580.7nm$. Panel (b) is SERS power at wavelengths $573.9nm$ and $580.7nm$ and panel (c) is the $538.8nm$ peak power. The symbols are data and the solids lines are linear fits to the data..... 135

4.18. Self-normalized measured PL and SERS power plotted against SC. The green data in each panel are the emission powers calculated from measured ρ values using a scaling model. Panel (a) shows PL at wavelengths $538.8nm$, $573.9nm$ and $580.7nm$. Panel (b) shows SERS power at wavelengths $573.9nm$ and $580.7nm$ and panel (c) is for the $538.8nm$ SERS peak. 138
4.19. Panel (a) is Log(PL power) plotted against Log(ρ) for samples with $SC < 0.4$. Panel (b) is Log(SERS power) plotted against Log(ρ) for samples with $SC < 0.4$. The solid lines are fits to the data. Panel (c) is Log(PL power) plotted against Log(ρ) for samples with $SC > 0.4$. Panel (d) is Log(SERS power) plotted against Log(ρ) for samples with $SC > 0.4$. 139
4.20. Panel (a) is simulated Log(Normalized Surface Area) plotted against Log(SC) for $SC < 0.4$. Panel (b) is Log(SC) plotted against Log(ρ) for samples with $SC < 0.4$. The solid lines are fits to the data. 141
B.1 The Morris water maze is an opaque pool of water from which the animal is highly motivated to escape via a submerged platform. B) Depicts the average time to locate the platform (black dot) as a function of trial period in typical animals. Typical paths taken by the animals throughout training are shown above the learning curve. C) Typical performance during probe trials reflecting the performance of mice under different treatments that adversely affect the circuitry necessary for learning and memory. D) A test condition indicating that with more intense training other circuitry can compensate. Figure adapted from reference [230]. 171

B.2 Representative Morris water maze probe trial tracks for four separate control (left) and test (right) animals measured in the Washbourne lab. All animals had been trained to locate a platform using visual cues. The quadrants and visual cues are highlighted by the red lines and circles, respectively. In all cases the animal found the former platform relatively directly, however the overall search behavior after passing this location is different between control and test animals. 173
B.3 Panel (a): Two-point distance distributions calculated from the tracks (X, Y, Z) seen in panel (b) and used to calculate the FWHM values of the tracks. Panel (b): Example tracks (X,Y,Z) with values of the FWHM calculated from the distributions in Panel (a). Panel (c): FWHM plotted against normalized NR2B concentration for both mutant and control groups. Figure adapted from reference [229] 177

LIST OF TABLES

Table Page

4.1. Chemical composition of the film surface determined by x-ray photoelectron spectroscopy. 111
4.2. Spectral location of the SERS peaks for an excitation wavelength of $532nm$, together with the Raman shift and adsorbed contaminant sources of the peaks. 123
4.3. PL to P_{ex} and SERS to P_{ex} scaling exponents measured at the wavelengths exhibiting SERS peaks. 125
4.4. PL to ρ and SERS to ρ scaling exponents measured at the wavelengths exhibiting SERS peaks. 139

CHAPTER I

INTRODUCTION

Origins of Nanoscale Optics

Irish scientist Edward Hutchinson Synge sent a brief letter to Albert Einstien in April of 1928. The letter contained a proposal for subwavelength optical imaging based on the collection of light scattered from a gold nanosphere scanned over the surface of a sample [1]. The importance of Synge's idea depends on the fact that conventional optical microscopes are limited in their resolution to roughly half the wavelength of the imaging light, a phenomenon known as the diffraction limit [2]. The wavelengths of visible light range from $400nm$ to $700nm$ [3], meaning that observing structure less than $\approx$ 200nm in size will test the limits of conventional optical microscopes. However, Synge knew that the visible light scattering properties of metal nanoparticles were strongly dependent on the local environment of the particle. He suggested that by scanning a nanoparticle across a sample and measuring changes in the scattered spectrum, information about the sample could be obtained with nanoscale resolution. What Synge had proposed was the first Near Field Scanning Optical Microscope (NSOM), an instrument that would take another five decades to be successfully implimented [1]. In

hindsight Einstien's response that Synge's idea was "essentially unusable" [1] was somewhat pessimistic, considering that nanoscale metallic optics is now a heavily studied, immensely relevant, and continuously growing field and the use of NSOM instruments has become common [4, 5].

Light is the fastest and most efficient way to transport information from the microscale and upward [6], however the diffraction limit prevents visible light from being focused, confined, steered, stored, and amplified at scales below hundreds of nanometers using conventional optics [6–9]. As new technologies such as nanoscale electronic devices emerge and the miniaturization trend continues, the resulting scale gap between nanotechnology and our ability to interact with it using optical technology remains a fundamental problem [10]. However, metallic nanostrucures (MNs) can enhance the light-matter interaction at the nanoscale and below, effectively bridging the device-optics scale gap, whether the device is a subwavelength optical transistor [11, 12], a nanoparticle inside a cancer cell [13], or even a single molecule [14].

The light-matter interaction enhancment seen in MNs arises mainly from the surface plasmon (SP) resonant excitations which occur in the structures. The field of plasmonics has studied the interaction between light at optical wavelengths and MNs for many decades and Edward Synge clearly understood the potential for MNs in 1928. However, the field has grown exponentially over the last few decades [5] due mainly to advancements in nanoscale fabrication and characterization including

electron microscopy, atomic force microscopy, NSOM, electron beam lithography, and chemical synthesis methods [6, 15–18]. The rapid growth of this relatively young field has led to major discoveries and many applications, however it has also left many questions to be answered in order for the discoveries and applications to reach their full potential [12]. In this thesis we present our work to advance understanding of nanoscale metallic optics, an objective made simultaneously possible and necessary by the continued downshifting of the size scale at which the forefront of science and technology operate [6]. Our studies have focused on two types of plasmonic structures in particular, those being thin silver films and disordered nanostructured silver films. Specifically we have studied how optical properties of these film types depend on their structure and environment. We begin the description of our work with a discussion on the fundamentals of nanoscale metallic optics and plasmonics.

The Optical Response of Metals

We begin our discussion of nanoscale metallic optics by examining the metal dielectric function $\epsilon_m(\omega)$, which describes the optical response of the metals. Applying the Lorentz Model [3] to a material with relative permeability equal to one, we can write the equation of motion for a single electron in a harmonic atomic potential with binding frequency ω_0 and driven by an external electric field with

magnitude $E(x,t)$ as:

$$m\left(\frac{d^2x}{d^2t}+\gamma\frac{dx}{dt}+\omega_0 x\right)=-eE(x,t) \tag{I.1}$$

For the case of incident light, the time dependence of the driving field has the form $E(t)=E_0e^{-i\omega t}$. For oscillation amplitudes small compared to the wavelength of the incident light we apply the electrostatic approximation and treat the spatial distribution of the driving field is effectively uniform. We then solve equation I.1 and write the dipole moment due to the displaced electron as:

$$p=-ex=\frac{e^2}{m}\left(\omega_0^2-\omega-i\omega\gamma\right)^{-1}E \tag{I.2}$$

For a material with number densities n_i of electrons with binding frequency ω_i and damping constants γ_i, then we can sum the contributions of all the electrons to arrive at the dielectric function of the material:

$$\frac{\epsilon(\omega)}{\epsilon_0}=1+\frac{e^2}{\epsilon_0 m}\sum_{i=1}n_i(\omega_i^2-\omega^2-i\omega\gamma_i)^{-1} \tag{I.3}$$

Some fraction of the electrons in a metal are not bound in atomic potentials leading to the $\omega=0$ (DC) conductivity of metals. These electrons do interact with the lattice potential of the metal and thus we assign them an effective mass m^* in order to treat them as "free", and having binding frequency $\omega_0=0$ [19]. Assuming the free electrons do not interact with one another and combining the contribution of all the bound electrons, including their interband transitions, into $\epsilon(\omega)_b$ we can separate the free electron contribution to $\epsilon(\omega)/\epsilon_0$:

$$\frac{\epsilon(\omega)}{\epsilon_0}=\epsilon(\omega)_b+i\frac{Ne^2}{\epsilon_0 m^*\omega(\gamma_0-i\omega)} \tag{I.4}$$

This result is known as the Drude Model, where N is the number density of free electrons and γ_0 characterizes the damping due to scattering from lattice defects and vibrations (phonons). From here on we will refer to $\epsilon(\omega)/\epsilon_0$ as the permittivity and write it simply as $\epsilon(\omega)$. We see that for sufficiently high driving frequencies such that $\omega >> \gamma_0$ the permittivity becomes:

$$\epsilon(\omega) \simeq \epsilon_b(\omega) - \frac{\omega_p^2}{\omega^2} \tag{I.5}$$

Where $\omega_p = \sqrt{Ne^2/\epsilon_0 m^*}$ is the plasma frequency, which has a value in the ultra-violet (UV) region of the frequency spectrum for the noble metals commonly used in the study of nanoscale metallic optics, such as silver and gold. When ω is large enough that $\epsilon_b(\omega) > \omega_p^2/\omega^2$ then $\epsilon(\omega)$ becomes positive and the incident light can be transmitted, giving rise to a UV-trasparency in some metals. When ω is still much greater than γ_0, but small enough that $\epsilon(\omega)$ is negative, then the amplitude of the incident electric field decays exponetially into the metal and is almost entirely reflected. Frequencies in the visible range satistfy these conditions on ω such that $\epsilon(\omega) < 0$, which gives rise to the high reflectivity of visble light by metals that we associate with common experience.

With a microscopic picture of the metal permittivity, $\epsilon_m(\omega)$, in hand we will continue with our discussion of nanoscale metallic optics. From here on it will be convenient to decompose the permittivity into the real and imaginary parts and write it as a function of vacuum wavelength, $\lambda = 2\pi c/\omega$, where c is the speed of light in vacuum. In this form we have: $\epsilon_m(\lambda) = \epsilon_m(\lambda)' + i\epsilon_m(\lambda)''$ and we will use tabulated

empirical values taken from reference [20] for any calculations. Figure 1.1. plots these tabulated values for silver and we can see the plasma edge where $\epsilon_m(\lambda) > 0$ near $\lambda = 320nm$. We also see that $\epsilon_m(\lambda)' < 0$ and $|\epsilon_m(\lambda)'| > |\epsilon_m(\lambda)''|$ in the visible spectral region, which will be important to our discussion of surface plasmons.

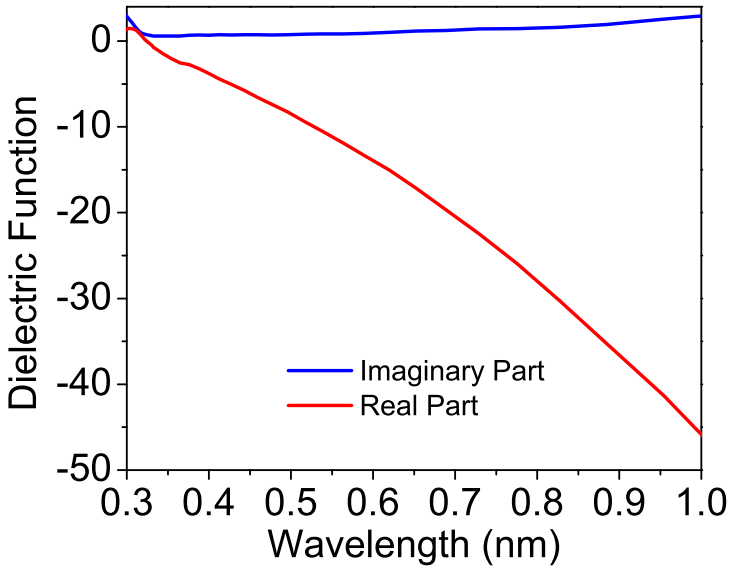

Figure 1.1. Wavelength dependent real and imaginary parts of the silver dielectric functions from tabulated values [20].

Surface Plasmon Polaritons on Flat Interfaces

The collective oscillations of the free electrons in a metal are known as plasmons. The longitudinal volume modes are known as bulk plasmons and the longitudinal surface modes present at the metal-dielectric boundary are known as surface plasmons. Surface plasmon polaritons (SPPs) are surface plasmons coupled to

light. Through this coupling the light is effectively bound to the interface following a dispersion relation modified by the presence of the free electrons in the metal [4]. Figure 1.2. depicts an SPP propogating at a flat interface between a metal and a dielectric with permittivity ϵ_d. The SPP electric field is seen to have components both normal and longitudinal to the propogation direction. The amplitude of the normal components decays exponentially away from the interface. The penetration depth into the dielectric is roughly an order of magnitude larger than into the metal as discussed in the following sections. The magnetic field of the SPP is not depicted as it is parallel to the interface and tansverse to the proagation direction $\hat{k}_x$. The electric field amplitude also decays as the SPP propogates due to damping of the collective electronic oscillations. These fundamental properties of SPPs are discussed below.

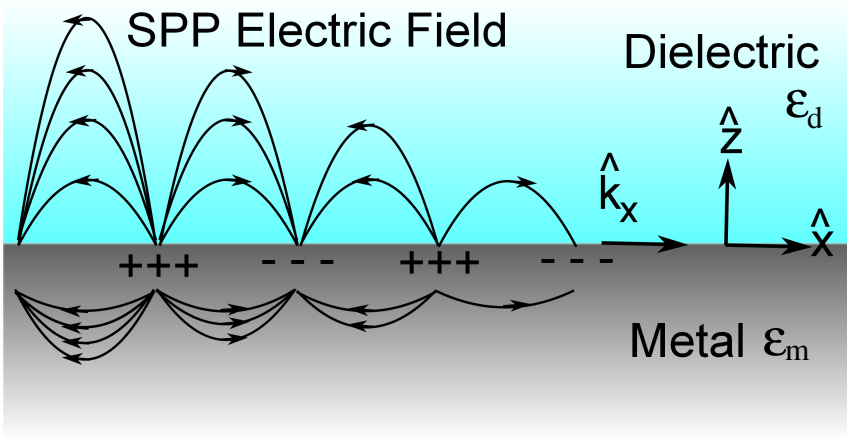

Figure 1.2. Diagram of surface plasmon polariton propagation at a flat metal-dielectric interface. The associated electric field are shown decaying into the adjacent media, while the magnetic field lies parallel to the interaface and perpendicular to the propagation direction.

The dispersion relation for SPPs propagating at the metal-dielectric interface is given by: [21]:

$$k_x = k_0\sqrt{\epsilon_m(\lambda)\epsilon_d/(\epsilon_m(\lambda)+\epsilon_d)} \tag{I.6}$$

Where k_0 is the vacuum wave number, related to the vacuum wavlegth as $k_0 = 2\pi/\lambda$. We can see from equation I.6 that when $\epsilon_m(\lambda) < 0$ and $|\epsilon_m(\lambda)| > \epsilon_d$ then $k_x > k_0$. Here the surface bound nature of the SPP is revealed because the normal component of the SPP wave vector, k_z must then be imaginary in order to satisfy $k_0^2 = k_x^2 + k_z^2$. We see in Figure 1.1. that these conditions on $\epsilon_m(\lambda)$ are met in the visible and near infrared (NIR) regions by metals. While metals other than silver also have $\epsilon(\lambda) > 0$ in the visible region, we have used silver in our work because it exhibits the lowest optical absorption at visible frequencies where our work is focused.

Coupling to Surface Plasmon Polaritons

Direct coupling between free space light and SPPs is prevented by the bound nature of the SPP modes, evident from $k_x > k_0$. Figure 1.3. shows the SPP dispersion relations for both air-silver and water-silver interfaces in the visible and (NIR) frequency range. The momentum mismatch, $k_x - k_0 = \Delta k$ is also indicated for each choice of dielectric and we see that Δk increases with ϵ_d.

The momentum mismatch, Δk can be addressed by either modifying the dispersion relation of the light or by providing additional momentum to the light by scattering from surface features. These methods include attenuated

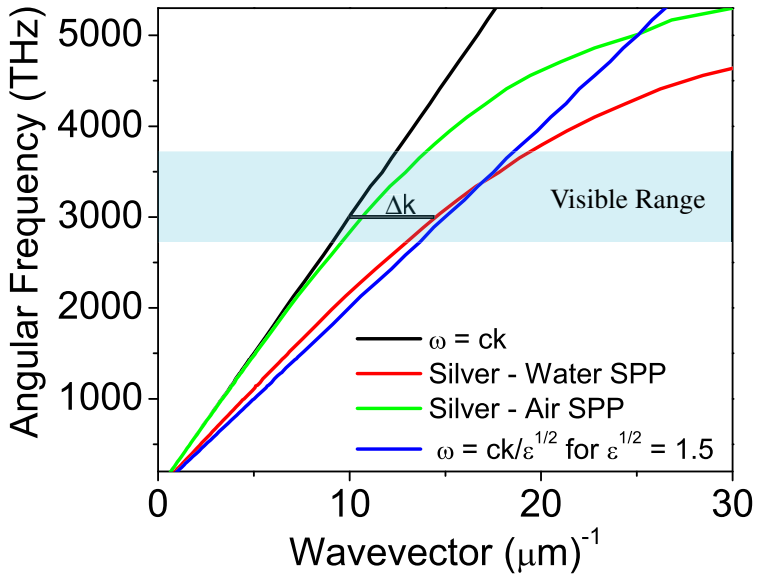

Figure 1.3. Dispersion relation of a surface plasmon polariton at silver-air and silver-water interfaces calculated using tabulated values for the silver dielectric function [20]. Note the light-SPP momentum mismatch, Δk depicted for the silver water interface at a particular frequency of $\omega = 3000\text{THz}$ ($\lambda_0 = 628nm$.)

internal reflection (ATR), grating, roughness, and curvature coupling [4, 21]. More recently, coupling by nonlinear four-wave mixing has been demonstrated [22]. We will discuss the ATR method in detail because we have used this method in our work. There are two common configurations for ATR coupling, known as the Otto configuration and the Kretschmann configuration. Both configurations involve a dielectric coupling prism which modifies the dispersion relation of the incident light from $k_0 = \omega/c$ to $k_0 = \sqrt{\epsilon_p}\omega/c$, where $\epsilon_p > \epsilon_d$ is the permittivity of the prism. This modification is seen in Figure 1.3. as a decreased slope of the light line in the prism. The resulting intersection with the SPP dispersion relation highlights

the opportunity for coupling to the SPP modes. Schematics of both the Otto and Kretschmann configurations are seen in Figure 1.4. and the details of the coupling process will be discussed below.

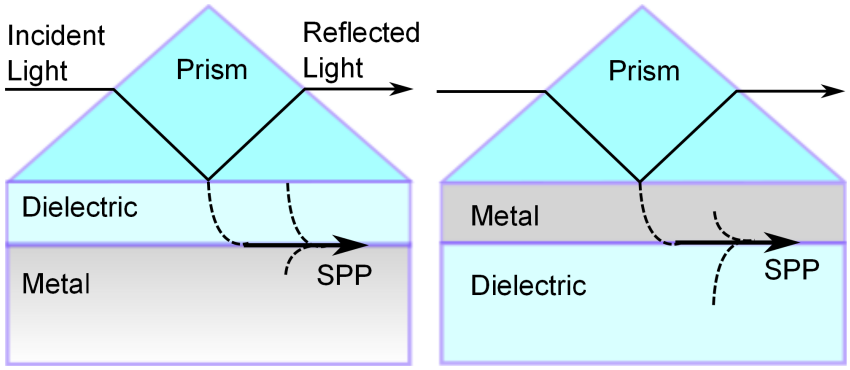

Figure 1.4. Schematics (not to scale) of the Otto (left) and Kretschmann (right) configurations for coupling incident light to the SPP modes. Dashed lines represent the exponential decay envelopes of the evanescent fields. Note the difference in which interface supports the SPP between the two configurations.

The Otto configuration consists of a thin dielectric layer sandwiched between a metal and the coupling prism. When light is incident on the base of the prism at angle θ greater than the critical angle for total internal reflection (TIR), then the light penetrates into the dielectric layer as an evanescent wave while being reflected [3]. For sufficiently thin dielectric layers the evanescent wave interacts with the metal layer below. In this case the SPP dispersion relation can be met by the component of the incident wave vector to the interface: $k_{||} = \sqrt{\epsilon_p} k_0 sin(\theta) = k_x$. The Kretschmann configuration [21] is based on the same principle, only in this case a thin metal film is sandwiched between the prism and the dielectric medium. For sufficiently thin metal films, the TIR associated evanescent wave is able to penetrate

the film and interact with the opposite metal-dielectric interface. As in the Otto configuration, the SPP dispersion relation can be met by the parallel component of wave vector of the reflected light. The dielectric layer in the Otto configuration can be on the order of 100nm, depending on the contrast in ϵ_p and ϵ_d. On the other hand, the metal layer thickness in the Kretschmann setup is limited by the skin depth of the metal, which for commonly used metals such as silver and gold is $\approx (25-50)nm$. We can see from Figure 1.3. and equation I.6 that the wave number where the prism light line intersects the SPP dispersion relation is dependent on the contrast between ϵ_p and ϵ_d. The necessary fine-tuning of the parallel component of the incident wavenumber is achieved by variation of the incident angle θ. The θ which satistfies $k_{||} = \sqrt{\epsilon_p} k_0 sin(\theta) = k_x$ for a particular set of layer permittivities is known as the surface plasmon resonance (SPR) angle, θ_{spp}.

The signature of SPP coupling is evident as a reduction in the reflected light power near θ_{spp}. Figure 1.5. shows the reflectance (ratio of reflected to incident power) from the Kretschmann configuration in Figure 1.4. calculated using the Fresnel method [21]. The reflectance is plotted as a function of incident angle, θ for several metal layer thicknesses, h, highlighting the thickness dependence of the resonance depth.

While the coupling prism allows for light to in-couple to the SPP modes, it also allows for out-coupling of radiation from the SPP modes into the prism. Interference between light which experienced TIR and the out-coupled light results in the

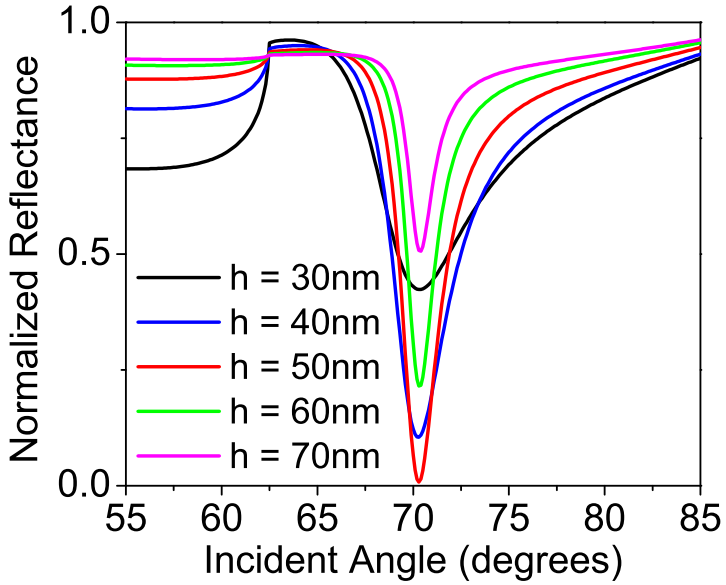

Figure 1.5. Kretschmann configuration reflectance for light of wavelength 632.8nm plotted as a function of incident angle for several values of the silver film thickness, h and water as the dielectric medium. Tabulated values for the optical constants of silver were used in the calculation [20]

.

reflectance dip and the corresponding Fano resonance lineshape [23]. This process is depicted in Figure 1.6. where we can see the phase relationship of the reflected and out-coupled light is dependent on the film thickness. The dependence of θ_{spp} and the reflectance on ϵ_m, ϵ_d, and h provide the basis for SPR based sensing [4, 24], which will be discussed in detail in Chapter II.

Evanescent Confinement of Surface Plasmon Polaritons

The decay coefficients of the electric field component normal to the interface

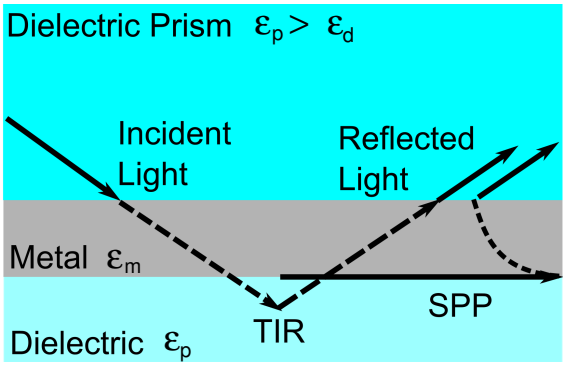

Figure 1.6. Schematic of light experiencing TIR and its interference with light out-coupled from an SPP excited by the evanescent wave associated with TIR. Dashed lines represent evanescent electric fields. Here we have shown the effect in the Kretschmann configuration. The effect in the Otto configuration is analogous.

and extending into the dielectric, γ_d and metal γ_m are calculated as as:

$$\gamma_d = Im\left[\sqrt{\epsilon_d k_0^2 - k_{||}^2}\right] \tag{I.7}$$

$$\gamma_m = Im\left[\sqrt{\epsilon_m k_0^2 - k_{||}^2}\right] \tag{I.8}$$

Figure 1.7. plots the decay of the normal component of the SPP electric field amplitude at a silver-water interface, highlighting the subwavelength nature of SPPs. This evanescent confinement of the SPP field normal to the interface produces a large electric field enhancement at the interface. The intensity ratio of the SPP electric field to the incident electric field at the interface is known as the enhancement factor and is given by [21]:

$$T_{en} = \frac{|\epsilon'_m|^2\sqrt{|\epsilon'_m|(\epsilon_p - 1) - \epsilon_p}}{\epsilon_d \epsilon''_m(1 + |\epsilon'_m|)} \tag{I.9}$$

This enhancement factor can typically be be of order 100. Specifically for a silver film with $h = 50$nm in the Kretschmann configuration with $\epsilon_p = 1.23$ and air as the

dielectric medium the factor is, $T_{en} = 120$. With water as the dielectric, $T_{en} = 70$. Here we see that the larger decay length for greater ϵ_d reduces the enhancement factor. The subwavelength evanescent confinement of SPP fields and the resulting field enhancements will be important to our discussion of SPP applications in the next section.

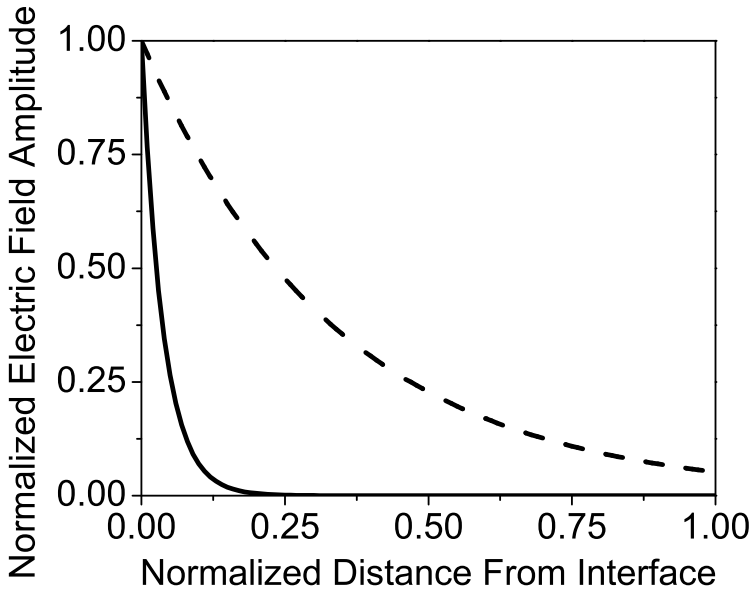

Figure 1.7. Normalized amplitude of the SPP electric field, plotted against the distance from the interface normalized to the free space wavelength, in this case $\lambda = 632.8$nm. The solid line depicts the electric field decay envelope in the silver film while the dashed line shows the field penetration into water as the adjascent dielectric.

Surface Plasmon Polariton Applications

Optical Circuits with Surface Plasmon Polaritons

The subwavelength evanescent confinement of the SPP fields together with the propagating nature of SPPs make them interesting candidates for information carriers in all-optical circuits [6, 7, 12, 25, 26]. Using SPPs to carry information through nanoscale metallic strips or voids may allow for photonic circuits which achieve the information bandwidth of light on the miniature scale of electronics [27]. We have largely moved from electronic to optical methods for long distance information transport. All-optical ciruitry using SPPs to bridge between optical and electronic scales would eliminate the need for optical-electrical conversion [9, 27]. The pursuit of these goals has led to much work in designing plasmonic waveguides and optical elements in order to build up the necessary SPP circuitry components [6, 7, 9, 12, 25–28]. Antagonistic to these goals are several energetic loss mechanisms which limit the propogation length of SPPs to tens of microns at optical frequencies [21]. These loss mechanisms include Ohmic losses in the metal due to decoherence of the driven electron oscillations by scattering from lattice defects and oscillations (phonons), crystal grain boundaries, and surface roughness, [9, 21, 29, 30]. Additionally, radiative losses occur due to the previously mentioned out-coupling of light from SPPs, a process known as radiation damping. [21, 31]. The limits placed on SPP-based circuitry by these

propagation losses have led to significant work on SPP amplification, aiming toward compensation of propogation losses [32–34].

Optical Sensing with Surface Plasmon Polaritons

While SPPs may provide the basis for future subwavelength optical circuitry, currently SPPs are primarily exploited for sensing applications. The concentration of electromagnetic energy at the interface makes SPPs very sensitive probes for changes in ϵ_d, even those occuring on subwavelenth scales [24, 35]. For example, the binding of proteins to the interface will change the local ϵ_d causing a shift in the SPR resonance that depends on the protein concentration. The shift can be detected by monitoring the reflectance of laser light used to excite SPPs on the interface [36]. Biological applications such as protein concentration sensing have dominated the SPR sensing field, and commercial SPR biosensors are now widely available [37]. However, other quantities such as chemical concentration [38, 39] and temperature [40–43] which affect ϵ_d and ϵ_m can also be probed. We have worked to build on previous SPP temperature sensing work to develop a method for accurate determination of temperature and thermo-optic properties of liquids at the microliter scale [44]. This SSP thermometry work will be discussed in detail in Chapter II.

Nonlinear Optics with Surface Plasmon Polaritons

The large electromagnetic (EM) field enhancements produced by SPPs allow for access to non-linear optical processes with relatively low input intensities. Many nonlinear processes have been studied in plasmonic systems, including second harmonic generation [45, 46], third harmonic generation [47], four-wave mixing [48] and Raman scattering [14, 48]. For example, a second order nonlinear optical process such as Raman scattering [49] occuring at a silver-air interface with $T_{en} = 100$ will experience a 10^4 enhancement of the nonlinear signal. This EM intensity enhancemnt by SPPs is a dominant contributor to surface enhanced Raman scattering (SERS) in metallic films, where signal enhancements of 10^{14} have been reported (controversially) and detection of single molecules by SERS has been achieved [14, 48]. These SERS signals and the giant EM field enhancements that produced them [50] were achieved in rough or disordered metallic films supporting Localized Surface Plasmon Polaritons (LSPs) rather than at the smooth interfaces discussed so far. We will now move on to a discussion of LSPs and the EM field enhancements produced in rough and disordered films.

Localized Surface Plasmons

Localized surface plasmon polaritons (LSPs) are charge density oscillations coupled to light at the metal-dielectric interfaces of structures with dimensions comparable to, and often much smaller than, the free-space wavelength [4]. In

contrast to the propogating SPPs at smooth surfaces discussed so far, LPS EM fields are evanescently confined in all three dimentions and do not propagate. The LSP resonance arises due to the restoring forces provided to the oscillating electrons by the curvature of the structures. This allows for curvature coupling of LSPs and free-space light without the need for additional coupling methods [4]. The basic properties of LSPs can be understood by examining the optical response of metallic nanospheres, which naturally support LSP resonances at visible frequencies. Figure 1.8. depicts incident light driving free electron oscillations in a metal nanosphere with permittivity $\epsilon_m(\lambda)$ surrounded by a dielectric medium with permittivity ϵ_s, resulting in LSP excitation. The signatures of LSP resonances are significantly

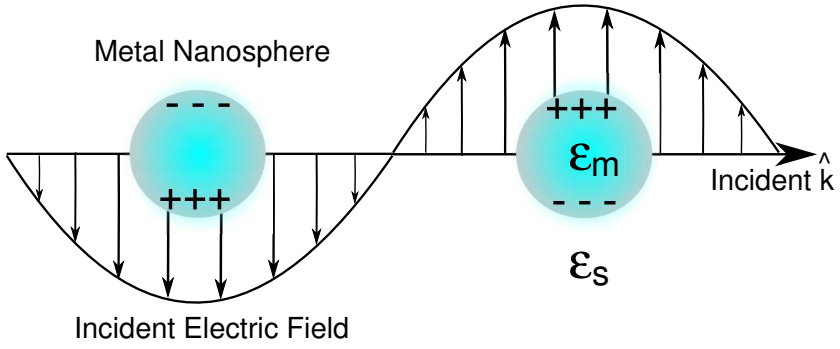

Figure 1.8. Excitation of a LSP on a metal nanosphere with $\epsilon_m < 0$ surrounded by dielectric medium with $\epsilon_s > 0$.

enhanced scattering and absorption cross sections. In general the scattering and absorption cross sections, α_s and α_a respectively, of small particles can be calculated using Mie theory [51]. The fundamental aspects of α_s and α_a for particles supporting LSP resonances can be examined by studying the relatively simple case

of a metallic sphere with radius, r, which is much smaller than the wavelength of the excitation light, λ. When $r << \lambda$ the sphere effectively experiences a uniform EM field across its entire (outer) extent at any moment in time. When the field is treated as spatially invariant, known as the electrostatic approximation, then the Mie theory expressions for α_s and α_a are reduced to [51]:

$$\alpha_s = \frac{8\pi}{3} k_0^4 r^6 \left| \frac{\epsilon_s - \epsilon_m}{\epsilon_s + 2\epsilon_m} \right|^2 \tag{I.10}$$

$$\alpha_a = 4\pi k_0 r^3 Im \left[\frac{\epsilon_s - \epsilon_m}{\epsilon_s + 2\epsilon_m} \right] \tag{I.11}$$

Here k_0 is the free space wave number of the incident light and ϵ_m is the complex metal permittivity. For many purposes, including our discussion of LSP resonances, the electrostatic approximation is adequate for nanospheres up to $r = 100nm$ [4]. Figure 1.9. shows α_s and α_a for a silver sphere with $r = 50nm$ in air and in water, normalized to the physical cross section of the particle, πr^2. We see that α_s and α_a can be larger than the physical cross sections and that the resonance peaks are red-shifted with increasing ϵ_s.

Recalling that $\epsilon'_m < 0$ at wavelengths longer than 320nm [20], the origin of the scattering and absorption peaks in Figure 1.9. becomes clear, as there is a scattering resonance in I.10 when $\epsilon'_m = -1/2\epsilon_s$. The relatively large values of α_a and α_s for plasmonic particles, together with the dependence of α_a and α_s on the local ϵ_s provided the basis for the revolutionary microscope proposed by Synge in 1928 [1]. Synge understood that a single plasmonic nanoparticle would be able to scatter a measureable amount of light from an illuminating beam in a way that was

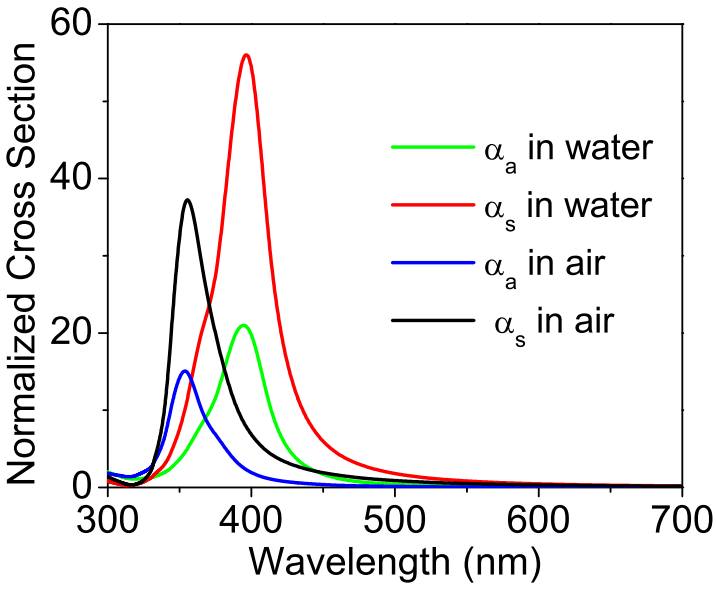

Figure 1.9. Scattering and absorption cross sections of a silver sphere with 50nm radius in water and in air.

dependent on the local (subwavelength) environment of the particle [1]. Figure 1.10. shows a true-color image of chemically deposited silver nanoparticle aggregates on a glass slide under illumination by white light. The size of the aggregates is on the order of $50nm$, which is well below the diffraction limit of visible light. However, the particles are easily detected due to their relatively large scattering cross sections. The scattering resonance of nanoparticle aggregates is redshifted relative to single nanoparticles and the redshift increases with aggregate size. The variations in particle color seen in the image are due to the sensitivity of α_s on aggregate size and shape, an effect which demonstrates the tunability of α_s.

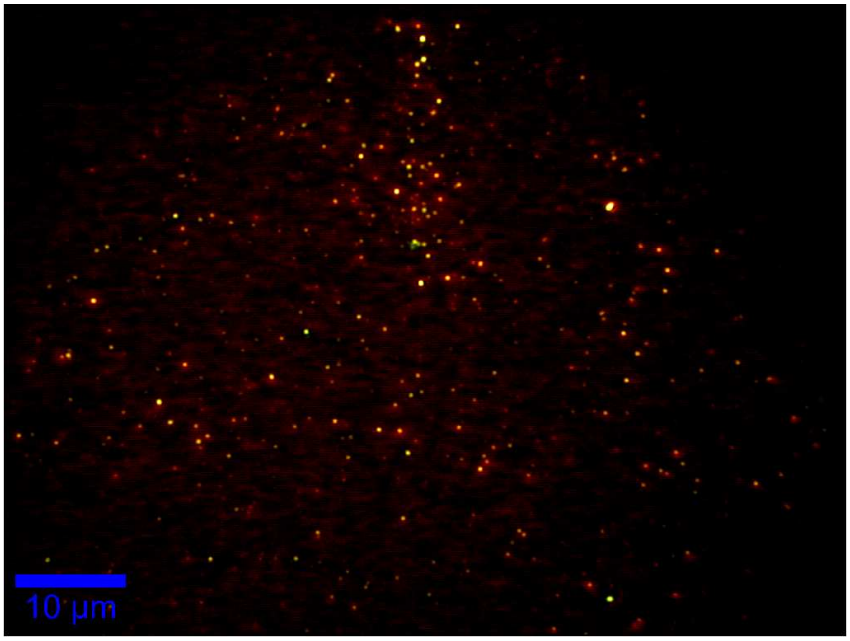

Figure 1.10. True-color image of chemically deposited silver nanoparticle aggregates under white light illumination, demonstrating the variation in LSP scattering resonance with aggregate size.

Electromagnetic Field Enhancement With Localized Surface Plasmons

The exponential confinement of the LSP EM field to the metal dielectric interface enhances the EM field intensity near the structure relative to the excitation intensity [4]. For particles with $r << \lambda$ satisfying the electrostatic approximation, the intensity distribution of the evanescent LSP field is that of a simple dipole. Figure 1.11. depicts this dipole field arising from charge separation in a metallic nanosphere. Additionally, subwavelength dielectric voids in a surrounding metal medium can also support LSP excitations known as gap plasmons or void plasmons [52]. Figure 1.11. shows a scanning electron micrograph (SEM) of a nanostructured silver film containing dielectric voids. The EM field

enhancements associated with void plasmons can be even greater than those of LSP excitation in metal nanoparticles of the same dimensions because the negative curvature of the metal surface concentrates the evanescent EM field energy inside the void [52, 53]. Furthermore, the non-resonant lightning rod effect is known to

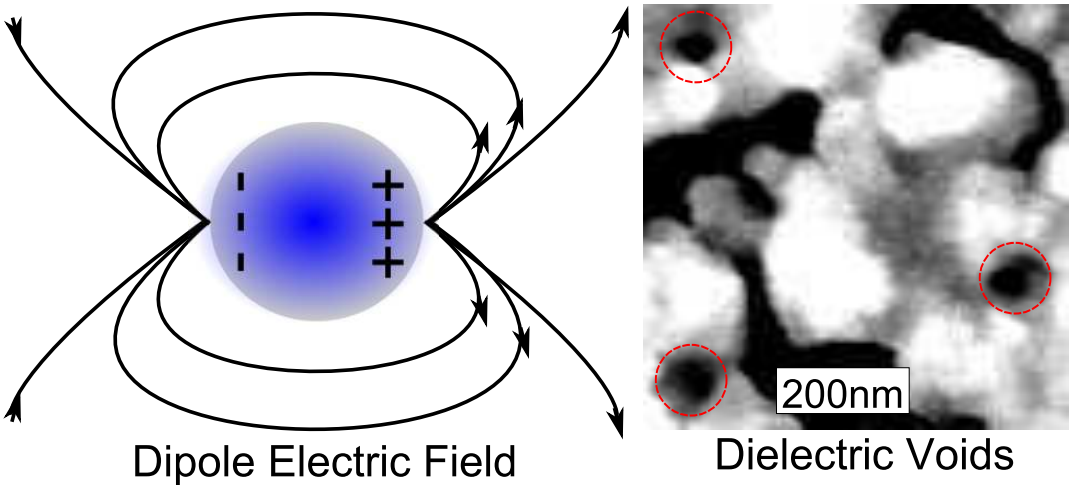

Figure 1.11. The figure on the left shows a schematic cross section of the dipole electric field distribution produced by excitation of an LSP on a metallic nanosphere. The right figure is a scanning electron micrograph of a chemically deposited silver film. Dielectric voids in the film are highlighted by the red circles.

produce EM field enhancement factors of order 100 where large aspect ratios or sharp edges spatially confine oscillating electrons to produce regions of high charge density [54]. These effects make plasmonic nanostructures excellent candidates for use in applications which rely on high EM field intensity and large EM field gradients such as SERS and optical trapping, respectively [54, 55]. However, additional EM field enhancements may occur due to plasmon coupling and wave localization in multiparticle and/or highly structured systems [56–59]. When plasmonic structures are located within the near-field region of one another their

charge density oscillations are no longer independent, leading to a coupling of their respective LSP resonances [4, 56]. As with any capacitive system, the large charge densities in the conducting structures separated by a thin dielectric will produce high electric field intensity between the structures. This effect can produce enhancement factors of order 10-20 [56]. As a result of this coupling, ordered arrays of plasmonic nanoparticles or voids will create well defined regions of high EM field intensity, which can be very useful for applications such as particle trapping [55] and subwavelength lithography [60].

Disordered Plasmonic Nanostructures

Our study has focused on the study of disordered arrays and aggregates of plasmonic nanostructures. These materials provide the added advantages of being relatively easy, fast, and inexpensive to fabricate compared to ordered arrays [61]. Additionally, these materials can produce even greater EM field enhancements than ordered arrays and single particles due to wave localization phenomena which arise in highly scattering disordered media [50, 59, 62–66]. Difficulty in predicting and controlling the exact optical properties of disordered metallic nanostructures has left many open questions to be answered [67] and we will address a subset of these questions in our work to relate photoluminescence (PL) and structural properties in these systems.

We have used chemically deposited nanostructured silver films in our study

because they have become a popular model system for studying nanoscale plasmonics [16] and are currently used for applications such as fluorescence enhancement [68] and (SERS) [61, 69]. These films can have morphologies which include disperse nanoparticles, isolated aggregate islands, fractal[1] structures, highly porous connected networks, and semi-continuous rough films with high porosity. [70]. Figure 1.12. shows SEM images of these films across this range of morphologies. Our work on structural characterization and development of a film deposition model in order to improve our understanding of the structural and optical properties of these films is detailed in Chapter III.

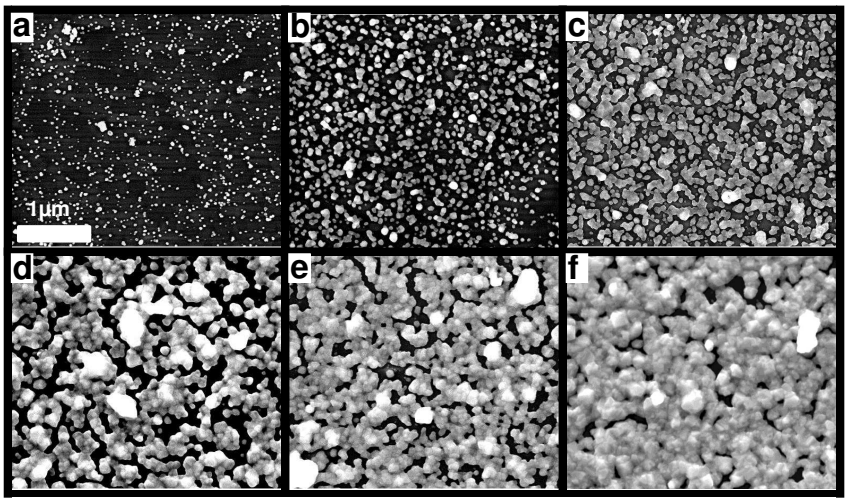

Figure 1.12. Scanning electron micrographs of chemically deposited silver nanostructures at various stages of growth morphology: (a) disperse nanoparticles, (b) isolated aggregate islands, (c) coalescing islands, (d) fractal (self-similar) films, (e) highly porous connected networks, and (f) semi-continous rough films. All images are the same magnification scale indicated by the scale bar in (a).

[1]We will refer to films which show statistical self-similarity across multiple length scales as fractal films.

Localized Surface Plasmon Polariton Applications

Near-Field Optical Microscopy

The modern implementations of Synge's proposed microscope are called near-field scanning optical microscopes (NSOM) because they probe evanescent EM fields which decay exponentially away from the interfaces supporting them [71]. Typical modern implementations of NSOM collect light scattered away from the evanescent EM fields in a sample by a subwavelength plasmonic structure, providing information on the distribution of the evanescent fields. This information can then be analyzed to determine subwavelength optical and structural properties of the sample. Other configurations excite LPSs on metallic nanostructures and then collect light scattered away from the evanescent EM field of the LSP by structure in the sample [18]. The subwavelength optical and structural information provided by NSOM has been used to gain deeper understanding of material properties for materials science [72], biological [73], and plasmonic [64] applications.

Biological Imaging and Sensing

In addition to the local environment, the LSP resonances of metallic nanostuctures are dependent on the size, shape, and optical constants of the metal. This allows for control over the resonant absorption and scattering spectra of LSP systems. For example, the LSP resonance of a silver nanoparticle can be shifted from the

blue to the red by only a change in shape [74]. The size of α_a and α_s relative to the physical size of plasmonic particles together with their tunability provide the basis for a variety of applications. These include biological imaging where a relatively large α_s allows nanoparticles to serve as non-intrusive optical markers [75] and photothermal cancer therapy where the relatively large α_a of nanoparticles allows for efficient conversion of optical energy into thermal energy within cancer cells [13].

Enhancement of Intensity Dependent Optical Processes

The various EM field enhancement mechanisms discussed so far all contribute to the production of subwavelength regions of very high EM field intensity, also known as "hot spots". These hot spots have been used to enhance the fluorescence of quantum dots and organic molecules as well as increase photovoltaic efficiency [68, 76–83]. Hot spot are especially suited for enhancement of nonlinear processes such as multiphoton photoluminescence and harmonic generation [67, 84]. These hot spots have also been exploited to observe single molecule SERS [14] and much work has gone into studying structural morphologies which maximize hot spot intensity for SERS applications [14, 48, 61].

Surface Plasmon Enhanced Random Lasing

Multiple scattering events in a highly scattering medium can increase the interaction length between light and a source of optical gain in the medium, leading to lower lasing thresholds. Additionally, closed loop scattering paths formed in the scattering gain medium may allow for coherent (resonant) feed-back leading to random lasing [65]. Wave localization due to subwavelenth scale fluctations in the optical constants of the medium can lead to lower random lasing thresholds by simultaneously providing feed-back and enhancing the local field intensity[62, 63]. Typically for dielectric particles the maximum packing density is reached before the medium is sufficiently scattering for these effects to occur, however the relatively large α_s of plasmonic nanoparticles can lead to random lasing at relatively low particle densities [85]. While absorption in plasmonic nanostructures reduces their effectiveness in random lasing applications, their large scattering cross sections overshadow this drawback, making them the go-to materials for random lasing applications [65, 85–88].

Optical Sensing Applications

The LSP resonances of metallic nanostructures are dependent on the local permittivity of the surrounding medium and changes to this can be detected by monitoring the scattering or transmission of light in the materials. This allows

for optical sensing of biological agents [89, 90], chemical concentration [91], and temperature [92]. Additionally, metallic nanostructures are known to exhibit photoluminescence that is dependent on the EM field enhancement mechanisms discussed previously. Consequently the PL signal is dependent on the geometry of the nanostrucure and the local environment through the LSP resonance. This effect holds potential for use in optical sensing [4, 67, 93]. This optical sensing potential will be discussed futher in Chapter IV where we present our work to link structural and optical properties of disordered metallic films.

Dissertation Chapter Outline

In chapter I we have introduced the basic optical properties of metallic nanostructures, beginning from a microscopic description of the optical response of metals. We then discussed surface plasmon polariton excitions in metal thin films, metal nanoparticles, and disordered metal nanostructures. Finally we presented a subset of the many optical applications that rely on metallic nanostructures. In light of the many applications based on SPPs and LSPs it is not surprising that the field of plasmonics has grown exponentially over the last decade [5]. Specifically, optical sensing has emerged as a major motivation for the study of SPPs and LSPs in general, with applications in biochemical sensing leading the charge [24, 35, 94]. The suitability of SPPs and LSPs for optical sensing comes from the sensitivity of these resonances to the geometry and local environment of the metal structures

supporting the plasmonic excitations. This dissertation is based on our study of the details governing these sensitivities in two separate plasmonic systems. The first system was the Kretschmann configuration, for which we have examined the sensitivity of SPPs to the temperature dependent thickness of the metal film and permittivities of the prism, metal film, and adjacent dielectric. The second system was chemically deposited nanostructured metal films. We have used experiments, modeling, and simulations to investigate the morphology of this system. We then determined how the ensemble photoluminescence and SERS signals are influenced by microstructure dependent LSP excitations. The outline for the discussion of our work in this dissertation is presented below.

In chapter II we discuss the details of SPR sensing and present our work to improve upon existing SPR sensing techniques by examining the factors limiting SPR sensor resolution. This work is done in the context of optical thermometry in microfluids. We examine and experimentally address some fundamental limitations of optical thermometry by exploiting SPR sensing methods. We then discuss the optimization of our optical detection scheme for highly accurate thermal characterization of microfluids. We present the results of these experiments and examine the sensitivity and limitations of our methods. Finally we examine the potential for applying the methods we have developed to thermal characterization of nanoscale systems.

In Chapter III we present our study of morphology dependent photoluminescence

(PL) in chemically deposited nanostructured silver films. In order to characterize the relation between PL and film structure we measured structural and optical properties across a wide range of morphologies under controlled conditions [67]. This significant undertaking was divided into two parts, the first being structural characterization of the films. Chapter III first introduces the methods we used for fabrication, characterization, modeling, and simulation of the 3D film structure. Then we compare measured structural properties to simulations based on our model and evaluate the accuracy of the model.

Chapter IV addresses the second part the structure-optics challenge. We discucss our measurement of PL and SERS signals from nanostructured silver films across a wide range of morphologies. We then work to relate the PL and SERS signals of the films to specific, measurable structural properties. Application of the knowledge gained in our study of the film structure, discussed in Chapter III, allows us to understand these dependences in terms of EM field enhancement. Finally we will discuss how our study relates to the process of tuning and exploiting the film PL and Raman signals for sensing applications. We will specifically describe a method for biochemical sensing with these films and discuss the optimized film structure for such an application based on our results.

In Chapter V we conclude with a summary of our study followed by a discussion of future work that might follow from our experimental results and the investigative methods we developed.

CHAPTER II

SURFACE PLASMON POLARITON BASED THERMO-OPTIC AND TEMPERATURE SENSING IN MICROFLUIDS

Introduction

Introduction to the Thermo-optic Coefficient

In this chapter we discuss the development of a surface plasmon resonance (SPR) based method for accurate determination of the thermo-optic (TO) coefficient of fluids. Our method is specifically designed to work with fluid volumes less than $100\mu L$ (microfluids). The TO coefficient characterizes the dependence of a material's refractive index, n on temperature, T and is defined as dn/dT. Accuracy in measuring fluid TO coefficients is becoming increasingly necessary in refractive index (RI) sensing applications where the TO effect is often a primary source of noise. For example, SPR-based refractive index sensors similar to the one employed here have recently been implemented with resolution of 1×10^{-7} refractive index units (RIU)[38]. At this level of RI resolution the TO coefficients of some commonly used materials are large enough that temperature changes of 1×10^{-3} °C will cause significant TO induced errors. Water is an example of just such a material and

widely used bio-chemical RI sensors which typically probe water-based solutions are subject to these TO induced errors. However, with accurate knowledge of TO coefficients and accurate determination of temperature it may be possible to correct for the TO-induced error and eliminate the need for such precise temperature control.

Various optical methods such as thermoreflectance measurements [95] and the minimal deviation method [96] have been previously used for measuring TO coefficients of liquids. However, due to limitations of many experimental setups, the systems are not always in thermal equilibrium. The resulting temperature gradients may hinder accurate determination of TO coefficients because measurements of n and T do not necessarily overlap in space and/or time. Due to this separation additional modeling of thermal transport processes is often necessary in order to account for thermal gradients [97, 98]. These additional sources of error may contribute to the spread in reported TO values, which can be as high as 10%, even for well characterized and commonly used materials such as ethanol [95]. We have addressed these issues by utilizing fluid sample volumes in the microliter range embedded in a thermal reservoir. This setup significantly reduces equilibration times and thermal gradients during TO coefficient determination. Overall, the apparatus and procedure discussed in this chapter were specifically designed to mitigate the technical challenges and limitations of TO measurement to allow determination of TO coefficients with accuracy better than 1×10^{-5} $^{\circ}\mathrm{C}^{-1}$.

Temperature Measurement in Microscale Fluids

In this chapter we will also discuss the use of our setup for SPP-based optical temperature sensing, an effort primarily motivated by the widespread growth in lab-on-chip technologies which require microscale temperature sensing [99–102]. Such technologies include microprocessor coolers [103], microfluid motion controllers [104], chemical microreactors [105] and biofluidic devices [106].

Measurement of temperature on the microliter scale and below is challenging because standard techniques require thermal contact and exchange of heat to achieve thermal equilibrium between probe and sample [43]. This leads to the restriction that sample heat capacity be much larger than that of the probe for accurate temperature measurements. While nanoscale metal thermocouples have been recently demonstrated [107], their novel architectures and requirement of electrical connection may not always be compatible with temperature sensing of fluids confined to nanoliter volumes or under flow conditions. Alternatively, using an EM field to probe a temperature dependent refractive index allows for highly accurate and non-invasive temperature sensing [43]. In this work we have addressed specific limitations present in prior SPR based temperature sensing studies by improving upon the sensing materials and interrogation methods used previously [30, 40–42].

Origins of Thermo-Optic Signals in the Kretschmann Configuration

In our study of SPP based thermometry we have used the Kretschmann configuration for excitation of SPPs on a metal-dielectric interface as discussed in Chapter I and depicted in Figure 2.1.. In this configuration the optical reflectance

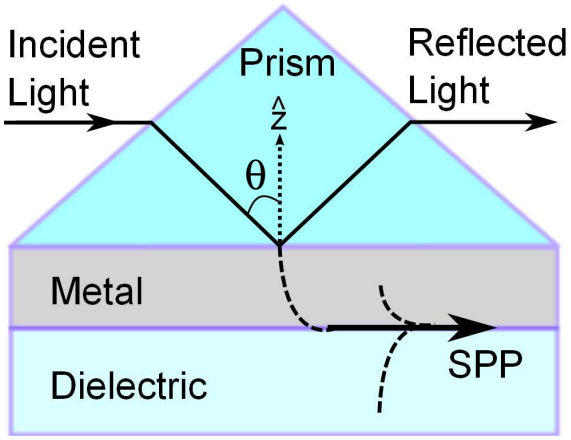

Figure 2.1. Schematic of the Kretschmann configuration (not to scale) for ATR coupling to SPPs at a flat metal-dielectric interface. Notice that the SPP is excited on the opposite side of the metal film from the which the light is incident. The dotted line indicates the direction normal to the interface, $\hat{z}$. Dashed lines represent the evanescent decay envelopes on the normal components of the electric fields.

of a monochromatic light beam with vacuum wave number k_0 incident to the metal film at angle θ can be expressed as [21]:

$$R(\theta, T) = \left| \frac{r_{pm} + r_{md} e^{i2k_m h(T)}}{1 + r_{pm} r_{md} e^{i2k_m h(T)}} \right|^2 \tag{II.1}$$

Here r_{pm} and r_{md} are the Fresnel reflection coefficients at the prism-metal and metal-dielectric interfaces, respectively and $k_{z,m}$ is the normal component of the

wave vector in the metal. The arguments of r_{pm}, r_{md}, and $k_{z,m}$ have been omitted for clarity in equation II.1, however each is dependent on temperature through the TO effect. This can be seen explicitly in the expressions for the reflection coefficients at the interface between materials i and j, $r_{ij}(\lambda, T, \theta_a)$, and the normal component of the wavevector in each material i, $k_{z,i}(\lambda, T, \theta_a)$. Here $\epsilon_i(\lambda, T)$ is the permittivity of material i, $\epsilon_p(T)$ is the permativitty of the coupling prism specifically, and θ_a is the incidence angle for light entering the prism from air:

$$k_{z,i}(\lambda, T, \theta_a) = k_0 \sqrt{\epsilon_i(\lambda, T) - \epsilon_p(T) \sin^2 \theta(\epsilon_p(T), \theta_a)} \tag{II.2}$$

$$r_{ij}(\lambda, T, \theta_a) = \left(\frac{k_{z,i}(\lambda, T, \theta_a)}{\epsilon_i(\lambda, T)} - \frac{k_{z,j}(\lambda, T, \theta_a)}{\epsilon_j(\lambda, T)} \right) \left(\frac{k_{z,i}(\lambda, T, \theta_a)}{\epsilon_i(\lambda, T)} + \frac{k_{z,j}(\lambda, T, \theta_a)}{\epsilon_j(\lambda, T)} \right)^{-1} \tag{II.3}$$

The origin of the TO effect in most non-conducting transparent dielectrics is due primarily to volumetric thermal expansion [108]. We have chosen to use the clear liquids water and ethanol for the dielectric medium due to their relatively large thermal expansion coefficients and consequently large TO coefficients [95]. However in metals the same temperature dependent electron scattering processes which cause Ohmic damping of SPP propogation also contribute to a temperature dependence of the refractive index, in addition to thermal expansion [42]. We have chosen to use silver for our metal film because it exhibits the least Ohmic loss among the noble metals at visible frequencies, which results in a narrower SPR [21] and increased sensitivity.

Calculation of Thermo-optic Signals in the Kretschmann Configuration

In the linear approximation the temperature dependent refractive index of any non-magnetic medium with dielectric function $\epsilon(T)$ is given by:

$$n(T) = n_0 + (T - T_0)dn/dT \equiv \sqrt{\epsilon(T)} \tag{II.4}$$

where n_0 is the material-specific refractive index at temperature T_0 and dn/dT is the material's TO coefficient. The linearized temperature-dependent thickness of the metal film is written as:

$$h(T) = h_0[1 + \alpha'(T - T_0)] \tag{II.5}$$

where h_0 is the film thickness at temperature T_0. The coefficient $\alpha' \equiv \alpha(1+\mu)/(1-\mu)$ is a geometric correction to the thermal expansion coefficient which accounts for expansion of the metal film primarily in the direction normal to the interface. The metal Poisson ratio μ defines the ratio of the material stress along the loading direction to the stress lateral to the loading direction and α is the standard metal thermal expansion coefficient [30, 109]. Using the linearized expressions for $n(T)$ and $h(T)$ we numerically calculated the derivative of the reflectance with respect to temperature, dR/dT from equation II.1. Systematically setting the TO and expansion coefficients of all but one material to zero allows us to evaluate the individual contribution of each material to dR/dT, represented by the terms in the expression:

$$\frac{dR}{dT} = \frac{\partial R}{\partial n_d}\frac{\partial n_d}{\partial T}|_{n_m,n_p,h} + \frac{\partial R}{\partial n_m}\frac{\partial n_m}{\partial T}|_{n_d,n_p,h} + \frac{\partial R}{\partial h}\frac{\partial h}{\partial T}|_{n_d,n_m,n_p} + \frac{\partial R}{\partial n_p}\frac{\partial n_p}{\partial T}|_{n_d,n_m,h} \tag{II.6}$$

In the above expression n_m, n_p, and n_d are the refractive indices of the metal, prism, and test dielectric, respectively. The first two terms in the expression represent the TO effect of the dielectric and metal, respectively. The third term accounts for the thermal expansion of the metal and the final term accounts for the TO effect of the BK-7 glass coupling prism. Figure 2.2. shows the individual contributions to dR/dT from the coupling prism, metal film, and test dielectric plotted as a function of incidence angle. The calculation was done for a $50nm$ thick silver film with liquid ethanol as the test dielectric. Previously published values for n_m, μ, α and the TO coefficients of silver, BK-7 glass, and ethanol were used in the calculations [20, 30, 95, 110]. Here we see that the contribution from the test dielectric is more than two orders of magnitude larger than the contributions from the metal film or the coupling prism. Considering this result we ignored the TO effect of the dielectric coupling prism in our calculations, however we included the metal film contributions to be prepared for the possible use of metals other than silver. We also see that the asymmetry in the SPR resonance curve results in an asymmetric dR/dT and that $|dR/dT|$ will be greatest at incident angles less than the SPR resonance angle, which is where dR/dT changes sign. We have chosen θ_0 to be near the angle which maximizes $|dR/dT|$, which is near 68° for water as the test dielectric and 71° for ethanol.

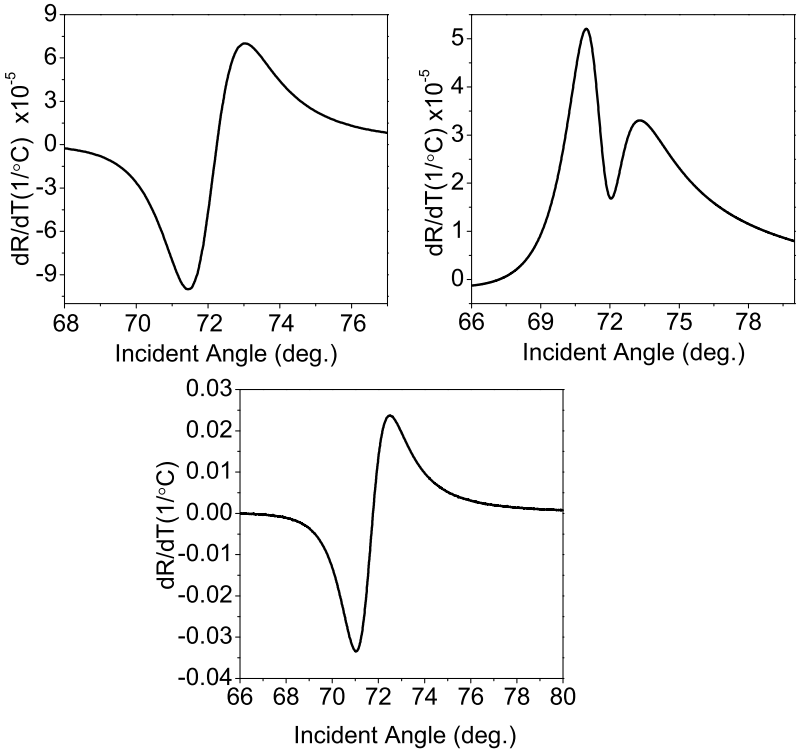

Figure 2.2. Panel (a) shows the contribution to dR/dT due to the TO effect in the coupling prism plotted against prism-silver incidence angle θ. Panel (b) shows the contribution due to the TO effect and thickness changes due to thermal expansion in the metal and panel (c) shows the contribution of the TO effect in the test dielectric. All calculations were for $T = 22°C$ using $\lambda = 632.8$nm, $h_0 = 50$nm and liquid ethanol as the test dielectric. Previously published values for n_m, n_d, n_p, μ, α and the TO coefficients of silver, bk7 glass, and ethanol were used in the calculations [20,30,95,110].

Experimental Setup for Measurement of Liquid Thermo-optic Coefficients

In order to address the issue of thermal gradients which hinder accurate TO measurement we have developed an apparatus for determining TO coefficients which consists of a temperature-controlled micro-volume liquid reservoir embedded in a thermal reservoir and coupled to a standard Kretschmann configuration setup. This

apparatus is shown schematically in Figure 2.3.. A $0.4mm$ deep fluid reservoir $6.3mm$ in diameter was drilled into a $1kg$ brass block which served as the thermal bath. Either water or ethanol were used to overfill the fluid reservoir in the brass to a total fluid volume greater than 13μl to prevent the formation of air bubbles when the coupling prism and silver film were attached as described below. Thermal evaporation under high vacuum is used to deposit a silver film with thickness of $\approx 50nm$ as measured by a quartz crystal monitor during deposition. The deposition substrate was a 1mm thick glass slide (Corning Glass Works soda lime glass) with refractive index equal to that of the coupling prism, $n = 1.512$. The opposite side of the slide was index matched to the BK7 glass prism using index matching oil to prevent formation of an air gap between the prism and slide. The prism and slide were then clamped to the brass mass such that the silver film was in direct contact with the liquid. A nitrile o-ring positioned in a shallow groove machined around the fluid reservoir formed a seal between the brass and glass slide. Metal foil was pressed between the brass and glass slide, around the external perimeter of the o-ring seal to decrease the magnitude of any thermal gradients between the heat bath and the optical interrogation region. Heating was achieved by running electrical current through a 10Ω resistor embedded within the brass heat bath, about 2cm away from the liquid reservoir. A digital thermometer with 0.01°C resolution was also embedded inside the brass at a distance of $250\mu m$ from the base of the liquid reservoir, and was used to read the temperature of the test dielectric. A HeNe laser

provided a collimated probe beam with $1mW$ of continuous wave (CW) power at the probe wavelength $\lambda_p = 632.8nm$. The 2mm diameter probe beam was incident on the silver film through the prism. The brass-prism system was affixed to a rotation stage mounted on a translation stage. This allowed for rotation to change the incident angle while maintaining the beam spot position at the center of the silver film and fluid reservoir A mechanical beam chopper provided a $911Hz$ signal modulation of the incoming probe beam, and the reflected signal was detected using a silicon photo diode and a lock-in amplifier locked to the chopper.

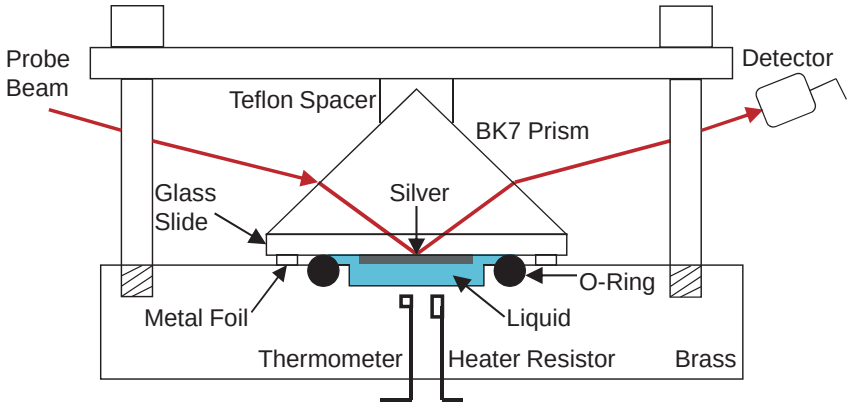

Figure 2.3. Diagram of the experimental setup excluding the stages to which the brass-prism system is mounted. The diagram is not to scale. Notice the clamp and o-ring system which seals the liquid inside the brass thermal reservoir.

Thermo-Optic Sensor Calibration

In order to apply the model discussed above to our experimental results and measure the liquid TO coefficient it was necessary to have an accurate determination of the refractive index and thickness of the silver film. The material properties

of thin metal films generally depend on parameters such as deposition conditions and ambient environment, so we determined the sample-specific permittivity of our deposited silver films *in situ* for $\lambda_p = 632.8nm$ using the SPR resonance [21]. We measured the reflectance of the silver film as function of incident angle at 0.25° intervals at a known, constant temperature, T_c as seen in Figure 2.4.. Values for the real and imaginary parts of the silver permittivity, $\epsilon'_m(\lambda_p, T_c)$ and $\epsilon''_m(\lambda_p, T_c)$, respectively, as well as the film thickness, $h(T_c)$ were determined using a least-squares fit of the theoretical reflectance to the measured values. The values for film thickness and refractive index, $h(T_c)$, and $n_{m,c} = \sqrt{\epsilon'_m(\lambda_p, T_c) + i\epsilon''_m(\lambda_p, T_c)}$, provided by the fit were then used as the initial values in the linearized equations II.4 and II.5 for subsequent calculations. Figure 2.4. compares reflectance calculated using film thickness measured with a crystal monitor during deposition and tabulated values for the optical constants of silver [20] with the calibration curve $R_c(\theta, T_c)$ which was calculated using $\epsilon_m(\lambda_p, T_c)$ and $h(T_c)$ obtained by the fit. We can see from this figure that using the tabulated values for the silver optical constants result in a theoretical SPR reflectance curve which is wider and shifted to higher resonance angle than the measured curve. These effects are due to an overestimate of the imaginary part of the silver refractive index in the tabulated values [20]. The disparity in the two curves illustrates the need for accurate determination of sample specific optical constants and thickness.

We used a DekTak profilometer to independently verify the film thickness

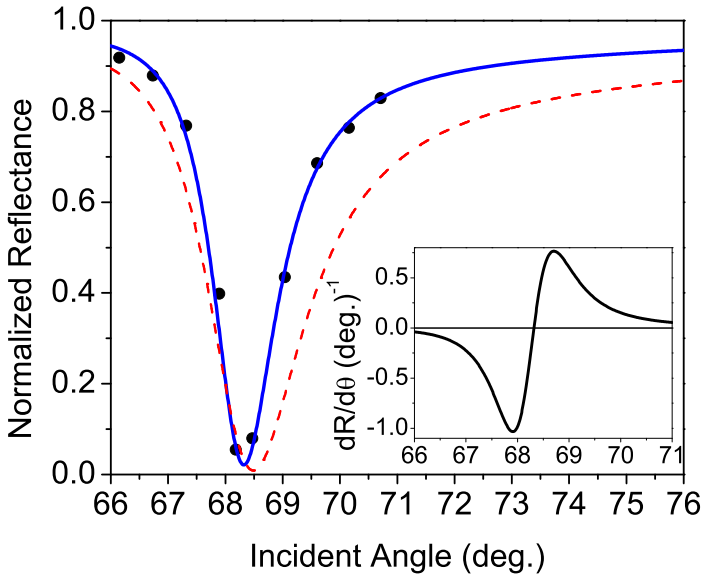

Figure 2.4. Reflectance as function of incident angle for probe wavelength 632.8nm with ultra-pure water (18.2MΩ-cm resistivity) as the test dielectric at $T = 21.65°$C. Measured values are indicated by dots. The solid curve is the reflectance function obtained by a least-squares fit to the data with ϵ'_m,ϵ''_m and h as parameters. The dashed line denotes the calculated reflectance using tabulated values for the refractive index of silver [20] and $h = 50nm$ measured during deposition. Inset: Angular derivative of the reflectance calculated from the solid curve in the main figure, plotted against incident angle.

obtained by the fitting procedure, providing greater confidence in the obtained optical constants. The DekTak profilometer was known to be sufficiently precise, but not necessarily accurate to the resolution we required so we first calibrated the DekTak to a 3nm height resolution. The DekTak was calibrated using a standard fluorescence interference contrast (FLIC) [111] chip[1], which consists of an array of steps with heights measured to less than single nanometer resolution using

[1] A calibrated FLIC chip was kindly provided by the Parthasarathy Lab, Department of Physics, University of Oregon

FLIC. Scanning these chips in a variety of orientations allowed us to produce the step-height calibration curve seen in Figure 2.5..

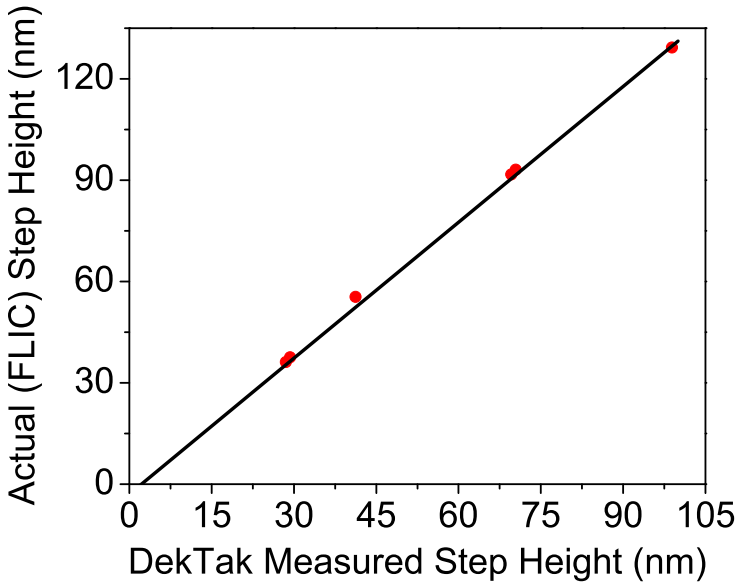

Figure 2.5. Calibration curve for DekTak profilometer allowing for 3nm step-height resolution. We see that actual height is consistently 1.35 times greater than measured by the DekTak for heights greater than $30nm$.

Experimental Measurement of Liquid Thermo-Optic Coefficients

Experimental Procedure

To begin the measurement the rotation stage was positioned to produce the desired probe beam-silver film incident angle, θ_0. For maximal sensitivity θ_0 was chosen near the extremal value of $|dR(\theta, T)/dT|$ as obtained from a calculation such as that shown in Figure 2.2.. The temperature of the system was then increased

by applying 4 volts across the embedded resistor. When the desired temperature was reached (as determined by reading the embedded thermometer) the heating power was turned off and the system was allowed to relax for 30 seconds. This guarantees that the thermometer readings are consistent with the temperature of the liquid reservoir by eliminating any significant thermal gradients in the liquid as well as between the liquid and the brass mass. Following this initial relaxation, LabView data acquisition software was used to record the time, temperature, and reflected optical probe signal as the system was cooling, at intervals of 0.01°C. Fixed temperature intervals, equal in magnitude to the resolution of the thermometer were used instead of fixed time intervals when recording data. This was to avoid over-sampling the reflectance and temperature at longer times as the rate of temperature change decreased exponentially during the cooling process, following Newton's law of cooling [112]. The resulting data set is used to obtain the measured reflectance as a function of temperature, expressed as $R_m(\theta_0, T(t))$ with t denoting time. Figure 2.6. shows $R_m(\theta_0, T)$ obtained for water (main figure) and ethanol (bottom inset). Each data point represents an average of ten successive values measured $130ms$ apart using the lock-in amplifier, with their computed standard deviation used as the measurement error for each averaged point. These errors range in value between 1×10^{-4} and 4×10^{-4}, and are not well resolved on the scale used in Figure 2.6..

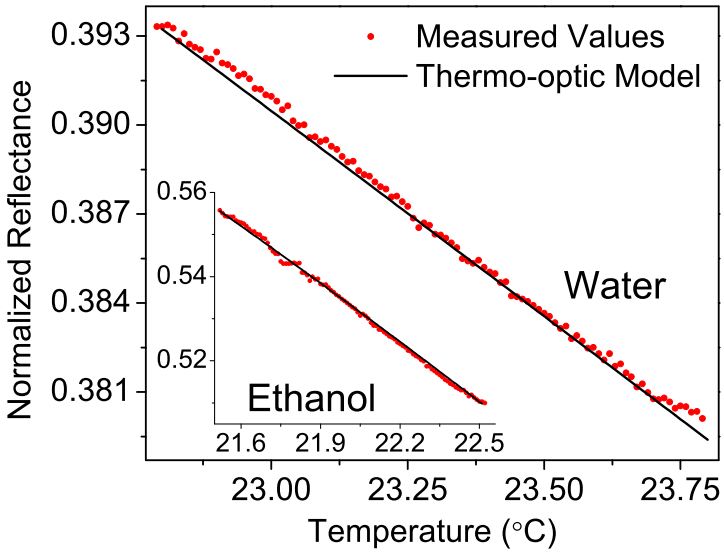

Figure 2.6. Reflectance as function of temperature for water (main figure) and ethanol (inset). Measured values are denoted by dots and solid traces indicate the fitted theory, which is used to determine the TO coefficient.

Data Analysis and Extraction of the Thermo-optic Coefficient

To model $R_m(\theta_0, T)$ it is necessary to know θ_0 accurately. We see from Figure 2.4. and the inset that the reflectance varies strongly with incident angle in the vicinity of the SPR. In fact, $|\partial R(\theta, T)/\partial\theta|_T$ is large enough (≈ 1) near θ_0 that an error in θ_0 of order $\left(1 \times 10^{-4}\right)^\circ$, which is below the angular resolution of standard rotational stages, will introduce an additional reflectance error comparable to our measurement error.

To enable a more accurate determination of θ_0 in our setup we extracted θ_0 from $R_m(\theta_0, T)$. In this case we have two parameters to determine from the $R_m(\theta_0, T)$ data; those being θ_0 and dn_d/dT, which are each constrained by the stage accuracy

and reported literature values, respectively. Comparing the final reflectance value, $R_m(\theta_0, T_f)$ to a theoretical $R(\theta, T_f)$ allowed us to extract θ_0. We used the reflectance value at the end of the cooling run because this is when the cooling rate and thermal gradients are smallest so that errors in the liquid temperature measured by the thermometer were minimized. However, $n_d(T_f)$ is required for the theoretical calculation, but was not necessarily known. We required an initial estimate of dn_d/dT to determine $n_d(T_f)$ from the linearized equation II.4 together with a tabulated $n_d(T_0)$. We used an average of literature values for this initial estimate of dn_d/dT [95, 96, 113] and determination of θ_0. Using this determined θ_0, we applied a least squares fit of the theoretical $R(\theta_0, T)$ to the measured $R_m(\theta_0, T)$ to determine a new value for dn_d/dT. This revised dn_d/dT is then used to recalculate $n_d(T_f)$ and $R(\theta, T_f)$ and extract an updated θ_0. Several iterations of this fitting procedure were applied until the change in the calculated $R(\theta_0, T_f)$ due to the revision of dn_d/dT was within the measurement error in $R_m(\theta_0, T_f)$, so that another extraction of θ_0 and further iteration was meaningless. This procedure converges on a TO coefficient that reproduces $R_m(\theta_0, T)$ for a final value of θ_0, which was always within the angular measurement error of our stage. We have specifically chosen θ_0 in the linear section of the reflectance curve, which results in $R_m(\theta_0, T)$ being linear over temperature changes of order $1C^\circ$, as seen in Figure 2.6.. In this case the slope, $dR_m(\theta_0, T)/dT$ is independent of the actual reflectance and θ_0, such that $dR_m(\theta_0, T)/dT$ is effectively determined by dn_d/dT alone and the

simultaneous fitting of θ_0 does not affect the final extracted value for dn_d/dT. The solid lines in Figure 2.6. demonstrate the result of this iterative fitting procedure for both fluids used. We measured the TO coefficients of ethanol and water to be $(4.20\pm0.08)\times10^{-4}$ RIU/°C and $(1.0\pm0.1)\times10^{-4}$ RIU/°C, respectively. These agree very well with the reported values of $(4.1 \pm 0.47) \times 10^{-4}$ RIU/°C for ethanol [95] and $(1.00 \pm 0.06) \times 10^{-4}$ RIU/°C for water [96, 114].

SPP Based Microfluid Temperature Measurement

SPP Based Temperature Sensing Considerations

The same basic setup described above for SPP based measurement of the TO coefficient was used for continuous determination of the sample temperature. This was accomplished by continuous monitoring of the reflectance from the sample at a fixed interrogation angle and a single wavelength in the same way the TO measurement was done. This alternative *reflectance interrogation* method [115] is significantly faster than both angular and wavelength interrogation techniques, which are typically applied in SPR temperature sensing [35]. Moreover, this technique is more suitable to SPR-based real-time thermometry in a range of microfluidic systems due to a lack of reliance on moving parts.

Test dielectrics with large TO coefficients will result in greater temperature sensitivity of the device and test dielectrics with relatively low n_d are also

desirable. We see in Figure 2.7. that increasing n_d by only a few percent causes significant broadening in the SPR resonance. This broadening effectively decreases $|\partial R(\theta, T)/\partial T|_{\theta_0}$, leading to lower sensitivity. Previous demonstrations of SPR temperature sensors have employed metal-semiconductor junctions to exploit the large TO coefficients of materials such as amorphous silicon. However, most semiconductors exhibit relatively high losses in the optical frequency range as well as large values for their refractive indices, which lead to broadening of the SPR and reduced sensitivity [40, 41]. These factors led us to conclude that transparent fluids with relatively low n_d and large TO coefficients constitute nearly ideal candidates for accurate SPR-based temperature sensing. As examples we exploited these properties in ethanol and water in our microfluid temperature sensor.

Detection of SPP Induced Heating

In order to determine the temperature from a measured reflectance we referred to previous calibration data where temperature and reflectance had been accurately measured, such as the data in Figure 2.6.. We applied a linear fit to the calibration data to obtain an expression for temperature as function of reflectance, $T(R)$. Using the fitted expression for $T(R)$ we are able to calculate the fluid temperature from reflectance measurement. Figure 2.8. shows temperature plotted against time measured by the embedded thermometer during a cooling cycle of the thermal reservior. The temperature calculated from the reflectance measurement using

$T(R)$ is comparted to the the values measured by the thermometer, demonstrating the accuracy of our method. To determine the measurement error, ΔT, of this temperature sensor we compute $\Delta T = \sigma \left(\partial R_m(\theta_0, T(t))/\partial T\right)^{-1}$ where $\sigma = 4 \times 10^{-4}$ is the measured error in the reflectance. We find ΔT to range between $0.03 - 0.06°\mathrm{C}$, depending on the specific h_0, $\epsilon_m(\lambda, T_0)$, ϵ_d, and choice of θ_0.

As mentioned previously, large errors in measuring the fluid temperature with the embedded thermometer exist mainly when the system is far from thermal equilibrium and is undergoing rapid cooling or heating. However, the fluid temperature can still be determined by a reflectance measurement in this

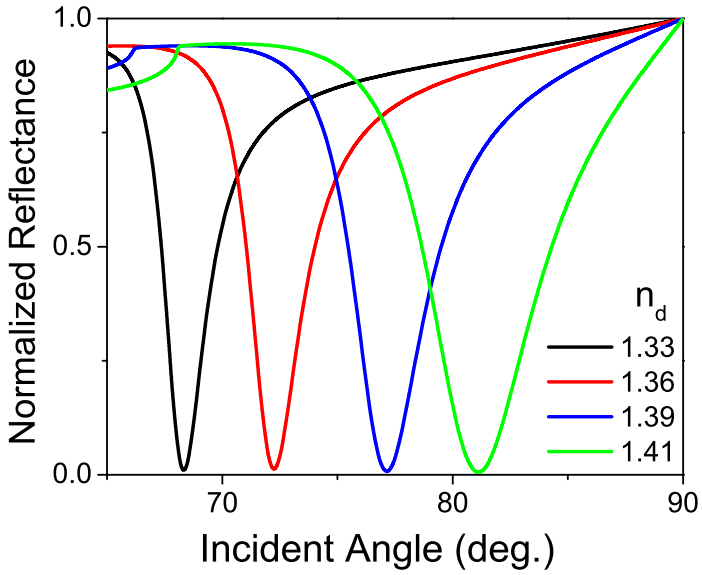

Figure 2.7. Reflectance as a function of incident angle plotted for several values test dielectric refractive index: 1.33 (black), 1.36, (red), 1.39 (blue), and 1.41 (green). The film thicknesses used in the calculations have been adjusted for each value so that only the effect of the increasing refractive index is compared.

case. While a running average of the reflectance signal for noise reduction is acceptable when the temperature is varying slowly, it is not practical when rapid changes in temperature are taking place. However, the calibrated reflectance-based temperature measurement has sufficient resolution to allow for meaningful temperature measurement without additional signal averaging. The inset to Figure 2.8. shows the non-averaged temperature values plotted against time for rapid cooling of water. The high cooling rate was achieved by rapidly heating the water layer next to the silver film with an incident laser, thus bringing it far from equilibrium with the thermal mass. The heater laser was a frequency doubled

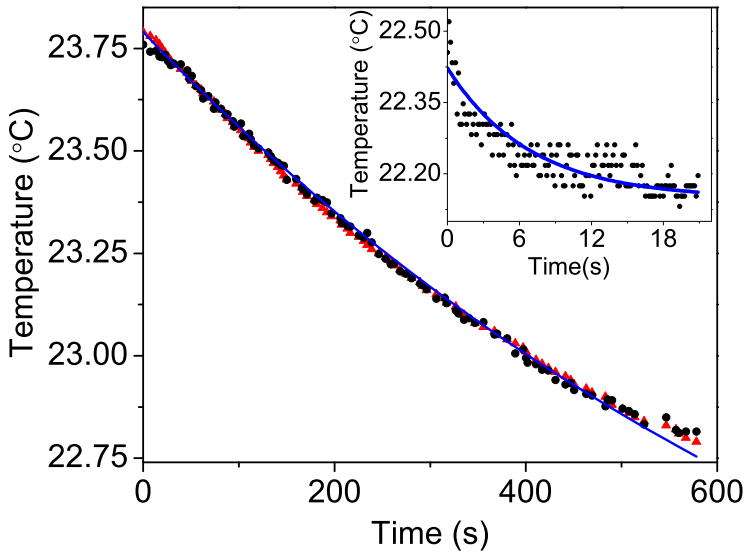

Figure 2.8. Temperature plotted against time showing calculated values (dots) and values measured using the thermometer (triangles). The solid curve denotes a fitted exponential cooling law, with a coefficient of determination $\mathcal{R}^2 = 0.998$. Inset: Non-averaged temperature values obtained from measured reflectance (dots) and fitted exponential cooling law, with coefficient of determination $\mathcal{R}^2 = 0.757$ (solid line).

Nd:Yag providing $\approx 40mW$ CW power at a wavelength of $532nm$. The heater laser was coupled into the Kretschmann setup from the opposite side of the prism as the HeNe probe beam. The heater laser beam spot surrounded the probe beam spot. The incident angle of the heater laser was set near the SPP resonance angle for its wavelength, which is several degrees greater than that for the probe beam, allowing for the excitation of SPPs and producing the characteristic dip in the reflectance. The thickness of the silver film was optimized for the probe wavelength of $632.8nm$, not for the heater laser wavelength, so the lowest reflectance value achieved was ≈ 0.5. The $\approx 20mW$ of power missing from the reflected beam are deposited as heat in the silver film as discussed in the SPP Coupling section of Chapter I, and some of this heat is conducted to the adjacent water. A $20s$ heating cycle by the heating laser was sufficient to raise the temperature of the fluid at the interface by approximately $0.3°C$, which is significanly larger than our temperature resolution. After the heating cyle, the heater laser was blocked and the system was allowed to cool. The data were obtained by recording the reflectance from the HeNe probe laser every $130ms$ during cooling and then converting the data to temperature values using the previously acquired calibration $T(R)$. We see from the noise in the cooling data that the temperaure resolution in the case of rapid cooling without reflectance measurement averaging is roughly $0.07°C$. The exponential cooling behavior is still evident despite the noise and we are able to apply an exponential fit and extract a meaningful decay constant. The cooling decay constants for the

entire system heated by the resistor and the laser heated liquid-metal interface are 1.5×10^{-3} and 1.3×10^{-1}, respectively. As expected, the low heat capacity and high surface area to volume ratio of the microfluid relative to the brass mass cause a much greater cooling rate for the locally heated fluid than for entire system.

SPP Based Thermo-optic and Temperature Sensor Limitations

Sensor Range Limitations

Figure 2.2. demonstrates that the magnitude of $dR(\theta, T)/dT$ is significant over a limited angular range, spanning either side of the resonance angle. The choice of interrogation angle θ_0 to be near the extremal value of $|dR(\theta, T)/dT|$ provides maximal sensitivity for the detection technique used here. However, a sufficiently large change in fluid temperature may shift the SPP resonance angle away from the initially optimized value of θ_0, into a lower sensitivity range, and potentially away from the calibration curve of the instrument. While the high sensitivity and accuracy of this setup are therefore limited to a finite range of temperatures, the method should be robust for temperature changes of several degrees. To verify this we measured the temperature-dependent reflectance over a range of 10°C, as shown in Figure 2.9.. There we can see the minimum of the characterisitc SPR reflectance dip, only now traced out by changing $n_d(T)$ rather than θ.

The inset to Figure 2.9. demonstrates the agreement between theoretical dR/dT

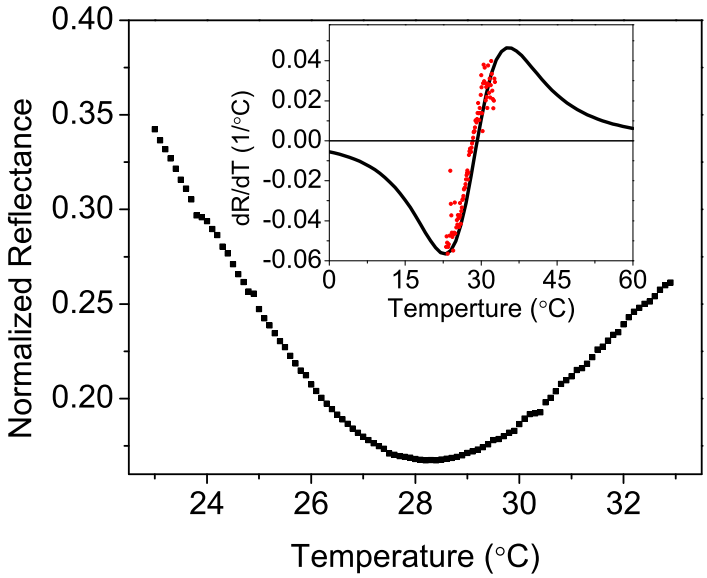

Figure 2.9. Reflectance values (raw data) plotted against temperature measured using ethanol as the test dielectric. Inset: Temperature derivative of the reflectance calculated using the theoretical model (solid line) and measured reflectance values from main figure (dots).

(solid line) and dR/dT calculated from the measured data shown in the main figure (dots). From the data and calculation in the inset we see that $|dR(\theta, T)/dT|$ drops to half its extremal value over a range of $\sim$ 5°C in either direction, and hence the high resolution operational range of this setup is roughly 10°C. The slope and width of the SPR depend on n_d and thus this range will vary somewhat with the sensing fluid used.

Probe-induced Heating

Generally the excitation of SPPs in metals is accompanied by heating of the metal and adjacent fluid as discussed previously. Due to this heating it is important

to minimize energy transfer into the film while still maintaining measureable level of reflected light. This provides further argument for use of reflectance interrogation, which allows us to choose a single θ_0 and avoid the low reflectance signal and maximal SPP induced heating that occur at θ_{spp}.

When probe-induced heating occurs the fluid temperature will rise until the total power input, P_{in} equals the power loss, P_{out} and steady state is reached. The probe-induced heating can be estimated by determining the steady state temperature difference, ΔT_{ss}, across the water filled reservoir which satisfies the steady state relation $P_{in} = P_{out}$. Here P_{in} denotes the rate of energy transfer into the interfacial fluid due to SPP induced heating and P_{out} is the rate of energy transfer away from the interface. Considering that the SPP induced heating occurs at the silver-water interface, we will assume that excess SPP-generated heat is lost through conduction to the fluid reservior and we neglect heat flow across the film into the prism. The thermal conductivity of water, k_w is 750 times less than that of silver [116] so we also assume conduction through the water to be the limiting factor in heat transfer. We also assume that heat generated in the film is immediately conducted across the entire area of the silver-water interface. We treat the fluid reservoir as an isolated cylinder, ignoring heat flow transverse to the liquid-metal interface, and assume that conduction is the only method of heat transfer, ignoring both convection and radiation. While not accurate, these assumptions will decrease the theoretical ability of the fluid to dissipate heat from the interface and thus will

overestimate ΔT_{ss}. In this case the calculated ΔT_{ss} will serve as an upper bound on probe induced heating. Under these assumptions the steady state rate of heat conduction through the liquid reservoir follows the steady state solution to the one-dimensional heat equation [117]: $P_{out} = k_w A \Delta T_{ss}/L$, where A is the cross sectional area of fluid reservior and L is the reservoir depth. Setting $P_{in} = P_{out}$ and solving for $\Delta T_{ss}/L$ we have: $\Delta T_{ss} = LP_{in}/(k_w A)$. With a probe power of $1mW$ and a typical reflectance near θ_0 of ≈ 0.5 we have $P_{in} = 5 \times 10^{-4} W$. The reservoir has $L = 4.0 \times 10^{-4} m$ and $A = 2.8 \times 10^{-5} m^2$ and k_w is $0.6 W/m \cdot K$ [116]. Entering these values we calculate $\Delta T_{ss} \simeq 0.01°\text{C}$, which is below the operational resolution of the instrument described here. Taking into consideration transverse conduction, fluid convection, and conduction in the coupling prism, the rise in temperature of the fluid due to the probe is guaranteed to remain well below the current detection limit.

Fluid Volume Limitations

The minimum and maximum fluid volumes that can be used with our setup are limited fundamentally by the scale of the SPP evanescent field decay length and practically by the technical difficulties in achieving thermal equilibrium across very large masses. The minimum fluid volume necessary for the SPP-based measurement of TO coefficients and temperature is set by the size of the optical beam spot and the decay length of the SPP electric field into the dielectric medium, γ_d. The

liquid-metal contact region must be greater than the beam spot and the fluid layer thickness, in our case the reservoir depth, must be much greater than γ_d. The projection of a beam spot with diameter D_b onto the prism-silver interface is an ellipse with long axis $D_p = D_b/cos\theta_0$ and short axis equal to D_b. For typical values of θ_0 near 70° and $D_b = 2mm$ used in our setup, the long axis of the beam projection was $D_p \simeq 6mm$. The decay length γ_d is typically in the range of $(100 - 300)$nm, depending on the fluid's refractive index as seen in Figure 1.7.. These conditions render nanoliter liquid volumes accessible to this type of temperature measurement.

The maximum appropriate fluid volume for this setup is limited by the requirement that significant thermal gradients do not exist across the fluid reservoir because the SPP field only probes the fluid within a few hundred nanometers of the interface. If large thermal gradients exist in the fluid then the fluid refractive index sampled at the interface will no longer be properly correlated with the fluid temperature measured elsewhere (e.g., in the fluid or a thermal bath surrounding the fluid). Cosequently, errors will be introduced into the TO measurement. The time required to reach a specific level of temperature uniformity across a fluid increases with the fluid volume and the techincal difficulty in with surrounding the fluid by a thermal bath also increase. This setup was specifically designed to address these issue by using microliter volumes for liquid TO coefficient determination and is thus not well suited for use with large fluid volumes.

Conclusions

In this chapter we have discussed the development of a minimally-invasive SPR-based TO sensor which addresses typical sources of error in TO coefficient measurement. The apparatus exploits the sensitivity of SPPs to interfacial refractive index for extracting values of fluid TO coefficients with accuracy of 1×10^{-5} $^{\circ}\mathrm{C}^{-1}$. This accuracy was made possible by coupling the test liquid to a thermal reservoir and employing a reflectance interrogation method. Such accuracy may be useful in calibrating SPP-based sensors commonly used for biochemical sensing. With accurate knowledge of the TO coefficient and accurate monitoring of the temperature the effects of temperature fluctuations on the reflectance measurement can be corrected for, thus increasing the accuracy of the sensor.

The setup can also be used to determine the temperature of microfluids with temperature resolution of 0.03°C. The method employs reflectance interrogation utilizing a low-power probe laser and requires only a single wavelength, polarization, and interrogation angle for accurate determination of temperature. Due to the low refractive indices and high TO coefficients that many clear fluids possess, this configuration is particularly suited for precise diagnostics within opto-fluidic systems. Requiring only microliter fluid volumes to operate with potential for further miniaturization, the method may be readily integrated into a variety of lab-on-chip platforms where accurate and precise knowledge of temperature conditions inside microfluidic systems is required.

The methods we have developed for SPP based temperature sensing might be applied to thermal diagnostics of nanoscale systems. As a proof of principle we have detected the change in temperature of a $50nm$ thick silver film and adjacent microfluid caused by the SPP mediated absorption of optical energy in the film. In similar fashion the temperature of a fluid reservoir with nanoscale dimensions might serve as a probe for sensing energy transfer to nanoscale structures by optical absorption. For example, optical heating of nanostrcutured metal films is known to occur and has been shown to result in photomodification of the film structure [118]. Using the method we have developed, the relative efficiency of optical to thermal energy conversion might be measured as a function of the film structure. The localized surface plasmon excitations (LPS) occurring in nanostructured metal films are also sensitive to the local temperature of the film and surrounding medium [92]. In this case the more general ideas and methods we have developed might be used to exploit LSP resonance shifts in nanostructured metallic films for thermal diagnostics within the films.

In the following chapters we will discuss our work to understand the morphology dependence of nanostructured silver film photoluminescence (PL) in terms of the film microstructure. These films experience significant optical heating which can modify the film surface. As will be discussed in Chapter IV, this effect may play a role in determining the PL properties of the films, most notably the PL time dependence [118]. A future study of this photo-annealing is exactly the type of

investigation which might benefit from the surface plasmon based temperature sensing methods we have worked to develop.

CHAPTER III

MEASURING AND MODELING THREE-DIMENSIONAL STRUCTURE OF SILVER TOLLEN'S FILMS

Introduction

Motivations for Studying the Structure of Silver Tollen's Films

As discussed in Chapter I, nanostructured metallic films exhibit unique optical properties that differ substantially from those of bulk metals at optical frequencies. These properties are heavily influenced by the excitation of LSPs on the (sub)wavelength scale structures. Figure 1.12. shows scanning electron microscope (SEM) images of such nanostructured silver films fabricated by the Tollen's reaction [70, 119, 120]. The details of the Tollen's deposition method are discussed later in this chapter. In general LSP excitations occur in nanostructured metal films because $\epsilon_m(\lambda) < 0$ at visible wavelengths. However, specific optical phenomena such as electromagnetic (EM) field enhancement, photoluminescence (PL), and surface enhanced Raman scattering (SERS) depend on the exact film morphology [48, 67]. This sensitivity to film structure and the possibility for control of optical properties via morphological tuning has lead to the variety of

applications for metallic nanostructures discussed in Chapter I. Such applications include surface plasmon guiding and circuitry [121], optical sensing [94], optical tweezers [55], and solar cell efficiency enhancement [80, 81, 122]. The additional EM field enhancements resulting from plasmon coupling, gap plasmons, and wave localization in disordered metallic films make them excellent materials for use in non-linear optical applications [67] such as SERS [14, 48, 61, 69], harmonic generation [45–47], and random lasing [65, 85–88].

In Chapter I we discussed the major goal of our research, which was to improve understanding and predictability of morphology dependent PL from nanostructured metallic films. In order to achieve this goal we must first characterize the relationship between PL and structure in these films and then examine the processes underlying these relationships. Once this has been done, the film optical properties can be more accurately predicted based on measurable structural properties as well as tuned by controlled variation of the structure.

Our first step toward this goal was to characterize the growth and structure of a particular type of disordered, nanostructured metallic film across a wide range of morphologies [61, 120]. We chose to work with Tollen's films for three distinct reasons:

(i) The films can be fabricated in a wide range of structural morphologies with a single method by varying a single parameter, in this case deposition time.

(ii) The films have become a popular model system for studying nanoscale

metallic optics and are already used in a variety of applications such as SERS, fluorescence enhancement and optical sensing [48, 61, 67, 68, 70, 94, 120, 123–125]

(iii) The complete three-dimensional (3D) structure of the films is not well known or easily characterized [126] and determining this makes an important contribution toward these films reaching their full potential for use in optical applications.

Having discussed our motivations for studying the structure of Tollen's films, we now discuss our motivations for employing modeling and simulation techniques in the study.

Motivations for Modeling and Simulating the Deposition and 3D Structure of Tollen's Films

Our motivation for applying modeling and simulation methods in addition to experiment in our study of microstructure in Tollen's films is two-fold. First, doing so provides access to the 3D structural properties of the films across multiple length scales, which is an important step toward understanding and optimizing the optical properties of these films. For example, effective medium theories are often used to calculate the effective optical constants of a composite medium, such as the metal-dielectric composite formed by a nanostructured metallic film [127]. Effective medium theories can be applied to metallic films when the average

film thickness is less than the optical skin depth in the metal and the structural feature sizes are much smaller than the wavelength of incident light. Three dimensional structural properties such as volume filling fraction, average thickness, and pore/particle size are important inputs to effective medium theories. These 3D structural properties might be obtained by an array of experiments. For example, atomic force microscopy (AFM) can provide surface topology, x-ray scattering can provide particle/pore size distributions and surface roughness [128, 129] and gas permeability or adsorption can provide filling fraction [128, 130, 131]. These methods are well established and typically robust, however each has limitations which may prevent complete structural characterization, even by their combined application [128, 129]. For example, AFM performs poorly on fragile samples or those with multiscale roughness [126]. Gas adsorption may require a range of probe molecules for accurate micropore measurement [128, 129]. Standard x-ray scattering methods suffer from sample thickness limitations and the area probed per unit time is small compared to imaging techniques such as AFM or SEM [128, 129].

Computer simulation is yet another complimentary method for characterization of 3D film structure. Simulations have the added advantage of providing access to a wide array of 3D structural properties from a single characterization method in digital format [132–137]. For example, film growth simulations can provide simultaneous access to thickness, roughness, porosity, and particle sizes as well as

other characteristics that will be discussed in this chapter. However, simulations are also limited in their scale of applicability by the available computing power [138]. More fundamentally, computer simulations are only as accurate and relevant as the physical models underlying them and the approximations and limitations inherent to the model must be considered when using simulation as a scientific tool [132]. This chapter will discuss in detail our work to develop a physically relevant model of Tollen's film deposition and to simulate the growth and 3D structure of the films as a first step toward our larger goal of understanding their optical properties.

Our second motivation for the modeling and simulation work was to develop an empirical 3D model of Tollen's film deposition informed by analysis of two-dimensional (2D) SEM images which might then be generalized to other deposition methods. The general concept of using measured 2D structural data to constrain 3D models and simulations is common in fields where measurement of 3D data is difficult, expensive, or impractical. For example, 2D seismic lithology data describing distributions of material interfaces is used as input for geological simulations to estimate 3D lithology distributions [139]. In another example, comparison of measured and simulated structure in the 2D projection of microparticle aggregates has been used estimate parameters in a 3D aggregate growth model [140]. Nanoscale surface characterization technologies such as AFM and SEM now allow for rapid imaging of nanostructured films. This has allowed for the development of metal film deposition models based on 2D structural

information extracted from AFM and SEM images [141, 142]. We have worked to develop a chemical deposition model which allows for 3D simulation of Tollen's film deposition across multiple size scales using desktop-scale computing resources. This work provides further insight into the physical mechanisms underlying the deposition process and gives researchers an additional tool for characterizing metal film structure. The film deposition model itself and our method for determining the model parameters from analysis of SEM images are discussed in this chapter. We begin with an overview of film growth simulation methods.

Metallic Film Deposition Simulation Methods

Typically two methods for film growth simulation are used, those being molecular dynamics (MD) and Monte Carlo (MC) methods. Molecular dynamics simulations are deterministic, where the trajectories of individual particles (e.g. atoms) are calculated from known initial conditions for the system. The MD method provides ensemble values by calculating the trajectories many times with initial conditions varied according to a distribution take from a physical model, such as a Boltzmann distribution of energies. Simulated films can be built up by calculating many trajectories and keeping track of final particle locations to be used as initial conditions in the next iteration [132]. However, calculating and tracking the complete trajectories of many particles is computationally expensive. When the deposition process is stochastic in nature then individual particle trajectories

can instead be drawn randomly from a known distribution according to a Monte Carlo simulation algorithm [132].

Monte Carlo methods are used to simulate stochastic processes according to a Markov chain of states. The Markov chain is a generalization of deterministic time evolution because each new state x_i is dependent on the previous state x_{i-1}. However, each x_i is stochastically (randomly) rather than causally derived from x_{i-1}. Typically the difference in energy, $\Delta E(x_i, x_{i-1})$ between states x_i and x_{i-1} is used to determine the probability, $P(x_i, x_{i-1})$ that x_i will follow x_{i-1}. For example, the commonly used Metropolis function calculates $P(x_i, x_{i-1})$ from the Boltzmann factor: $P(x_i, x_{i-1}) = (1/\tau)e^{-\Delta E(x_i, x_{i-1})/k_B T}$ if $E(x_i, x_{i-1}) < 0$ and $P(x_i, x_{i-1}) = (1/\tau)$ if $E(x_i, x_{i-1}) > 0$ [132]. We will determine $P(x_i, x_{i-1})$ by comparing the 2D structure of films simulated using an MC algorithm to that extracted from SEM images, as will be discussed in the following sections. The general MC algorithm for generating the Markov chain of states is as follows [132]:

1) Draw a random number r from a uniform distribution over the interval [0,1].

2) Use r to choose a new state, x_i to test.

3) Calculate the difference in energy, $\Delta E(x_i, x_{i-1})$, between states x_i and x_{i-1}.

4) If $\Delta E(x_i, x_{i-1}) < 0$ accept the new state and return to step 1.

5) If $\Delta E(x_i, x_{i-1}) > 0$ draw a random number r

6) If $r \leq P(x_i, x_{i-1})$ accept the new state and return to step 1.

7) Otherwise reject the new state and remain in current state.

8) Return to step 1.

Typically the above algorithm is applied to an ensemble of particles, from which ensemble values can be calculated and used as inputs for $P(x_i, x_{i-1})$ in the next iteration. For example, $P(x_i, x_{i-1})$ may be temperature dependent as in the Metropolis function, and the temperature might be deduced by sampling the ensemble of current energy states in the system. Simulated films can be built up using the MC method by applying the algorithm above to particles in succession or in parallel. For example, particles may be placed on the substrate and moved along it by the MC method, simulating surface diffusion of the particles. The dependence of the resulting film structure on parameters entering $P(x_i, x_{i-1})$, such as substrate temperature or particle-film and particle-substrate binding potentials can then be investigated [132–134].

Certain processes cannot accurately be modeled by MC methods alone because some values entering $P(x_i, x_{i-1})$ for individual particles are not well determined by ensemble averages [132, 142]. In such cases hybrid simulation methods are used where some processes are simulated by MC and others by MD. In the case of sputter deposition for example, the motion of the substrate atoms may be modeled by MC while trajectories of high energy impinging atoms are determined by MD

methods [132]. The stochastic nature of our particle aggregation model of Tollen's deposition is well suited to MC simulation and we have employed this method in our study. This model and the MC type algorithm we used to simulate it are discussed in the following sections, however we first introduce the Tollen's film deposition process in detail.

Fabrication of Silver Tollen's Films with Varied Morphology

The Tollen's method is a chemical deposition process than produces polycrystalline silver films by reduction of silver nitrate. The Tollen's reaction we employed for fabrication of nanostructured silver films was [70]:

$$RCHO + 2Ag(NH3)2OH_{(aq)} \rightarrow 2Ag_{(s)} + RCOONH4_{(aq)} + 3NH3_{(aq)} \quad \text{(III.1)}$$

A $0.6\%(wt/wt)$ glucose solution (RCHO) held at 6.5 °C was used as the reducing agent. The Tollen's reagent was prepared by adding $0.5g$ of a 0.5% sodium hydroxide solution to $0.5g$ of $0.33\%(wt/wt)$ silver nitrate solution. Insoluble silver oxide is formed and precipitates out of the solution as a brown solid. A 10% ammonium hydroxide solution was then slowly added, while stirring until all precipitate was dissolved. The amount of ammonium hydroxide required to dissolve the precipitate was between $1.4g$ and $1.7g$.

Cleaned glass microscope slides were soaked in the prepared glucose solution for 1.5 hours prior to addition of the Tollen's reagent. The glucose solution was immersed in a temperature controlled water bath, held at 6.5 °C which served to

slow the reaction kinetics and allow for greater control of the film morphology. The Tollen's reaction typically started within 20 minutes after adding the Tollen's reagent to the glucose solution containing the slides. The start of the reaction was signaled by a yellowing of the reaction solution due to the formation of suspended silver nanoparticles. Figure 3.1. shows a photograph of the Tollen's film fabrication setup taken approximately one minute after the noticeable color change.

Figure 3.1. Photograph of Tollen's film fabrication setup with samples suspended in the Tollen's reaction solution. The photograph was taken within 1 minute after the start of deposition as indicated by the yellowing of the solution.

After a light yellowing the solution color proceeded to run through dark yellow, brown, and finally gray as the suspended nanoparticles grew and aggregated. The color change was relatively rapid, with the entire change from clear to gray occurring over several minutes. The change from clear to noticeably yellow occurred in approximately 30 seconds, allowing us to use the first noticeable color change as

the zero of deposition time. This assignment was supported by a lack of deposition seen on samples removed before the change or within one minute after the change, while samples removed 1.5 minutes after the change showed measurable deposition. Panel (a) of Figure 3.2. shows an SEM image of a sample removed 1.5 minutes after the start of the reaction. We see a disperse distribution of silver nanoparticles deposited on the glass substrate with an average size on the order of $10nm$.

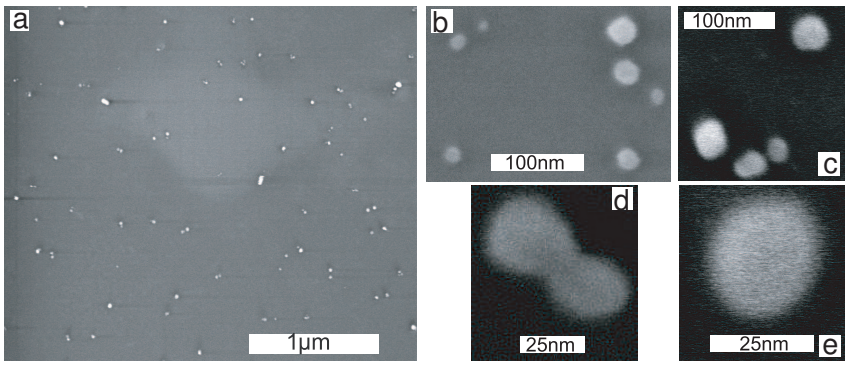

Figure 3.2. Scanning electron micrographs of silver nanoparticles deposited on glass using the the Tollen's method. Panel (a) shows a wide-view image of a sample removed 1.5 minutes after the initial yellowing of the solution. Panels (b)-(e) show high magnification images from a sample removed after 2.5 minutes, where the typical particle size is seen to be roughly $25nm$

Simply varying the time spent in the Tollen's reaction allowed us to fabricate nanostructured silver films with morphologies ranging from disperse, uniform distributions of nanoparticles to continuous films with micron scale roughness [61, 70, 120]. Intermediate morphological states include isolated islands, fractal structures, and highly porous, semi-continuous films. Figure 1.12. shows SEM

images of example films removed from the reaction at deposition times (in minutes): a)11.5, b)23, c)30, d)85, e)85, f)120.

After being removed from solution, one side of the substrates were wiped with a cotton swab soaked in hydrochloric acid. This removed the film from one side to prevent contamination of the SEM and the optical microscope that were used to study the films. The films were dried and stored in a nitrogen atmosphere, however this did not prevent the formation of a silver oxide layer on the films. The films were exposed to normal atmosphere while being wiped and prepared for storage and again when removed for SEM or optical measurements. The formation of a silver oxide layer on these films has been verified previously [119]. This study showed that an oxide layer roughly $3nm - 7nm$ thick was initially formed, with little increase in thickness afterward. The formation of a silver oxide layer in these films will be an important consideration in our study of the photoluminescence exhibited by these films, which is discussed in Chapter IV.

Tollen's Film Deposition Model

Models for film growth due to atomic deposition from the gas phase often include an atomic diffusion component, treated using a site hopping model [132, 143]. In this case the atom hops from site x_{i-1} to site x_i with a probability which is dependent on the height of the energy barrier for hopping, $P(\Delta E(x_i, x_{i-1}))$. The atoms will hop until settling into a site with a sufficiently deep potential such that

the probability per unit time for hopping out is much less than the characteristic timescale for the film growth [132, 143]. We have modeled silver particles in solution binding to the substrate or existing film in an analogous fashion.

We have developed a "hard cube" particle aggregation model of Tollen's silver film deposition. Individual silver particles are treated as impenetrable cubes subject to hard wall potentials with no spatial extent [141]. We observe silver nanoparticles forming in solution before measurable deposition occurs, indicated by the yellowing of the solution, and previous studies have found that the growth of silver nanoparticles by reduction of silver salts is dominated by particle aggregation rather than atomic adsorption. The formation of all the silver nanoparticles occurs on a timescale of seconds, and these particles then aggregate in suspension and on surfaces [144]. Considering the minutes long timescale required for measurable surface deposition we have ignored the initial particle formation stage of the deposition processes and only treat aggregation. The use of vigorous stirring during deposition provides a spatially uniform concentration of nanoparticles throughout the solution allows us to neglect local concentration gradients when developing the model.

The model assumes that the magnitudes of the particle-substrate and particle-film binding energies are much greater than $k_B T$. The van der Waals potential, $V(d)$ between two spherical particles of radii R_1 and R_2 separated by a distance d can be estimated using the Hamaker approximation, which assumes a superposition

of the molecular van der Waals interactions over the volume of the sphere [144]:

$$V(d) = \frac{AR_1R_2}{(R_1 + R_2)6d} \tag{III.2}$$

Here A is the Hamaker coefficient, which for bulk silver has a value of approximately $50 \times 10^{-20}J$ [144]. Using equation III.2 we calculate the van der Waals potential between two silver particles with $R_1 = R_2 = 20nm$ and $d = 4\mathring{A}$ (the silver lattice constant) to be $2 \times 10^{-19}J$, which is more than an order of magnitude greater than k_BT at the reaction temperature. Considering this result, we assumed particles do not return to suspension or reconfigure due to stress/strain and we only modeled particles hopping from solution onto the glass substrate or existing silver film. However, the effects of surface stress/strain energy do play a role in polycrystalline film growth and inclusion of these effects will likely improve the performance of the model and simulations [145, 146]. We will discuss the effects of neglecting surface strain/stress on our simulations results in the following sections and in the Conclusions to this chapter.

The probabilities per unit time for a particle to hop out of suspension and bind to a specific location on the substrate or to an existing particle in the film are defined as $P_g(\Delta E_g(x_i, x_{i-1}), C(t))$ and $P_s(\Delta E_s(x_i, x_{i-1}), f, C(t))$, respectively. Here $\Delta E_g(x_i, x_{i-1})$ and $\Delta E_s(x_i, x_{i-1})$ are the barrier energies for hopping onto the substrate and existing film, respectively and $C(t)$ is the time dependent particle concentration discussed below. We treat the probability for a particle to bind at a specific location where it will contact f neighboring particles to be

the sum of the probability for binding to each individual neighbor. In this case $P_s(\Delta E_s(x_i, x_{i-1}), f, C(t))$ is proportional to f.

Assuming the rate of particle loss by surface deposition and formation of macroscopic aggregates is proportional to the number of particles present, we expect an exponential decay of particle concentration in time. We treat the probability per unit time for a particle to arrive at any location on the film and bind as proportional to the particle concentration. In this case $P_g(\Delta E_g(x_i, x_{i-1}), C(t))$ and $P_s(\Delta E_s(x_i, x_{i-1}), f, C(t))$ have the form: $P_g(\Delta E_g(x_i, x_{i-1}), C(t)) = Ge^{-\gamma t}$ and $P_s(\Delta E_s(x_i, x_{i-1}), f, C(t)) = Sfe^{-\gamma t}$. The initial probabilities G and S are dependent on the unknown $\Delta E_g(x_i, x_{i-1})$, $\Delta E_s(x_i, x_{i-1})$, and initial silver particle concentration. Herein lies the strength of this model, where G, S, and γ, can be determined empirically and the computationally expensive modeling of lower-level atomistic processes is not needed to reproduce the correct film morphology. We have implemented this model in our film deposition simulations and used data acquired from SEM images to determine G, S, γ, and set the temporal and spatial mesh sizes of the simulations.

Simulation of Tollen's Film Deposition

Implementation of the model discussed above for computer simulations begins by defining a 3D simulation space containing empty volume pixels (voxels) and then defining a substrate surface. We then apply an MC type algorithm to each

voxel in order to determine if a silver particle binds at that location. At each iteration of the simulation every voxel is assigned a random number, r chosen from a uniform distribution over the interval 0-1. For each voxel sharing a face with the substrate surface where $r \leq Ge^{-\gamma t}$ the value at that voxel is set to 1, indicating a silver particle has bound at that location. The same basic process is used for voxels which share a number of faces, f with a previously deposited silver voxels, only in this case $Sfe^{-\gamma t}$ is compared to r. Here we have identified the number of shared voxel faces in the simulation with the number of contacted neighboring particles in the physical model. We have written our specific algorithm, which is applied to each voxel in the simulation space, in the format of the general MC algorithm discussed previously to allow for direct comparison:

1) Our model does not require an initial random number be drawn to determine the test state x_i. For any free particle at an unfilled voxel location there is only one availible test state, which is bound at that location. A particle already bound to the film or substrate will remain bound and no test state is needed.

2) For a particle at an unfilled voxel location in the unbound state x_{i-1}, the test state, x_i will be the bound state.

3) The model assumes the final bound state energy is always less than the free particle energy. However, we do not automatically bind a particle because

we must evaluate the probability that a particle will be found at the unfilled location. The energy barrier to binding, $\Delta E_g(x_i, x_{i-1})$ or $\Delta E_s(x_i, x_{i-1})$, must also be overcome for binding to occur.

4) The final bound state energy is less than the free particle energy. Acceptance of the new state will be determined by $P_g(\Delta E_g(x_i, x_{i-1}), C(t))$ and $P_s(\Delta E_s(x_i, x_{i-1}), f, C(t))$.

5) A random number r is assigned to each voxel.

6) The probabilities for a free particle to arrive at any location and then bind to the substrate or existing silver are $P_g(\Delta E_g(x_i, x_{i-1}), C(t)) = Ge^{-\gamma t}$ and $P_s(\Delta E_s(x_i, x_{i-1}), f, C(t)) = Sfe^{-\gamma t}$, respectively. If the particle is on the subsrate and $r \leq Ge^{-\gamma t}$ the particle binds, or if the particle is contacting the film and $r \leq Sfe^{-\gamma t}$ then the particle binds (the voxel is filled).

7) Otherwise do not fill the voxel.

8) Return to step 1.

Figure 3.3. shows the first two iterations of this algorithm for $G = 1/4$, $S = 1/3$, and $\gamma = 0$. Step of A of the figure represents the initially empty simulation space. Step B shows that 4 of the 16 free voxels contacting the substrate are filled. Step C shows that in the first iteration no voxels share faces with previously deposited silver. In step D a boolean addition of the results of steps B and C is performed to arrive at the total resulting deposition for the first iteration. We again see in

step B2 that 1/4 of the now 12 free voxels contacting the substrate are filled. Step C2 demonstrates that a silver particle is deposited onto 5 of the 15 available faces of previously deposited silver, corresponding to $S = 1/3$. This example does not demonstrate the effect of the neighbor contact factor f, however f will become more important as the complexity of the film surface increases. Finally, in step D2, a boolean addition is performed between the results of steps B2 and C2 to arrive at the final film produced in the second iteration, which is then fed into the 3rd iteration. Tracking the deposition onto substrate and existing film separately and performing the boolean addition allows us to easily separate the contributions of these two types of binding to the film growth at any time step. While we have used an MC-type algorithm in our simulations, we have not used a specific physical model to determine $P_g(\Delta E_g(x_i, x_{i-1}), C(t))$ and $P_s(\Delta E_s(x_i, x_{i-1}), f, C(t))$ *a priori*. Instead these parameters are determined by comparing structure in measured and simulated 2D projections of the films.

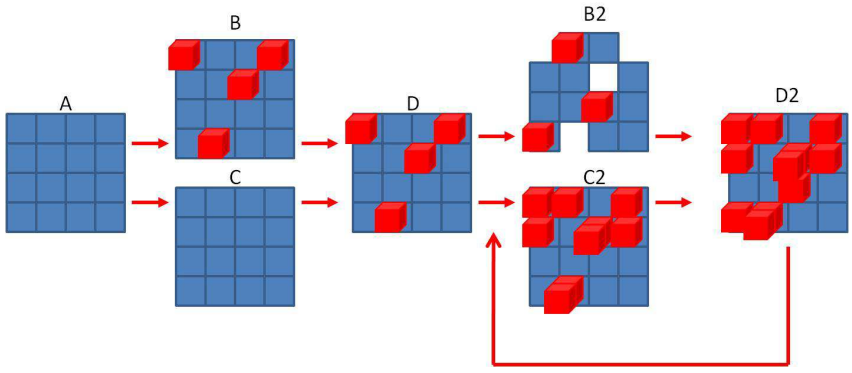

Figure 3.3. Diagram of the MC-type algorithm for simulation of Tollen's film deposition using example values of G = 1/4 and an S = 1/3.

Having discussed the model and its implementation for simulating Tollen's film deposition we will now describe our method for determining the simulation spatial scale, time scale, and model parameters G, S, and γ from analysis of SEM images of the films.

Analysis of SEM Images

Tollen's films were imaged using a FEI Quanta 200F SEM, providing $(1024 \times 880) pixel$ images with a $4nm/pixel$ scale factor. Higher magnifications were possible, however sample charging prevented resolution of structure below $4nm$ so we chose to sacrifice less than $4nm$ pixel scaling in favor of a large field of view. A low vacuum mode is used to reduce sample charging in the non-conducting samples. These images are then processed to maximize contrast and reduce non-uniform background illumination using built-in MATLAB image processing algorithms. The programs were then brightness thresholded using a user contributed MATLAB thresholding program[1] to produce boolean images of the films, which represent the 2D normal projections of the films onto the substrate plane. The threshold level is chosen to balance the minimization of noise due to charging and non-uniform illumination with the preservation of small and/or relatively dark silver features. Figure 3.4. shows an example SEM image and resulting 2D projection (boolean image) produced by this process.

[1]Threshold program contributed by Kateryna Artyushkova, Department of Chemical and Nuclear Engineering, University of New Mexico

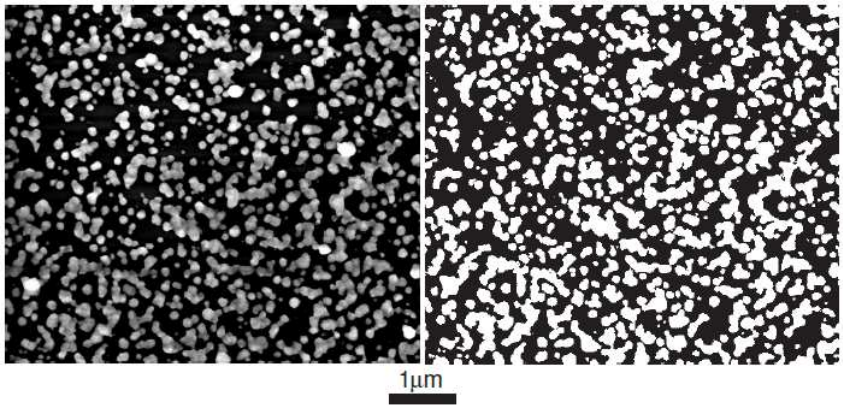

Figure 3.4. Comparison of an SEM image of a silver Tollen's film (left) and the boolean image produced by brightness thresholding the image (right). The boolean image represents the 2D normal projection of the film onto the substrate plane.

The surface coverage, (SC) is calculated as the ratio of white pixels to total pixels in the image. Defined this way, the surface coverage is an easily measured and controllable structural characteristic of the films. The SC will often serve as the independent variable in our examination of other film structural and optical properties in the remaining chapters. Figure 1.12. shows SEM images of films with varied morphologies corresponding to surface coverages: a)0.11, b)0.36, c)0.56, d)0.70, e)0.80, f)0.95. We estimated the error in the SC measurement by varying the threshold level of several images from extremely low (significant noise in the boolean image) to extremely high (a number of islands completely removed). The range in SC computed using the extremal thresholding levels serves as a conservative estimate of the error in SC due to sample charging, non-uniform illumination and user error or bias in executing the manual thresholding. Figure 3.5. shows the error in SC estimated in this way as a function of SC.

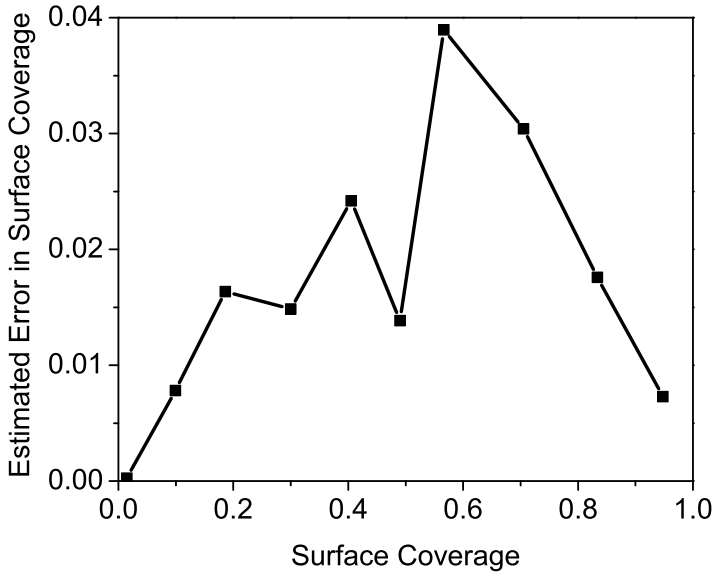

Figure 3.5. Conservative estimate of the error in SC measurement due to sample charging, non-uniform illumination, and user bias or error.

Individual silver islands are identified as a set of connected white pixels surrounded by black pixels, where pixels sharing an edge (4-connected) are considered connecting, but pixels sharing a corner (8-connected) are not. Figure 3.6. illustrates these connectedness definitions. The islands are counted, and the area, A of each island is computed by counting the number of pixels in the island. The radius of gyration, R_g of of each island is also calculated as:

$$R_g = \left(\frac{1}{A} \sum_{i=1}^{A} a_i \right)^{1/2} \tag{III.3}$$

where a_i is the distance of each pixel in the island from the island center of mass (each pixel is assigned one unit of mass) [147]. The R_g represents the radius of a ring with the same mass and moment of inertia as the original object. The R_g

measurement allows us to compare the size of asymmetric, spatially extended (non-compact) objects [147]. The relationship between R_g and A provides information about the spatial distribution of mass (pixels) in the object. Spatially extended dendritic objects will have a greater R_g to A ratio than compact, solid objects. Figure 3.6. shows two example islands with equivalent A and different R_g to illustrate how the R_g to A ratio assesses the compactness of an object.

The surface coverage measurement described here was used in determining model parameter values. The island R_g and A measurements were reserved for evaluating the validity of the model and accuracy of the simulations.

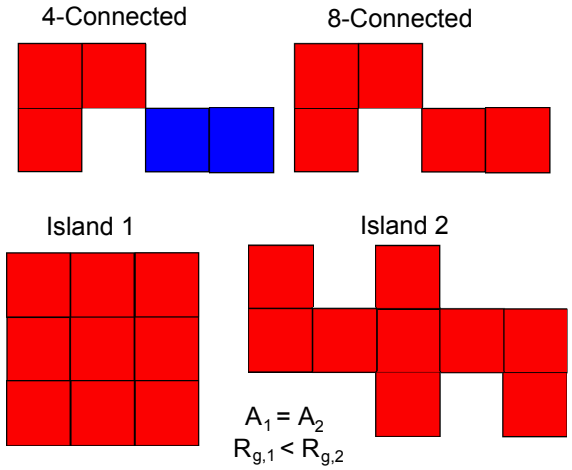

Figure 3.6. The top two pixel islands show the the 4-connected and 8-connected definitions of pixel connectedness. Under the 4-connected definition the set of pixels is counted as two islands. Under the 8-connected definition the pixels are considered as one island. We have used the 4-connected definition in our analysis. The bottom two islands demonstrate how the R_g measurement assesses island compactness. The two bottom islands contain the same number of pixels, but the R_g for the compact island on the left is less than for the spatially extended island on the right.

Determination of Model Parameters

Figure 3.7. shows the surface coverage plotted against deposition time. We can see from the data (blue squares) that deposition times of a few minutes produce SC values between 0.01 and 0.05, while $SC \approx 0.90$ after roughly 90 minutes. The maximum deposition rate is $\approx 0.025/min$. These results indicate that a simulation time step on the order of one minute will provide an accurate description of the film growth process. We have defined $P_g(\Delta E_g(x_i, x_{i-1}), C(t))$ and $P_s(\Delta E_s(x_i, x_{i-1}), f, C(t))$ as probabilities for binding *per unit time*. As long as the time step is on the order of one minute or less, the specific time step used will not affect the results of determining these parameter values. For convenience we set the simulation time step such that one iteration represents one minute of real deposition time.

The typical particle size at early deposition times is on the order of $10nm$ as seen in Figure 3.2., which shows an SEM images of a films with $SC < 0.03$. Specifically, the average island diameter measured in samples with $SC \leq 0.01$ is $24nm \pm 5nm$, thus we set the mesh size of the simulations at $24nm^3/voxel$. The effective coarse graining introduced to the model by using only a single constituent particle size of $24nm$ significantly reduces the computing requirements needed to simulate film growth over micron scale dimensions relative to atomistic simulations. However, this also prevents the reproduction of features less than $24nm$ in size.

In order to determine the substrate binding parameter, G we apply a fit to

measured $SC(t)$ data between zero and 20 minutes with an empirical function of the form $SC(t) = \beta(e^{\alpha t} - 1)$, which is indicated by the solid black line in Figure 3.7.. The form of the function was chosen such that $SC(t = 0) = 0$. The function does not reproduce the $SC(t)$ behavior beyond 20 minutes of deposition time because the growth ceases to be exponential for reasons that are discussed in the following sections. The fit produced parameter vales $\alpha = 6.19 \times 10^{-2} min^{-1}$ and $\beta = 0.11 \times 10^{-1}$ with a coefficient of determination of $R^2 = 0.83$. Evaluating the derivative of this function at $t = 0$ provides an initial growth rate, $dSC(t)/dt|_{t=0} = \alpha\beta$. The model and simulation algorithm dictate that the initial change in surface coverage over the first time step of the simulations is equal to G, thus we set $G = \alpha\beta = 6.8 \times 10^{-3} min^{-1}$. With respect to the simulations, this determines that the fraction of voxels sharing a face with the substrate that will be filled in the first iteration is 6.8×10^{-3}. With respect to the physical model this indicates that when deposition begins the probability per unit time at for a particle to arrive at a particular location on the substrate and bind is $P_g(\Delta E_g(x_i, x_{i-1}), C(t = 0)) = G = 6.8 \times 10^{-3} min^{-1}$. Without the effects of depletion this probability would not change. However, the exponential decay in particle concentration will cause an exponential decay in $P_g(\Delta E_g(x_i, x_{i-1}), t)$ as discussed previously.

The rate of film growth after the first few minutes is dominated by the effects of depletion and particle-film binding. This allows us to determine the particle-film binding parameter S and the depletion parameter γ from a χ^2 comparison of

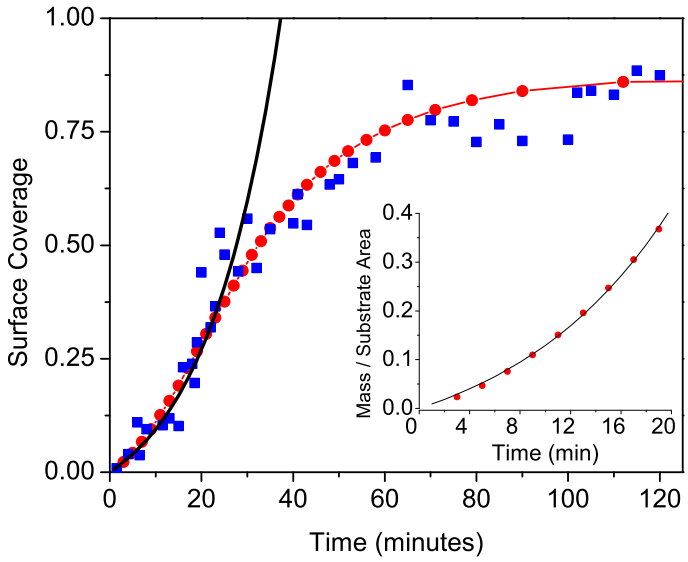

Figure 3.7. Dependence of surface coverage on deposition time for experimental films (squares) and simulated films (dots). The red line is a guide to the eye only. The black solid line is an empirical fit to the $SC(t)$ data for $t < 20$ minutes. (Inset) Simulated mass density (filled voxels per unit substrate area) plotted against deposition time (dots) and exponential fit to the data (line) showing exponential growth at early times.

experimental and simulated $SC(t)$ data across the entire range of deposition times (zero to 120 minutes). The parameters producing the best fit are determined to be $S = 5.2 \times 10^{-2} min^{-1}$ and $\gamma = 3.3 \times 10^{-2} min^{-1}$. With respect to the simulations this determines that the fraction of voxels sharing f faces with existing film that will be filled during iteration n is $(f)5.2 \times 10^{-3} e^{-0.033n}$. In terms of the model this indicates that at time t the probability per unit time for a particle to arrive at a location with f neighboring particles and bind is $(f)5.2 \times 10^{-3} min^{-1} e^{-0.033t}$.

The $SC(t)$ determined from simulations of film growth using the parameter values listed above is compared to the measured data in Figure 3.7. and we see

excellent agreement across all surface coverages (morphologies). The effects of the parameters G, S, γ on the features seen in the $SC(t)$ data are not independent, however the level of agreement seen in Figure 3.7. cannot be achieved by any other set of parameter values. For example, a larger S will cause $SC(t)$ to outrun the data. Increasing γ will counter this effect initially, however the roll-off in dSC/dT will be too sharp and will occur too early. When a lower S is used and γ is lowered to compensate, the opposite result occurs and the roll-off in dSC/dT occurs too late. The overall $SC(t)$ data is least sensitive to G, however the initial growth rate in the first few minutes is largely effected by G. The ability of the simulations to reproduce the measured $SC(t)$ across all surface coverages lends validity to our model as a relevant description of the physical deposition process. The order of magnitude difference in the values for S and G verify that particle-film aggregation is the dominant growth mechanism. We will discuss how these values determine the film growth mode in the following section.

Modeling and Simulation Results

Comparison of Simulated and Measured Tollen's Films

The accuracy of the simulations and validity of the model are evaluated by comparing measured and simulated 2D and 3D structural properties in the films. Figure 3.8. compares SEM images of Tollen's films to the 2D projections

of simulated films at several surface coverage levels to demonstrate the visual similarity. Also shown are 3D renderings of the simulated films, highlighting the 3D morphology.

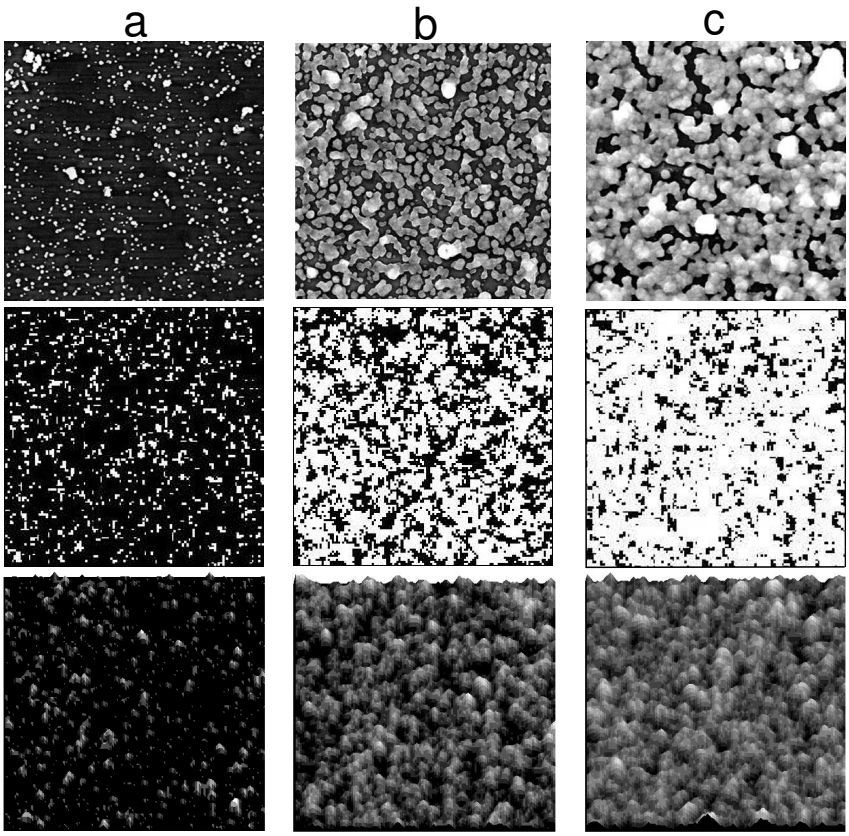

Figure 3.8. Comparison of SEM images of experimental films (top row) and 2D projections of simulated films (middle row) with equal surface coverage. White pixels represent the silver projection and black are substrate. Three-dimensional renderings of the simulated films are shown in the bottom row. The surface coverage of the films in each column are: column a)0.11, column b)0.56, column c)0.80. The scale of all images is $(3 \times 3)\mu m$ and the viewing angle for the 3D renderings is 14° off-normal.

A comparison of structural data extracted from 2D projections of simulated and measured films is shown in Figure 3.9.. The agreement between measured and

simulated data demonstrates the ability of the model to reproduce the measured film structure. Panels (a) and (b) show the average island area and standard deviation in the island area plotted against surface coverage, respectively. Panels (c) and (d) show the island number density and gyration radius to scaling parameter plotted against surface coverage, respectively. Many characteristics of the film growth processes are evident in the measured and simulated data. In panel (a) we can see that the average island area spans more than three orders of magnitude during the deposition process. While the average island area grows the standard deviation also grows by more than four orders of magnitude, indicating that both large and small islands exist at later stages of growth. This result can also be seen in the SEM image of the film with $SC = 0.80$ in Figure 3.8.. Here a few nm-scale islands are found surrounded by large connected network islands. We also notice in panel (b) of Figure 3.9. that for $SC < 0.1$ the simulated standard deviation in island area is consistently less than measured from SEM images. This is expected because the model uses only a single constituent particle size while a range of particle sizes are produced in the Tollen's reaction.

The simulated and measured island density data in panel (c) of Figure 3.9. demonstrates the effects of island coalescence. For $SC < 0.2$ the island density increases as new particles deposit on the the substrate. We see a peak in island density indicating that for $SC > 0.2$ the island number is reduced by coalescence more rapidly than new islands are added by substrate deposition. The relatively

sharp drop in island density seen near $SC \simeq 0.3$ indicates a sudden coalescence of many islands. This coalescing stage is an important contributor to the morphology dependence of the photoluminescence of Tollen's films. This details of this contribution are discussed in Chapter IV.

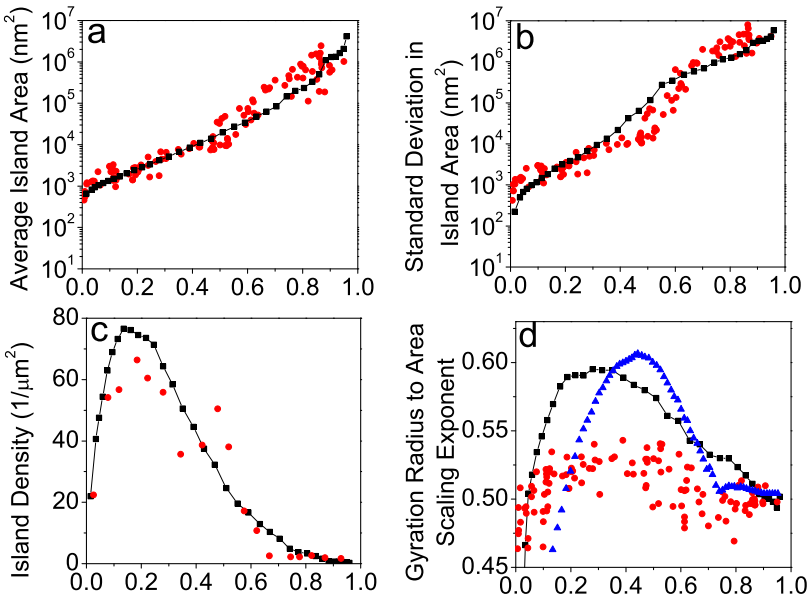

Figure 3.9. Comparison of film structural data extracted from simulations and measured using SEM. Horizontal axis for all plots is surface coverage. a)Dependence of average island area on surface coverage for experimental (dots) and simulated (squares) films. b)Dependence of standard deviation in island area on surface coverage for experimental (dots) and simulated (squares) films. c)Dependence of island density on surface coverage for experimental (dots) and simulated (squares) films. d)Radius of gyration to area scaling exponent as a function of surface coverage for experimental(dots) and simulated films (squares) and for randomly filled pixels (triangles).

A fundamental limitation of our model is evident in the more dendritic look of the simulated films seen in Figure 3.8.. In order to further explore this limitation we examine the relationship between island gyration radius, R_g and area, A. As

discussed previously, the R_g to A ratio measures the compactness of an object. A dendritic, spatially extended object will have a relatively large R_g to A ratio. Measuring R_g and A for the many individual islands in each sample allows us to determine the R_g to A scaling behavior. The scaling exponent, ν in the scaling relationship $R_g \propto A^{\nu}$, tells us about the level of dendricity of the islands in a given sample. If the projections of the islands were to remain compact (e.g. circular or square) throughout the deposition then ν would have a constant value near 0.5. However we see from SEM images such as those in Figures 1.12. and 3.8. that the islands are not compact at all surface coverages. Consequently ν depends on SC with larger $\nu(SC)$ indicating less compactness and higher dendricity in the islands at that surface coverage. We use dependence of the scaling exponent, ν on surface coverage as a measure of island dendricity throughout the deposition process [147]. Panel (d) of Figure 3.9. compares the measured and simulated $\nu(SC)$. While qualitative agreement is found, the $\nu(SC)$ for the simulated films is consistently higher than measured by SEM. This is consistent with the visual identification of more dendritic structure in simulated films Figure 3.8.. This discrepancy arises because our model lacks energy minimization components to reduce surface strain/stress energy. The curvature induced surface stress and strain in a metal film can constrain growth and induce boundary reconfiguration of regions with high curvature [145, 146, 148]. Our model neglects the effects of material stress/strain and consequently sharp dendritic structures are not preferentially

rounded off in the simulations, despite the opportunity for this to occur in the films. Future directions for this work include treatment of such effects in the model. We discuss this further in the Conclusions to this chapter.

The Tollen's Film Growth Mode

The order of magnitude difference in G and S results in Volmer-Weber type deposition, dominated by growth and eventual coalescence of individually formed islands [132, 149, 150]. This is consistent with the growing island morphologies seen in the SEM images in Figure 1.12. and indicated by the data in Figure 3.9.. Comparable values of G and S with $G < S$ in this model would result in both significant substrate layering and island growth, while for $G > S$, layered growth dominated by substrate deposition would be seen [132].

With the insight into the film growth provided by the simulations we can understand the form of $SC(t)$ in terms of our deposition model with $G << S$. At low $SC(t)$ there are many islands with high perimeter-to-area ratio and the majority of deposition occurs adjacent to existing islands (quasi-2D growth). In this case $dSC(t)/dt \propto SC(t)$, leading to the exponential form of $SC(t)$ seen for $SC < 0.2$. At low $SC(t)$ the mass is proportional to $SC(t)$ (indicating the film is approximately 2D) and this leads to an exponential time dependence for the film mass as well. This behavior is seen in Figure 3.7., which shows the simulated mass plotted against time along with a exponential fit to the data.

When the ratio of projected island areas to perimeters becomes sufficiently large the addition of mass is dominated by deposition on top of existing film, indicating a transition to full 3D growth. At this point the rate of mass deposition is proportional to the film surface area. Additionally, the mass is no longer proportional to $SC(t)$, but rather to average film thickness. This causes the exponential behavior of the mass time dependence for $SC > 0.2$ to become linear, as film thickness is constantly added. As SC increases the free substrate area $(1 - SC)$ decreases. This limits the number of locations where a particle can bind and contribute to an increase in SC, which prevents the continued exponential growth in $SC(t)$ for $SC > 0.3$.

Determining the 3D Structure of Tollen's Films

From the simulated films we are able to extract 3D structural properties and correlate them with 2D surface coverage. This bridges the problematic gap between easily measured 2D projections and difficult to characterize 3D structure. The now readily accessible 3D film properties include important parameters such as average thickness, volume filling fraction, surface area, and roughness of both the free and substrate sides of the film. In order to further test the structural accuracy of the simulations we use AFM to measure the surface roughness and average thickness of the films (WiTech Instruments alpha 300). Figure 3.10. shows two sample AFM images of films at different surface coverages. These images were exemplar, the

majority of the AFM images taken exhibited imaging artifacts due to cantilever ringing in high SC samples and particles sticking to the tip in low SC samples. This difficulty in acquiring artifact-free AFM data is a major motivation for simulation of film structure.

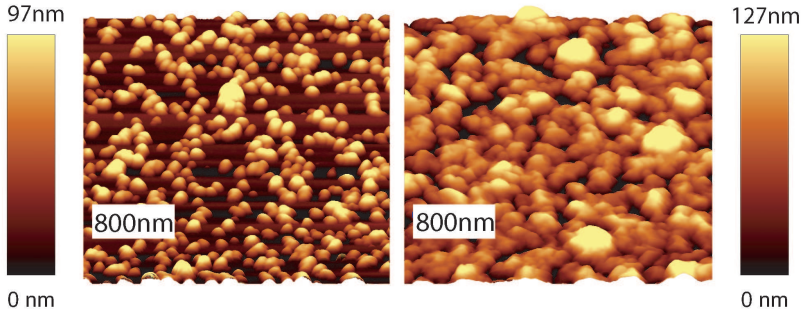

Figure 3.10. AFM images of chemically deposited silver thin films with surface coverage 0.24 (left) and 0.80 (right).

The average film thickness was measured as the average height of the film above the substrate. The surface roughness of the films was defined as the root mean square (RMS) of the difference between the height at each location and the average height. We expect that the measured topology will be affected by the finite size of the AFM tip [151], causing error in the 3D characteristics calculated from the measured topology. The AFM tip is unable to probe the entire depth of the film at every sampling point due to its finite size and consequent interaction with neighboring film structure. Figure 3.11. illustrates how the AFM tip is constrained by its size and the film structure surrounding the probe location.

The film roughness and thickness determined directly from the simulated

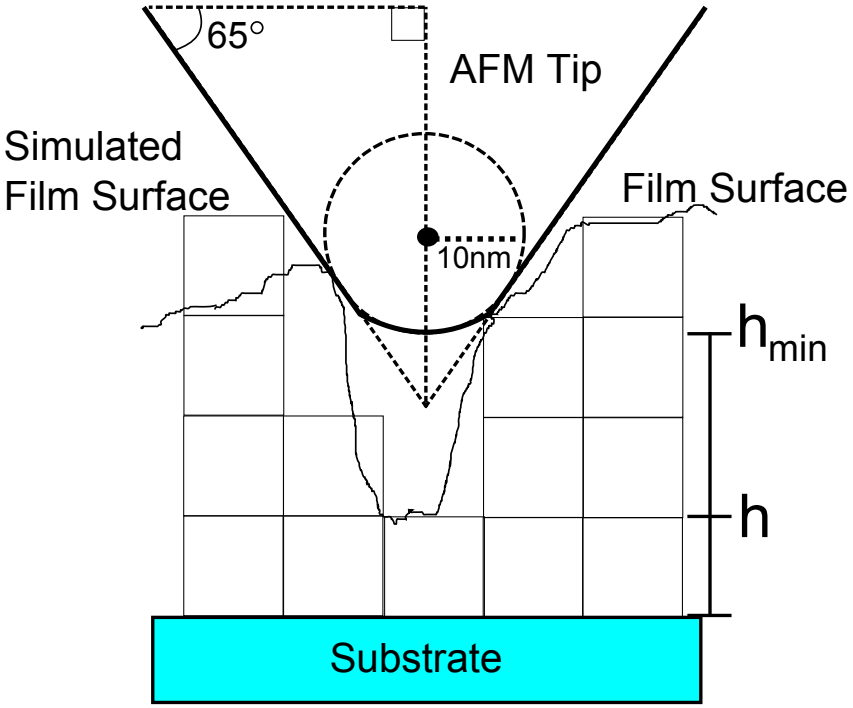

Figure 3.11. Schematic of the AFM tip geometry. The solid lines indicate the actual tip shape and dashed lines are references used to define the tip geometry. The tip is shown interacting with the silver film adjacent to the probe location, an effect which can introduce artifacts in the topography measured by AFM. The actual height h and the height that would be measured by the tip in the illustration, h_{min} are also shown. The boxes represent individual filled voxels in a simulated film and show how h and h_{min} can be calculated for a simulated film given a known tip geometry.

films do not suffer from tip-sample interaction artifacts. Considering this, we expect a discrepancy between the measured and simulated film thickness and surface roughness. Panels (a) and (b) of Figure 3.12. show the surface roughness and average thickness obtained directly from simulated films and from AFM measurements. We see in panel (a) that the rate at which film roughness increases with SC levels off above $SC > 0.5$ for the AFM data, but not for the simulation data. In panel (b) we see that the average film thickness measured by the AFM

is typically larger than for the simulations. We also see significant scatter in the AFM data due to the previously mentioned difficulties with AFM measurement on these films. These are exactly the discrepancies we expect to occur due to the finite probe size. At relatively high SC the film thickness and roughness are sufficiently large that the AFM tip cannot probe the entire depth at every location. This results in an artificially reduced roughness measurement. The thickness is instead increased artificially because some of the the lowest values of film thickness are not sampled.

We have used the simulated films to study the effect of the AFM tip geometry on the AFM measurement. At each point in the simulated film with actual height h we calculate the minimum height, h_{min} accessible by the tip when constrained by the height of the surrounding film and tip geometry. The tip geometry is shown schematically in Figure 3.11. along with h and h_{min}. The height measured by the tip is set to $h_{probe} = h$ for $h \geq h_{min}$ and $h_{probe} = h_{min}$ for $h < h_{min}$, producing an effective AFM measurement. The roughness and average thickness are then calculated from the simulated topology produced by this processes. These values show better agreement with the measured AFM data as demonstrated by the blue dots in panels (a) and (b) of Figure 3.12.. This result highlights an additional application of the model and simulations as tools for error and artifact analysis.

We can now exploit the film growth simulations to estimate 3D structural properties not easily accessed experimentally. For example, the AFM can measure

the topographic surface area of the film, however the area contributed by the bottom surfaces of any overhanging structures will not be counted. The volume filling fraction cannot be measured accurately by AFM or SEM because the contributions of overhangs and voids will not be probed. The tip geometry will also influence these measurements because some regions of the film will not be probed, as we have discussed above. Panel (c) and (d) of Figure 3.12. show the simulated volume filling fraction and surface area as a functions of the easily measured surface coverage, respectively.

Conclusions

We have developed a particle aggregation model of Tollen's film deposition which can be used for computationally lean film deposition simulations. The model and simulations are informed by data extracted from SEM images of the films, specifically the time dependence of the surface coverage. Comparison of simulated and measured films demonstrate that the model and parameter determination method capture the dominant effects in the deposition process. The simulations successfully describe the measured 3D structural features of surface roughness and average film thickness across the entire morphological range. The access and insight into the film structure provided by the characterization, modeling, and simulation work has addressed the first step in our goal of relating structure and optical properties in Tollen's films. With this work comes the opportunity for

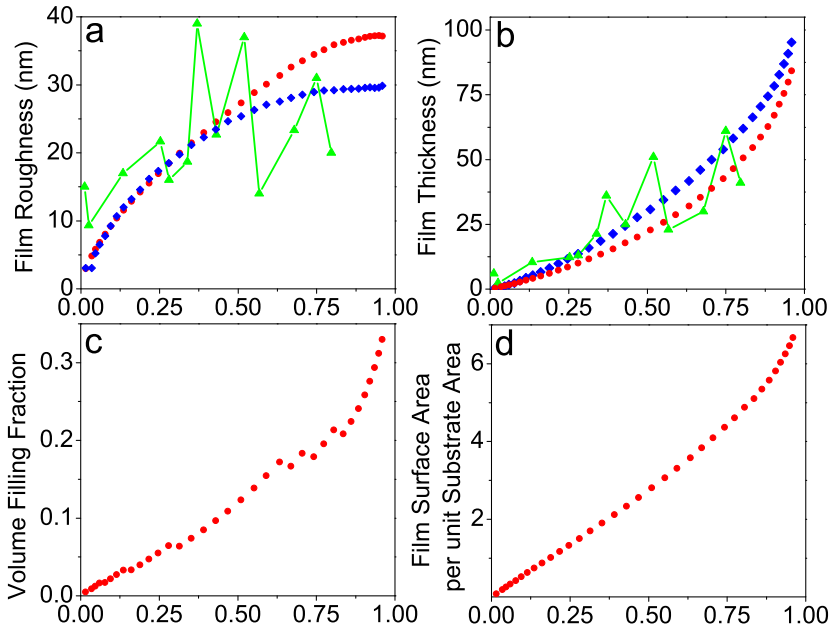

Figure 3.12. Three-dimensional structural properties as a function of projected 2D surface coverage determined from simulated films. Horizontal Axis on all plots is projected 2D surface coverage. a)Film roughness measured by AFM (triangles), calculated from simulated film (dots), and calculated from simulated AFM scan on simulated film (diamonds). b)Average film thickness measured by AFM (triangles), calculated from simulated film (dots), and calculated from simulated AFM scan on simulated film (diamonds). c)Volume filling fraction. d)Silver surface area per unit substrate area. Note the large variation seen in the measured AFM data demonstrating the difficulty in using AFM for characterization of these films.

greater understanding of the optical properties of the films. Additionally, the modest computing resources required by this model relative to molecular dynamics simulations may make it a valuable resource for experimental design and materials engineering.

Future work based on this model includes treatment of stress/strain energy minimization effects. This may help to address the previously discussed discrepancy in the level of dendricity seen in the simulated films, as indicated by the R_g

to A scaling behavior. A possible first step toward implementing such effects would be to make the binding probability dependent on the change in local surface curvature produced by the binding particle [145]. Additional improvements could be made by allowing for surface reconfiguration to reduce stress/strain energies; accounting for the relative crystal orientation of neighboring particles; and using more physically relevant distance-dependent binding potentials such as the Van der Waals potential [132, 135, 145].

All simulations here were performed on a desktop PC with a single 1.8GHz processor. Simulation of deposition up to $SC = 0.95$ lasted approximately one hour. At high SC the growth rate is slow due to the decay in the particle concentration and this increases the time required to simulate high SC films. Simulation to lower SC required significantly less time ($\approx 10min$). Inclusion of the depletion effect in the model is only required for accurate modeling of the time dependence of the growth because we have shown that the morphology of the films is dominated by the ratio of S to G. Under the conditions $G << 1$ and total substrate pixels $>> 1$, we can set the concentration decay constant, γ to zero in order to reduce the simulation run-time when only morphological information is desired. These stated conditions ensure that the simulated deposition happens over a sufficient number of iterations that the specific features of the model control the deposition process. Under these conditions the relative values for G and S control the deposition process and the Volmer-Weber mode still dominates the film growth. If these conditions are not met

then substrate and layer-by-layer deposition will dominate the growth, producing a relatively smooth structure.

Our characterization, modeling, and simulation work has provided a more thorough understanding of the film growth process. This work has also allowed us to optimize our methods for characterizing the microstructure of films across the entire morphological range. The next chapter will discuss how we have harnessed these results and applied them to our study of morphology dependent photoluminescence in nanostructured silver films. The insights in to the film growth process will prove invaluable to understanding how the photoluminescence is influence by the microstructure of the films.

CHAPTER IV

MORPHOLOGY DEPENDENT PHOTOLUMINESCENCE AND RAMAN SCATTERING IN SILVER TOLLEN'S FILMS

Introduction

Motivations for Studying the Photoluminescence of Tollen's Films

Nanostructured metal films play important roles in a variety of research and practical applications. Typically, silver or gold films are used to exploit the large electromagnetic (EM) field enhancement associated with the excitation of localized surface plasmons (LPSs) and the formation of EM field hot spots in the structures [4, 48, 50, 94, 123, 152–155]. The ubiquitous use of nanostructured metal films includes applications such as Surface Enhances Raman Scattering (SERS) [69, 123], biological sensing and imaging [76, 156], light harvesting [80, 81], random lasing [65, 86–88], and fluorescence engineering [68, 76–79, 157–159]. In order for these applications to reach their full potential, and to discover new ones, we want to understanding how specific optical phenomena are related to structural characteristics in these films [67, 94]. This knowledge will allow us to better

predict and tune optical properties *a priori* so that we may more quickly converge on structures optimized for particular applications.

Specifically, structure enhanced photoactivated photoluminescence (PL) is one unique optical phenomenon exhibited by nanostructured metal films which is not yet fully understood [67]. We have chosen to study the morphology dependence of the ensemble PL signal from silver Tollen's films for several distinct reasons:

1) The effects of the inherent PL signal on the applications discussed above are often neglected. The potential for exploitation of these signals in sensing applications has, until recently, been largely ignored. This work will lead us toward correct treatment of these signals and illuminate the possibility of exploiting these signals in bio/chemical sensing applications.

2) The PL is attributed to clusters of elemental silver a few nanometers in diameter formed at the film surface by photoreduction of silver oxide. This process results in a dependence of PL power on excitation wavelength, intensity, and film morphology [4, 67, 93, 160–164]. These dependences provide a rich data set through which to examine the relation between PL and film structure. Additionally, the approach we use to study the structure-PL relation is quite general and might be applied to nanostructured metallic films fabricated by other methods.

3) The PL efficiency from noble metal nanostructures is much greater than from

bulk metals and this has largely been attributed to the EM field enhancement effects discussed so far [67, 93, 165, 166]. However, the dependence of the PL power on structural properties is not yet fully understood [67]. The work described in this chapter will illuminate specific features of the film structure that dominate the ensemble PL and SERS response of these films.

4) The measured PL spectra of the films is typically combined with the SERS spectrum of environmental contaminants and both signals are intensity dependent [67, 165, 166]. This allows us to use the ensemble PL and SERS signals as probes for characterizing the structure dependent EM field enhancement in the films.

As discussed in Chapter I, we have broken our goal of relating the PL properties of disordered nanostructured films to their microstructure into two steps. The first step was to characterize film structure across a wide range of morphologies. The second step was to measure the PL across those morphologies and analyze how the PL is influenced by the film structure. In chapter III we discussed our work to address the first step by characterizing, modeling, and simulating the structure of silver Tollen's films. This chapter will describe our work to address the second half of the structure-optics challenge by measuring the ensemble PL and SERS signals from silver Tollen's films as functions of film structure. We will also discuss our analysis of these relations and the resulting insight into the EM field enhancement properties of the films. We will begin with an overview of the sources of the PL and

SERS signals in nanostructured noble metal films and conclude with a discussion of exploiting these signals for bio/chemical sensing applications.

Noble Metal Nanostructure Photoluminescence

Noble Metal Photoluminescence

Photoluminescence in bulk noble metals arises from excitation of electrons from the upper d-bands into the conduction band (s-p band) of the metal and the subsequent radiative recombination of the d-band holes with conduction band electrons [93, 167, 168]. Propagating photons at visible wavelengths have momenta much less than that of the electrons in the metal, thus the radiative excitation and recombination are direct. Luminescence is produced by radiative recombination of holes scattered by phonons and lattice defects to momentum states less than the Fermi wave vector, k_F, where the conduction band is filled [167, 168]. Figure 4.1. shows a general diagram of this noble metal PL process.

The PL exhibited by nanostructured noble metal films is attributed to clusters of metal atoms on the order of $2nm$ in size produced by photoreduction of metal oxide at the surface of the structures [67, 160–162, 164]. For convenience we refer to these elemental clusters as *nanoclusters*. Photoproduction and subsequent recombination of electron-hole pairs within the nanoclusters then leads to the photoactivated PL seen in the films. The PL exhibited by noble metal nanostructures is typically much

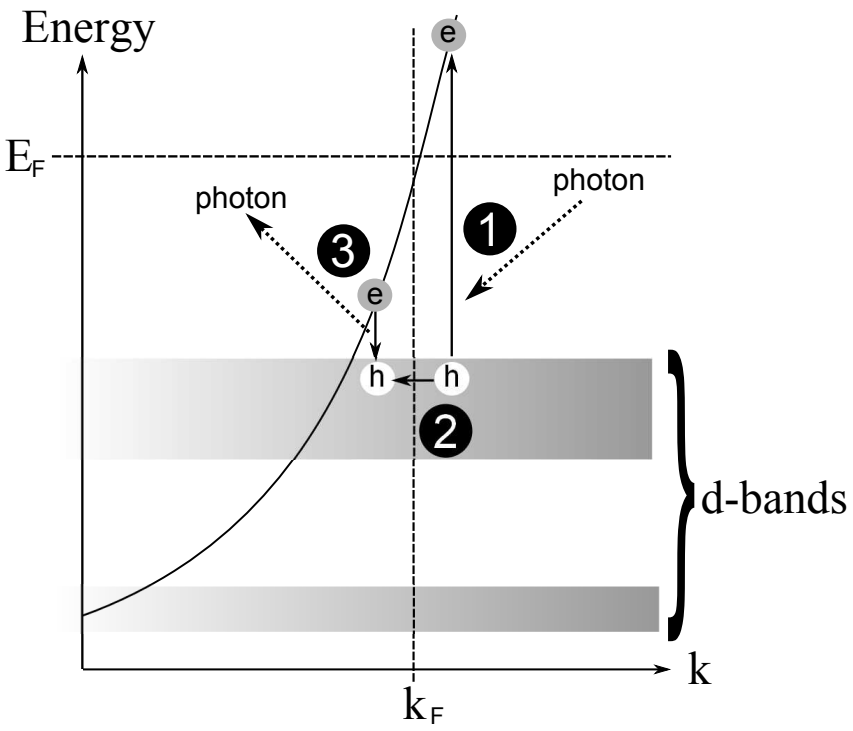

Figure 4.1. Radiative excitation and recombination process resulting in noble metal photoluminescence. 1)Excitation of an electron from d-band to conduction band by an incoming photon. 2)Hole is scattered to wave vector smaller than k_F. 3)Radiative recombination.

stronger than from bulk metal, with up to six orders of magnitude enhancement of the PL efficiency (fraction of photogenerated electron-hole pairs which radiatively recombine). This enhancement has been attributed to several effects, depending on the size of the nanocluster. The most obvious PL enhancement mechanism is EM field enhancement due to surface plasmon excitations and the lightening rod effect [67, 93, 165]. However, it has been argued that the one-to-two orders of magnitude field enhancement provided by these effects alone would not provide the level of enhancement seen in linear PL from noble metal nanostructures [169]. Additionally, noble nanostructures are found to exhibit PL even when the photon

energy of the excitation light is less than the bulk metal interband transition energy. This has been observed most notably in silver, where the interband transition energy ($4eV$) is nearly twice that in other commonly used noble metals such as gold and copper [67, 160, 164, 165, 170–172].

In general the PL efficiency can be enhanced by slowing the competing non-radiative decay processes or by accelerating the radiative decay process. Electrons in nanoclusters less than $2nm$ in diameter will experience size quantization of the free electron energy levels so that the clusters behave as quantum dots. Both the electron and phonon density of states are decreased as the cluster size decreases. This leads to diminished electron-phonon coupling as a competing non-radiadtive relaxation path and thus enhanced PL efficiency in the clusters relative to bulk metal [160, 169, 173–176]. As the nanoclusters grow larger than $2nm$ the size quantization is lost so that the clusters exhibit metallic behavior and the PL efficiency is decreased. The quantization and consequent reconfiguration of electronic energy levels also reduces the photon energy required to produce PL in the nanoculsters. This effect is crutial to our study where we have used an excitation wavelength of $532nm$, corresponding to a photon energy of $2.33eV$, which would not produce PL in bulk silver due to its $4eV$ interband transition [171, 172]. In the next section we discuss the intermittency (blinking) in PL emission from silver nanostructures. This blinking behavior further implicates the nanoclusters as the dominant source of the PL signal, as opposed to PL from the silver oxide

(Ag_2O) which has a bandgap in the visible at $552nm$ ($2.25eV$) and is known to exhibit only a relatively weak yellow PL [177].

Blinking Behavior in Photoluminescence and SERS from Noble Metal Nanostructures

The measured emission spectra of the films are a composite of the PL spectrum and the SERS spectrum of environmental contaminants, including nitrogen and carbon [67, 170, 178]. Both the PL and SERS signals show intermittency (blinking) similar to that of single molecules or quantum dots [67, 165, 166, 170]. Blinking behavior in molecules and quantum dots occurs due to competition between radiative and non-radiative relaxation processes. When the particle, either an electron or an exciton[1] is in an energy state for which the radiative relaxation time is much shorter than non-radiative relaxation time, then luminescence is observed (bright state). When the opposite is true, then non-radiative relaxation dominates and luminescence is suppressed (dark state).

For example, single molecule fluorescence blinking occurs due to non-radiative electronic transitions into and out of dark triplet states [179–181]. The dark triplet states are electronic energy levels in the molecules with opposite spin to the ground state so that transitions to these states are not induced by absorption of photons. Once photoexcited from the ground state to an optically accessible energy level,

[1] An exciton is a quasi-particle formed by Coulomb attraction between electrons and holes.

the electron may non-radiatively decay into the triplet state. The triplet relaxation lifetime can be relatively long (metastable) and fluorescence is suppressed until this relaxation occurs [182].

Quantum dot blinking is somewhat controversial, but the behavior has conventionally been attributed to the photoassisted charging and discharging of the dots. The photoassisted ejection of a charge leaves the core of the QD charged, which effects the ratio of the radiative to non-radiative recombination rates [183]. Uncharged (bright state) dots experience photoexcitation of electron-hole pairs (neutral excitons) and these radiatively recombine to produce fluorescence. For the case of charged (dark state) dots, photoexcition of a charged three-particle exciton comprised of an electron-hole pair and an extra electron occurs (trion). The timescale for non-radiative recombination of the trion[2] is much shorter than for radiative recombination and luminescence is quenched [184]. The photoassisted charging and discharging of the dots then produces a switching between bright and dark states.

The mechanisms behind noble metal nanostructure PL emission and its blinking behavior are not yet fully understood and much work to illucidate the fundamental physics underlying this phenomenon is ongoing [4, 67, 93, 160–166]. The blinking has been attributed to the size quantization of free electron energy levels in the photoproduced nanoclusters, resulting in blinking behavior analogous to that of

[2]Three-particle Auger recombinations provides a fast non-radiative relaxation pathway relative to radiative recombination.

quantum dots [160, 169, 173–175]. Additionally, the exact energy spectrum of the nanoclusters will depend on the size and shape of the clusters. This will cause temporal variations in emission power and wavelength from individual clusters as they change size and shape with continued exposure to light. Figure 4.2. shows a montage of real-color images extracted at one second intervals from a video recording of a Tollen's film during exposure to laser light with $15mW$ continuous wave (CW) power focused to a $1.3\mu m$ diameter spot on the film. The beam spot exposes an ensemble of emitters and the integration time was $17ms$. Under these conditions we sample an ensemble of intensities and blinking on/off times (flicker) rather than the on-off telegraph behavior characteristic of single emitters [184]. The time order of the images is left to right and top to bottom. We see the variation in signal power and color from specific locations within the beam spot as well as in the total signal power, demonstrating the flicker behavior of the combined PL and SERS signal.

Alternatively, blinking in SERS signals from metal nanostructures has been attributed to thermally driven rearrangement of molecules at the surface and the diffusion of molecules through variations in local EM field (hotspots). In this case laser induced heating in the nanostructures may provide a significant increase in diffusion and reorientation rates [185–187].

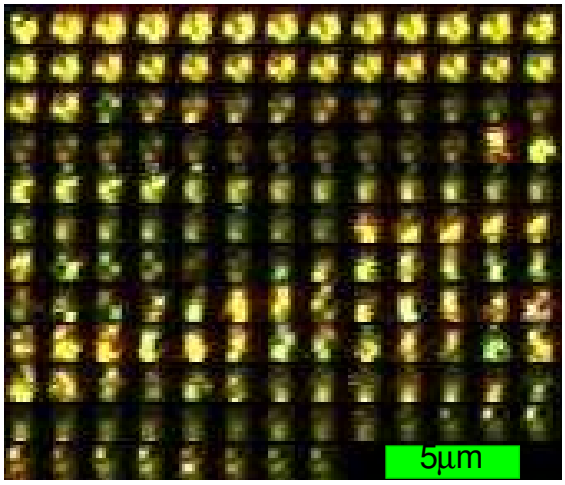

Figure 4.2. Montage of images of a silver Tollen's film under exposure to laser light, demonstrating the flicker behavior of the PL and SERS signal. The time order of the images is left to right and top to bottom.

Temporal Decay in Photoluminescence and SERS from Noble Metal Nanostructures

In addition to the blinking behavior of the PL and SERS, both signals also show a relatively slow decrease of the signal power with time. Typically we see the power decrease to half of the initial value over a timescale of $10 - 40$ seconds. Figure 4.3. shows the combined PL and SERS power measured using a $1s$ integration time at a wavelength of $538.8nm$ plotted against time. Here we see this decay as well as flicker (bursts of emission power) in the signal. The inset shows the the data from $1500s$ to $1600s$ in order to highlight the flicker behavior and demonstrate that it occurs on multiple time scales. The temporal decay in the signal appears similar to photobleaching seen in molecular fluorescence, which occurs due to photodestruction of the molecules [188]. However, for the case of noble metal

nanostructure PL this decay is attributed to a transition of the photoreduced atomic clusters from quantized to metallic behavior as the clusters grow with continued exposure to light [161, 170, 175]. The temporal decay in the SERS signal is attributed to the photo-assisted desorption of the surface contaminate molecules [118, 189].

Modification of the silver nanostructure surface due to heating by the incident laser light may also play a role in the decrease of both signals. This photo-annealing may reduce the sharpness of nanoscale features and thus diminish EM field enhancement effects [118]. Additionally, when a nanocluster is produced within a hot spot the SERS from nearby molecules may be diminished. The nanoclusers can competetively absorb a significant fraction of the optical energy from a hot spot due to thier relatively large absorption cross sections [190]. In this case the total SERS signal may be reduced with time as hot spots are quenched by formation of nanoclusters within them.

Our work has focused on understanding the effects of structure and morphology on the ensemble PL and SERS power and we have taken steps in this study to avoid artifacts in our measurements due to the flicker and decay in the signal. However, possible future directions for this work include the study of how signal decay and blinking behavior in the PL and SERS power are influence by film structure.

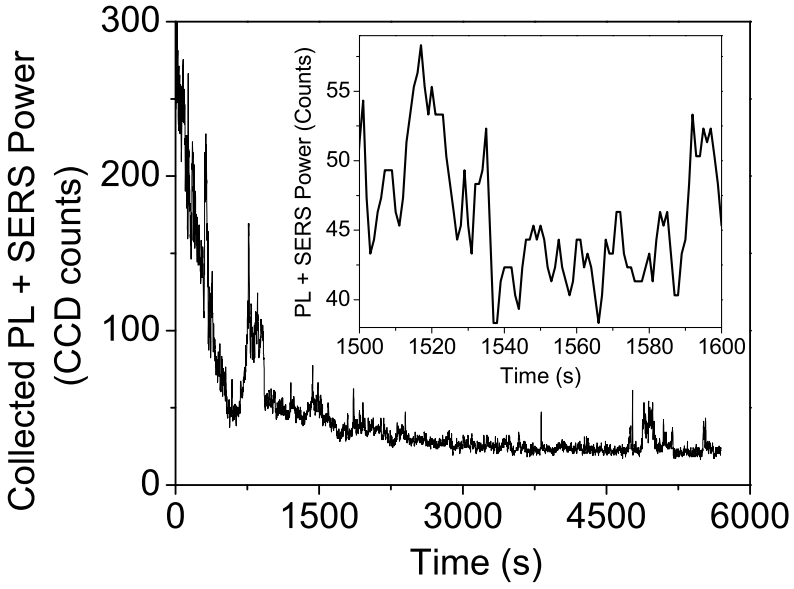

Figure 4.3. Time dependence of the combined PL and SERS spectrum at a collection wavelength of $538.8nm$. A decay of the measured power with time as well as flicker behavior are evident in the time series. The inset focuses in on the the data from $1500s - 1600s$ only.

Fabrication and Characterization of Silver Tollen's Films

We have used the modified Tollen's reaction described in Chapter III to fabricate silver nanostructured films with morphologies ranging from disperse nanoparticles to semi-continuous rough films [61, 70, 120]. As discussed in Chapter III, a $5nm - 7nm$ thick oxide layer forms on the surface of the films. The previously discussed formation of photoluminescent elemental silver nanoculsters by photoreduction of silver oxide occurs in this layer. The chemical composition of the film surface was analyzed by performing x-ray photoelectron spectroscopy (XPS) (Thermo Scientific Escalab 350) on test sample. The XPS measurement only probes the outer $5nm -$

Element	Atomic Percent (±0.1%)
Silver	7.3
Carbon	17.8
Calcium	1.1
Magnesium	0.4
Sodium	1.0
Oxygen	48.4
Silicon	23.9

Table 4.1. Chemical composition of the film surface determined by x-ray photoelectron spectroscopy.

$10nm$ of the sample surface, which is roughly the thickness of the oxide layer, thus expect to see significant oxygen content in addition to silver. We also see carbon (from atmosphere) along with trace amounts of calcium, magnesium, sodium, and significant silicon (from glass substrate)[3]. Table 4.1. shows the atomic percentage of each of these elements present at the sample surface.

The structural characterization techniques we developed in our study of Tollen's film growth were used to analyze the relationship between structure and PL in the Tollen's films. The films were imaged using a FEI Quanta 200F scanning electron microscope (SEM) and we applied the SEM image analysis methods discussed in Chapter III to measure structural properties of the films. The SEM images were thresholded to produce boolean images representing the 2D projection of the films onto the substrate plane. Figure 3.4. compares an example SEM image with the 2D projection of the film created by thresholding the SEM image.

Structural characteristics of the projections were then determined, including

[3]The x-ray photoelectron spectroscopy data was acquired and analyzed by Jason L. Fahrion of the CAMCOR microanalytical facility, University of Oregon.

the surface coverage (SC), island size distributions, and interface density, ρ. Three separate images were taken at different locations on each sample and the values for structural characteristics calculated from each image were averaged. Samples with measured SC values differing by less than the SC measurement error discussed in Chapter III ($< \pm 10\%$) were binned, and their characteristics averaged. The measure PL and SERS spectra of these samples were also averaged prior to their analysis by the methods discussed later in this chapter. The surface coverage is calculated as the ratio of white pixels in the projection to total pixels. The island sizes are calculated as the the effective island radius, $r = \sqrt{\frac{A}{\pi}}$, where A is the island area. Interface density is calculated as the ratio of total interface length total area of the image. The interface length is determined by counting the number of pixels edges shared by white and black pixels. Figure 4.4. shows an example boolean image with the total interface under this definition highlighted in red, which demonstrates that the interface contributed by voids in the metal film are included in the measurement.

The interface density measured in the films proves to be highly correlated with the PL and SERS power. The measured island size distributions and the insight into the film growth process gained from our modeling and simulation work have allowed us to understand this correlation in terms of EM field enhancement in the films. Our analysis of the relation between film microstrucure and PL efficiency will be discussed in detail in the following sections.

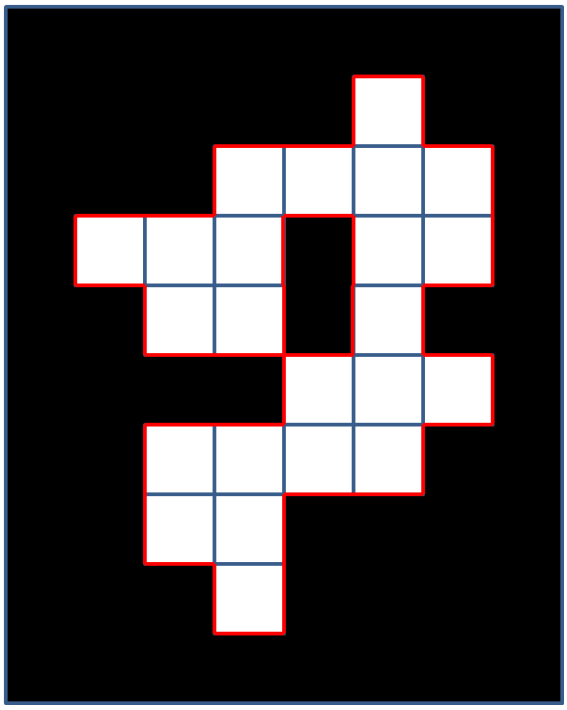

Figure 4.4. Example boolean image representing the normal projection of a silver island onto the substrate plane. The interface length is highlighted in red. The interface density is defined as the ratio of this length to the total substrate area.

Measurement of Photoluminescence and SERS from Tollen's Silver Films

Experimental Setup and Procedure

Combined PL and SERS spectra of the Tollen's films were measured using spectroscopic confocal microscopy with $5mW$ CW excitation power at a wavelength of $532nm$. In general confocal microscopy configurations are used to reduce collection of light originating from outside the focal plane of the collection lens [191]. In our experiments the confocal setup serves to discriminate against fluorescence from the glass substrate which is otherwise a significant source of noise in our

experiments. Figure 4.5. depicts the confocal setup we used (Witec Instruments alpha300) in our study. The collimated $532nm$ wavelength excitation laser light is incident on a 50-50 beam splitter, which divides the light power equally between transmission and reflection. The transmitted light is blocked and the reflected light is focused onto the sample by a microscope objective. The emission from the film is collected by the objective, along with reflected and scattered excitation light. Light emanating from the focal point of the objective lens is collimated by it, while light emanating from elsewhere is either diverging or converging after leaving the objective. The light is then divided again by the beam splitter with the reflected light being blocked. The transmitted light is sent to an edge filter which blocks light at wavelengths below $538.8nm$, including the scattered and reflected excitation light. Light at wavelengths above $538.8nm$ passes through the filter to a coupling lens. The collimated film emission which emerged from the focal plane of the objective is focused on to an aperture placed at the focal point of the coupling lens. The uncollimated light which emanated from locations other then the focal point of the objective is not focused to the focal point of the coupling lens and is therefore rejected by the aperture. The aperture also rejects a significant amount of the film emission signal which is scattered by the sample before being collected by the objective. As with any confocal setup a balance must be achieved between noise rejection and signal strength, typically by modulating the size of the aperture. In our setup the $125\mu m$ core of a multimode optical fiber served as the

aperture and the fiber itself served to couple the accepted light into a spectrometer (Princeton Instruments Acton SP2300).

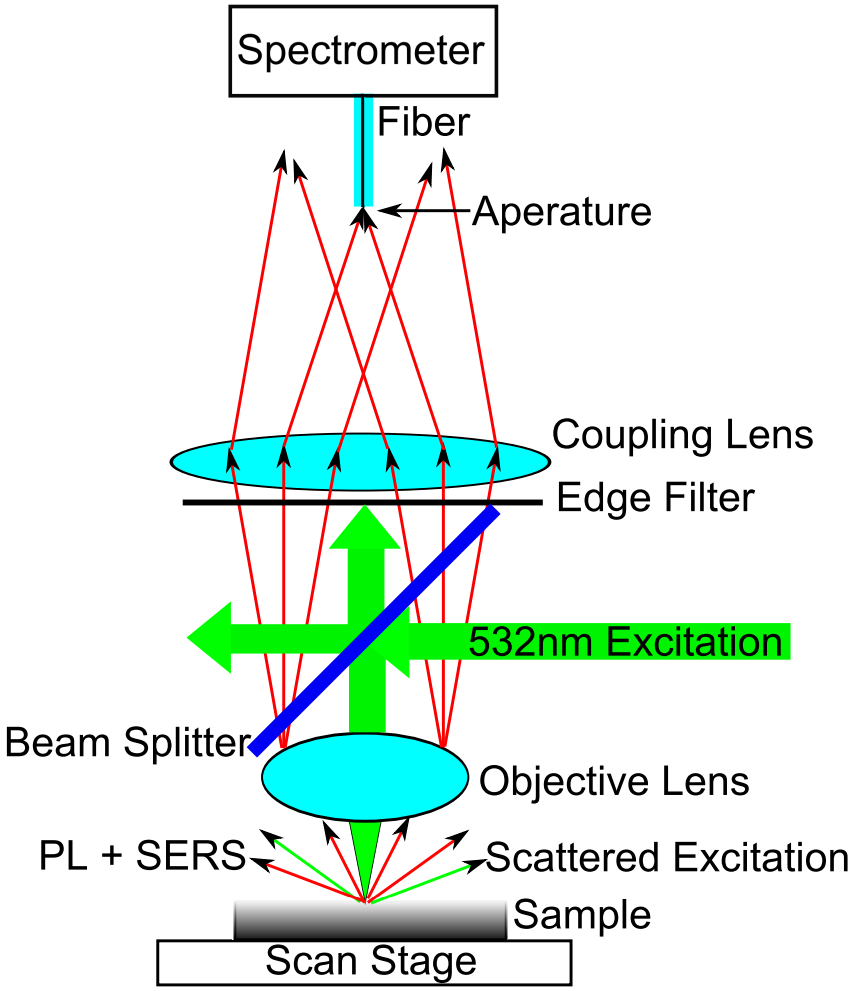

Figure 4.5. Diagram of the confocal spectroscopy setup used for measurement of PL and SERS in silver Tollen's films. The diagram is not to scale.

The excitation beam was focused to a spot with $2.6\mu m$ diameter (Nikon 10X objective with numerical aperture 0.25) and emission spectra collected from 27 distinct locations on each sample were averaged. A one second integration time at each location was used to avoid sampling the decay in emission power with time,

which occurs over a timescale of $10s - 40s$. The large spot size relative to the largest features in the films ensures an ensemble PL and SERS measurements rather than sampling of individual silver nanoclusters or contaminant molecules [67]. However, it has been shown that the PL and SERS signal enhancements experienced by nanoclusters and molecules located in hot spots, which may be as large as 10^6 and 10^{14}, respectively, can cause an ensemble signal to be dominated by a small number of sources if a low number of hot spots is sampled [14, 48, 67, 93, 165, 169]. Measuring many distinct locations on the sample addresses this issue and also averages over slight variations in surface coverage within a sample. These averaging steps also average over signal power variations due to blinking, which would otherwise introduce significant noise to our measurements. The size relations between the $2.6\mu m$ beam spot and the structural features in the films across all morphologies are shown in Figure 4.6.. We see that at low surface coverages ($SC < 0.4$) the beam spot encompasses hundreds of individual silver islands. At mid-range values of surface coverage ($0.4 < SC < 0.7$) the spot averages over significant silver and non-silver regions without having the spot area dominated by any particular substrate or silver region. For high surface coverages ($SC > 0.7$) the spot covers many large structural variations in the silver as well as many ($\approx 25 - 50$) dielectric voids.

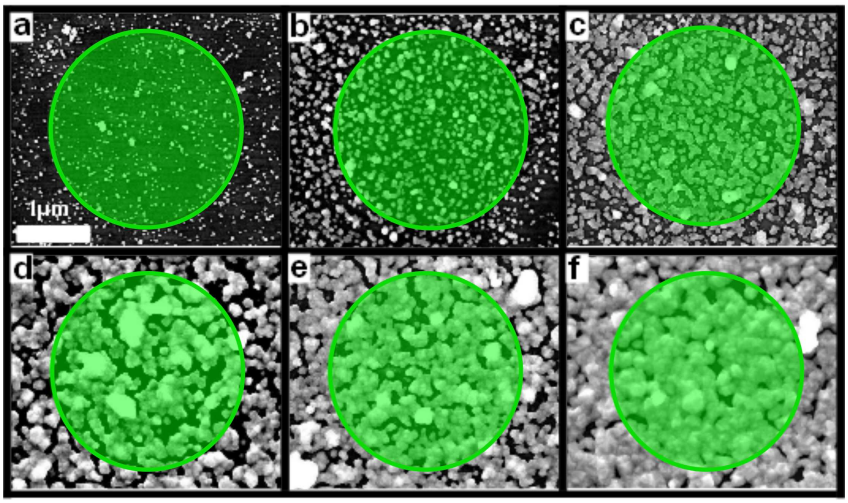

Figure 4.6. Scanning electron microscope images of Tollen's films with overlay representing the $2.6\mu m$ spot diameter of the focused excitation beam. The surface coverage values of the samples are: a)0.11, b)0.36, c)0.56, d)0.70, e)0.80, f)0.95.

Removal of Background Substrate Luminescence

Prior to decomposing the PL and SERS contributions to the measured spectrum we subtract the bias level signal and the luminescence of the glass substrate. The CCD bias level induced an artificial signal of 174 counts at all wavelengths, as mesured by recording a spectrum with the laser blocked. This bias level was subtracted from all measured sample spectra.

The luminescence spectrum of the of the glass substrate alone, along with the measured spectrum from samples with $SC < 0.26$ are shown in panel (a) of Figure 4.7.. We see a broad luminescence spectrum from the glass with a significant peak at $564nm$, indicated by the arrow in panel (a) of Figure 4.7.. For $SC > 0.25$ the peak was washed out by the emission signal from the silver film. We determined the dependence of the glass luminescence power on surface coverage by measuring

the height of the $564nm$ peak above the background of the glass luminescence and silver film emission. As seen in panel (b) of Figure 4.7., we found that the measured glass luminescence power decreased roughly linearly with surface coverage for $SC < 0.26$, where the height of the $564nm$ peak was measurable. Considering this data, we have subtracted a background from all measured sample spectra equal to the luminescence spectrum measured from the bare glass substrate multiplied by $(1 - SC)$. Panel (c) of Figure 4.7. shows the original spectra in panel (a) after subtraction of the glass luminescence according to this procedure. The shallow dips in the corrected spectra at a wavelength of $564nm$ indicate that this method overestimates the glass contribution at low surface coverages. The relative size of this error decreases rapidly as SC increases, both because the silver emission signal grows and because the glass luminescence decreases. In the next sections we will see that the PL and SERS power at $SC < 0.15$, where this error is significant, is sufficiently small compared to the signals at $SC > 0.15$ that this error does not affect our analysis.

While the EM field enhancement provided by the silver films may enhance the substrate luminescence somewhat this was not a significant source of error in our measurements. We see in Figure 4.7. that the substrate luminescence is nearly washed out by the PL and SERS signals from the silver film. The film emission signals continue to grow with increasing surface coverage while simultaneously less glass is exposed to the excitation laser. The features of the glass luminescence,

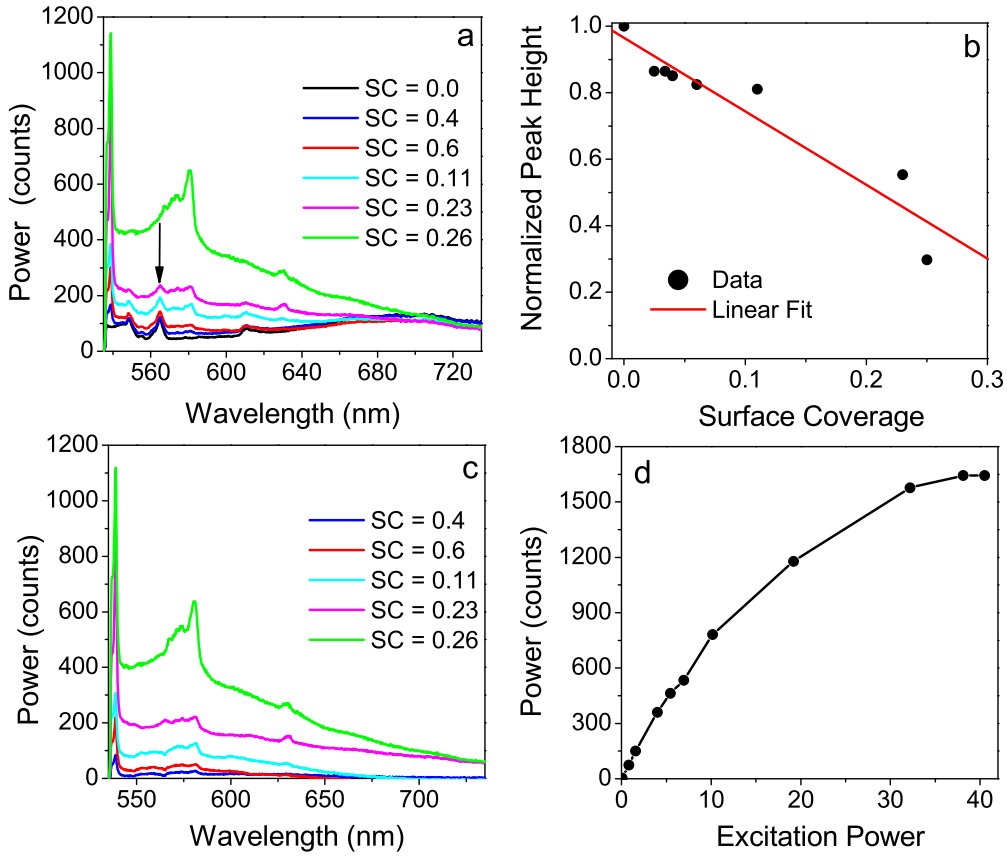

Figure 4.7. Panel (a) shows measured film emission and glass substrate luminescence spectra from films with $SC \leq 0.26$. The bare glass substrate is labeled $SC = 0$ in the figure legend. The arrow indicates the glass luminescence peak at $564nm$, which used to determine the dependence of the glass luminescence power on SC. Panel (b) shows the height of the peak in the glass luminescence at wavelength $564nm$ normalized to the height for a bare glass slide and plotted against surface coverage. We see a linear dependence for $SC \leq 0.25$. Panel (c) shows the spectra in panel (a) after subtraction of the glass luminescence. Panel (d) shows the dependence of the glass luminescence power on excitation power. The connecting lines are a guide to the eye only.

including the distinct $564nm$ peak are not noticeable above the noise in the silver film PL background for films with $SC > 0.25$, indicating that the glass luminescence is not providing a significant contribution to the spectrum. We also see in panel (d) of Figure 4.7. that the glass luminescence power shows a weaker than linear

dependence on excitation power. The PL and SERS signals show a linear and quadratic dependence on excitation power, as will be discussed later in the chapter. Considering these results, any EM field enhancement provided by the film should only decrease the relative contribution of the substrate luminescence to the total measured spectrum.

In order to verify that none of the spectral features in the measured PL and SERS signals were due to the specific substrate used we also deposited a silver film on a silicon substrate. The spectrum measured from this film is shown in Figure 4.8., along with the spectrum from the bare silicon, the combined PL and SERS spectra from a $SC = 0.33$ silver film and the bare glass substrate luminescence spectrum. We can see that all the features of the silver film combined PL and SERS spectrum are present for the film on the silicon substrate. The silicon Raman lines at wavelengths $547nm$ and $560.3nm$ (relative Raman shifts $515cm^{-1}$ and $1044.5cm^{-1}$, respectively) are marked with arrows on the figure [192]. The spectrum from silicon with no silver film verifies that the source of these lines is the silicon substrate. Note that the respective spectra in Figure 4.8. have been normalized by different factors, and different excitation powers were used in the experiments to allow for convenient comparison of the spectral features.

Decomposition of PL and SERS Spectra

In order to examine the structure dependence of the PL and SERS signals we

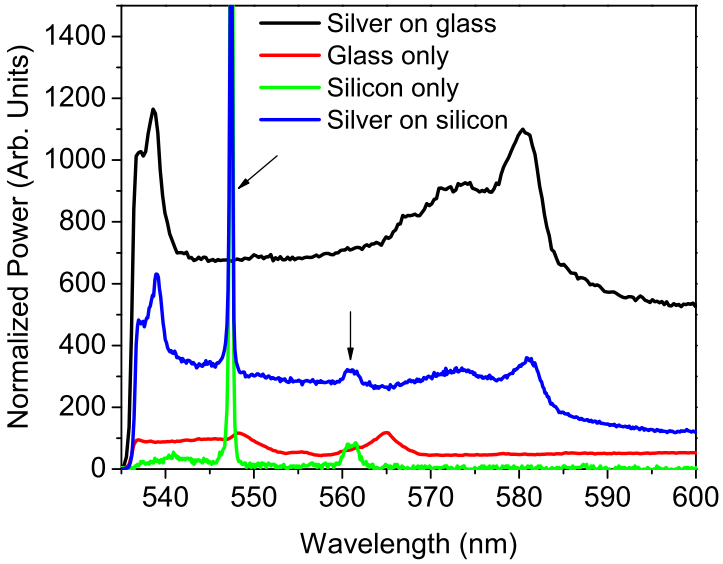

Figure 4.8. Combined PL and SERS spectra of silver films deposited on glass and on silicon substrates along with the Raman spectrum from the bare silicon and the luminescence spectrum from the bare glass. The sharp lines seen in the samples containing silicon are the silicon Raman lines at wavelengths 547.0nm and 560.3nm (Raman shifts 515cm^{-1} and 1044cm^{-1}, respectively)

.

first decompose the measured spectra into the constituent PL and SERS spectra. To decompose the spectra we determine the PL contribution by performing a 3rd order polynomial fit to the data in three smooth spectral regions not containing significant SERS peaks. With the PL signal determined by the fitted function, we then subtract the PL background from the total spectrum to arrive at the SERS spectrum. Figure 4.9. shows a representative measured spectrum along with the decomposed PL and SERS contributions determined by the fitting and subtraction procedure. Figure 4.9. also shows the spectral regions used in the fitting procedure

and identifies the contaminant sources of the SERS peaks. Table 4.2. identifies sources of the major SERS peaks at wavelengths $538.8nm$, $573.9nm - 580.7nm$, and $628.4nm$ [67, 170, 178] according to thier relative Raman shifts. The contaminant sources are atmospheric nitrogen (Ag-N), the carbon-carbon double bond (C=C), and carbon crystallites formed on the film surface (Carbon) [67, 170, 178, 193]

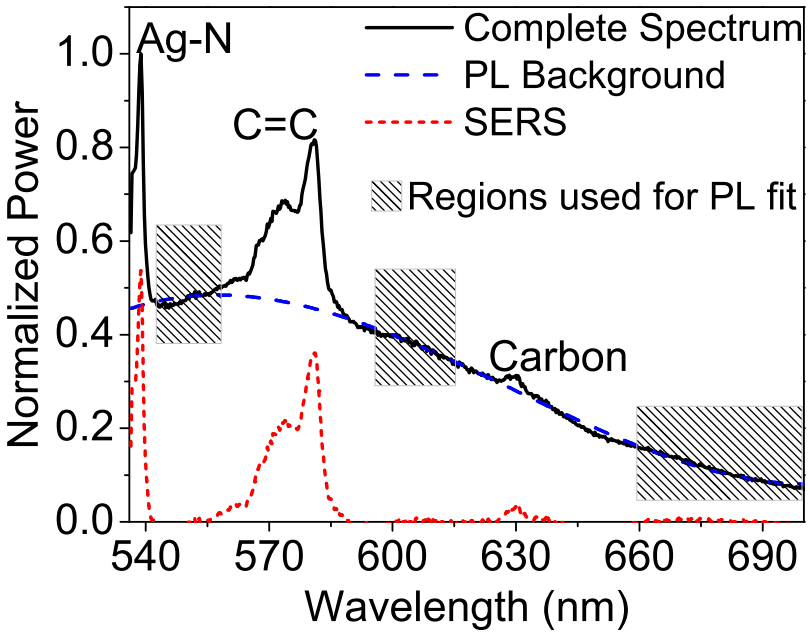

Figure 4.9. Panel (a) shows an example measured spectrum from a silver Tollen's film with surface coverage of 0.42. The black solid line is the measured spectrum normalized to the maximum signal. The SERS peaks are labeled with their environmental contaminant sources on this measured spectrum. The blue dashed line is a 3rd order polynomial fit to the data in the hatched spectral regions away from the peaks, giving the background PL spectrum. The red dotted line is the SERS spectrum obtained by subtracting the fitted PL background from the total signal.

Wavelength nm)	Relative Raman Shift(cm^{-1})	Source
538.8	237	Ag-N
573.9-580.7	1372-1576	C=C
628.4	2883	Carbon

Table 4.2. Spectral location of the SERS peaks for an excitation wavelength of $532nm$, together with the Raman shift and adsorbed contaminant sources of the peaks.

Power Dependence of PL and SERS in Tollen's Silver Films

Determining how the PL and SERS signals scale with excitation field intensity will be important to understanding how structure dependent EM field enhancements influence these signals. With the measured spectrum decomposed into the underlying PL and SERS spectra, the dependence of PL and SERS power on excitation power, P_{ex} was determined. In the upcoming analysis we have assumed that the excitation intensity at the focus of the laser is proportional to the measured P_{ex} because the beam spot size is constant. As discussed below, the SERS signal scales quadratically with P_{ex}, which verifies $P_{ex} \propto$ intensity [49]. Figure 4.10. shows the measured dependence of PL and SERS power on P_{ex} at the locations of the major spectral peaks (wavelengths $538.8nm$, $573.9nm$ and $580.7nm$). Also shown are fits to the data which allowed us to extract the P_{ex} scaling exponents.

Table 4.3. shows how the PL and SERS signals at each wavelength scale with P_{ex}. We see that the PL power at all wavelengths scales similarly with P_{ex}, giving

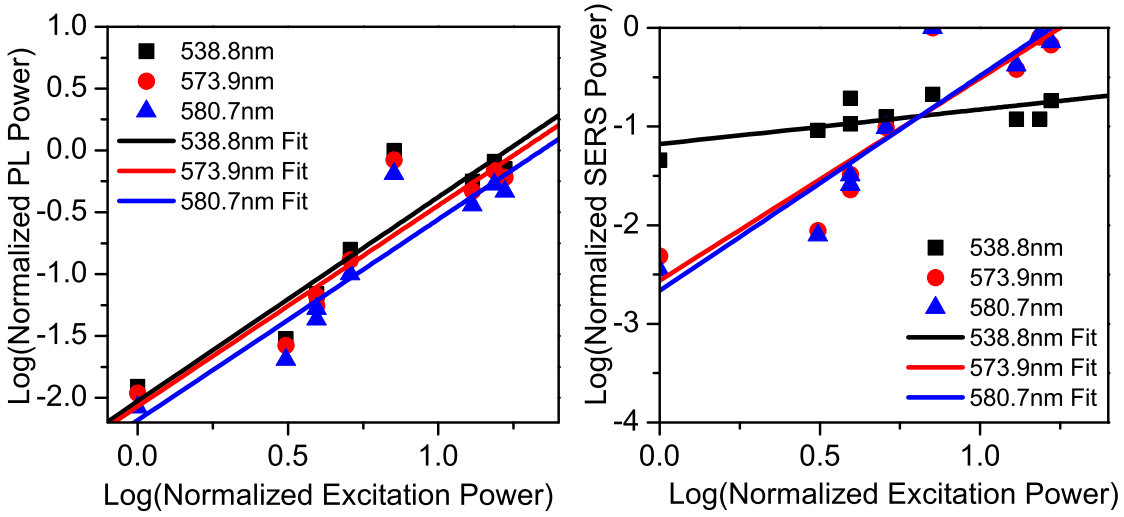

Figure 4.10. Log(PL Power) (left) and Log(SERS Power) (right) plotted against Log(P_{ex}) at wavelengths 538.8nm (black squares), 573.9nm (red dots) and 580.7nm (blue triangles). The solid lines are fits to the data at each wavelength: 538.8nm (black line), 574nm (red line) and 580.7nm (blue line).

an average scaling exponent of $\alpha_{PL} = 1.6 \pm 0.3$. We can understand this scaling by approximating the ensemble PL power as $P = NaP_0$, where N is the number of nanocluster emitters per unit area, a is the beam spot area, and P_0 is the average single emitter power. The measured $\alpha_{PL} = 1.6$ for the PL power is then attributed to P_0 showing the expected linear scaling with P_{ex} while $N \propto P_{ex}^{0.6}$. This assignment is supported by previous studies which have shown a linear scaling of the PL power with low total impinging photon number followed by a roll off with higher photon number [67, 162]. This roll-off occurs because N is limited by the available film surface area and surface stoichiometry, and because the nanoclusters become less efficient emitters as they grow and become metallic [160, 161, 164, 169, 170, 173, 174].

Wavelength(nm)	PL to P_{ex} scaling exponent	SERS to P_{ex} scaling exponent
538.8	1.7 ± 0.3	0.4 ± 0.2
573.9	1.6 ± 0.3	2.0 ± 0.4
580.7	1.6 ± 0.3	2.2 ± 0.4

Table 4.3. PL to P_{ex} and SERS to P_{ex} scaling exponents measured at the wavelengths exhibiting SERS peaks.

The 573.9nm and 580.7nm SERS peaks show the expected quadratic dependence on P_{ex}, with an average scaling exponent of $\alpha_{SERS} = 2.1 \pm 0.4$. The 538.8$nm$ peak behaves differently, exhibiting saturation behavior at relatively low P_{ex} that results in a scaling factor of $\alpha_{Ag-N} = 0.4 \pm 0.2$. This saturation is attributed to photoinduced desorption of nitrogen from the film surface [118, 189].

Morphology Dependences of PL and SERS in Tollen's Silver Films

We measured the emission spectra of films with $0.03 < SC < 0.80$, which spans a range of sample morphologies from disperse nanoparticles and aggregates to semi-continuous rough films with nanoscale voids. We have found that the PL and SERS power show non-monotonic dependence on film morphology, including a sharp peak for all wavelengths near $SC \simeq 0.3$, as seen in Figure 4.11.. We see that the peak is sharpest for the 573.9nm and 580.7nm SERS signals followed by the PL power, and finally the 538nm SERS signal. The strength of the dependence on P_{ex} for these signals follows the same order, which suggests that an EM field enhancement mechanism is responsible for the peak. As discussed previously, the

EM field enhacement properties of the films are structure dependent, so we attribute this peak to the unique morphological characteristics present in the films near $SC \simeq 0.3$. We have used the insights gained from our previous work on characterizing, modeling, and simulating the film growth to determine the dominant structural features producing the peak. We now discuss the morphology dependence of the film emission in the context of the varying microstructure present in the films throughout their growth.

The Volmer-Weber growth mode exhibited by these films results in island density and island size eventually becoming sufficiently large that significant coalescences of many separate islands into fewer larger islands is enabled [194]. Our experimental analysis and simulations use the 4-connected definition of island coalescence discussed in Chapter III. Under this definition, two previously separate islands have coalesced when their 2D projections form a single 4-connected set of pixels. The coalescing stage of growth will be signaled by a decrease in the island number density which occurs when coalescence begins to lower the island number more quickly than new islands are added by substrate deposition. The left panel of Figure 4.12. shows the measured and simulated island number density plotted against surface coverage for the Tollen's films. We see a peak occurring near $SC \simeq 0.2$ followed by a sharp drop at $SC \simeq 0.3$, indicating a relatively sudden coalescence of many islands. This sudden coalescence also indicates that just before it occurs a significant fraction of the islands are separated by nanoscale

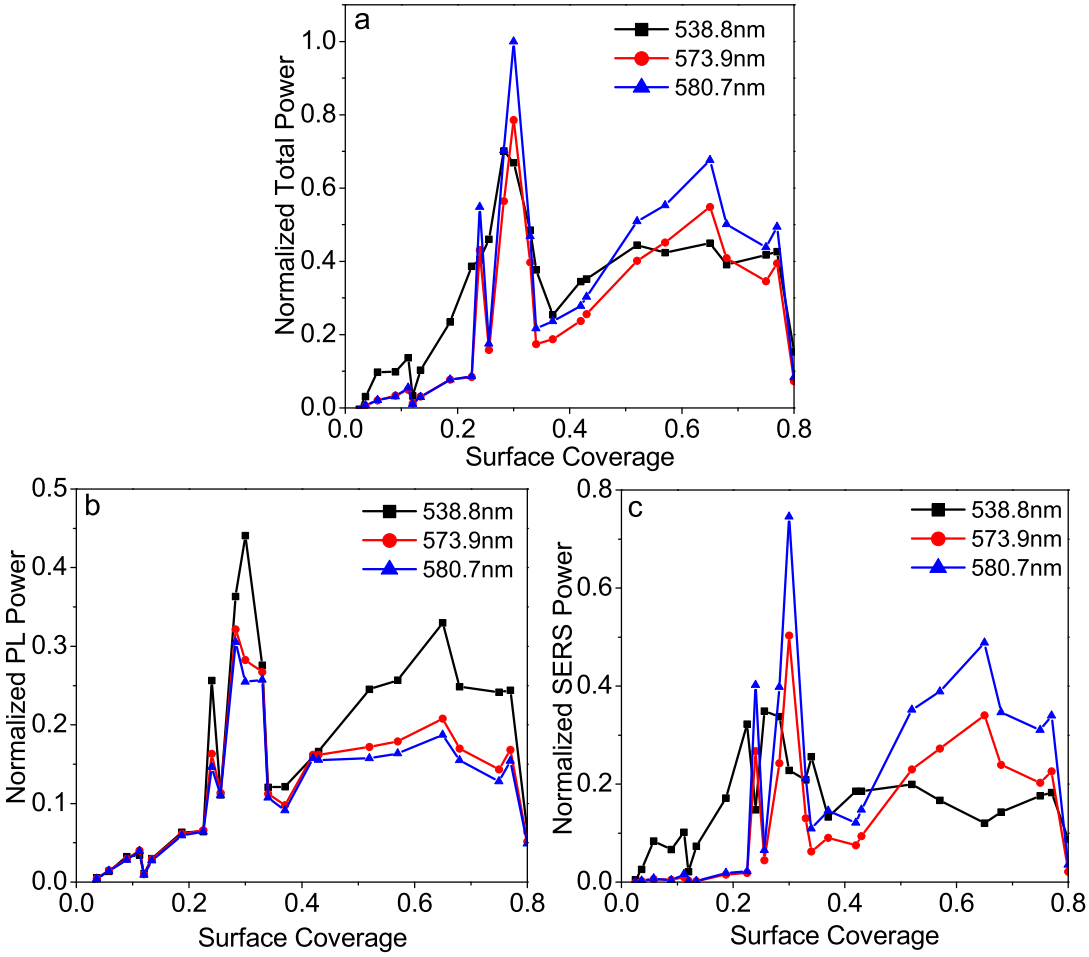

Figure 4.11. Measured PL and SERS power normalized to peak value in the combined PL and SERS spectrum, and plotted against surface coverage. Panel (a) is the combined PL and SERS power, panel (b) is the PL power only and panel (c) is the SERS power. We see the relative contributions of the PL and SERS power to the total varies with surface coverage and we see a significant peak in both PL and SERS power near $SC \simeq 0.3$. Colors designate wavelength according to the legend in each panel. Connecting lines are a guide to the eye only.

gaps, which is an important structural characteristic that we will discuss in greater detail below. These nanoscale gaps between islands can be seen in Figure 4.13., which shows an SEM image of a sample with $SC = 0.30$. This sample exhibited the largest PL and SERS signals of all those measured.

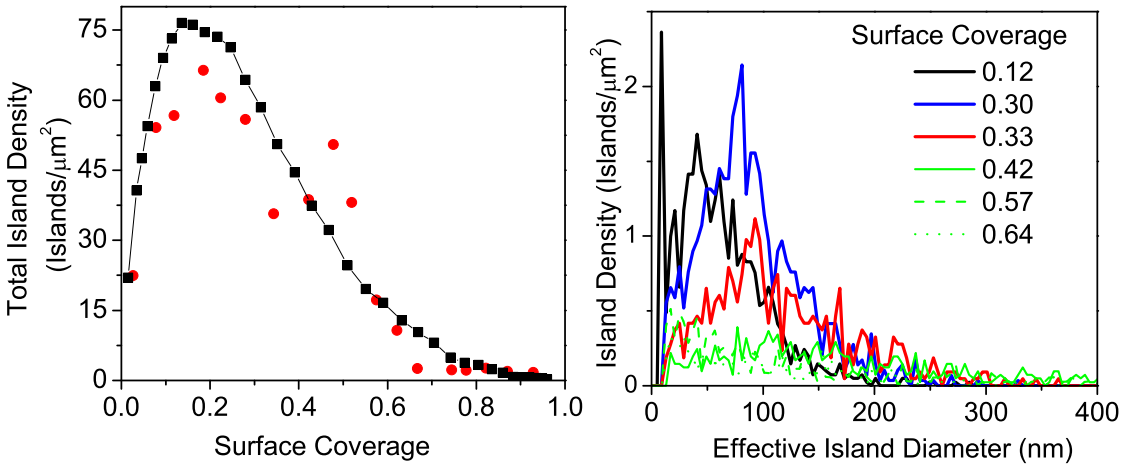

Figure 4.12. The left panel shows the measured and simulated island number density plotted against surface coverage, showing a turn-over in island density near $SC \simeq 0.2$ due to the onset of coalescence. The sharp drop in island density near $SC \simeq 0.3$ indicates sudden significant coalescence. The right panel shows the measured island size distributions of Tollen's films before and during coalescence. The distributions change dramatically between $SC = 0.33$ and $SC = 0.42$, indicating the relatively sudden occurrence of significant coalescence.

Closer inspection of the island size distributions across a wide range of surface coverage further demonstrates the occurance of a relatively sudden coalescence growth stage. The right panel of Figure 4.12. shows island size distributions for films with $0.12 < SC < 0.64$. We see that for $SC < 0.33$ the distributions continue to broaden and shift toward larger sizes as the islands continue to grow. Reduced integrated area under the distributions indicates some decrease in the total island density due to the onset of coalescence. Between $SC = 0.33$ and $SC = 0.42$, the distributions change dramatically and become nearly uniform across the size

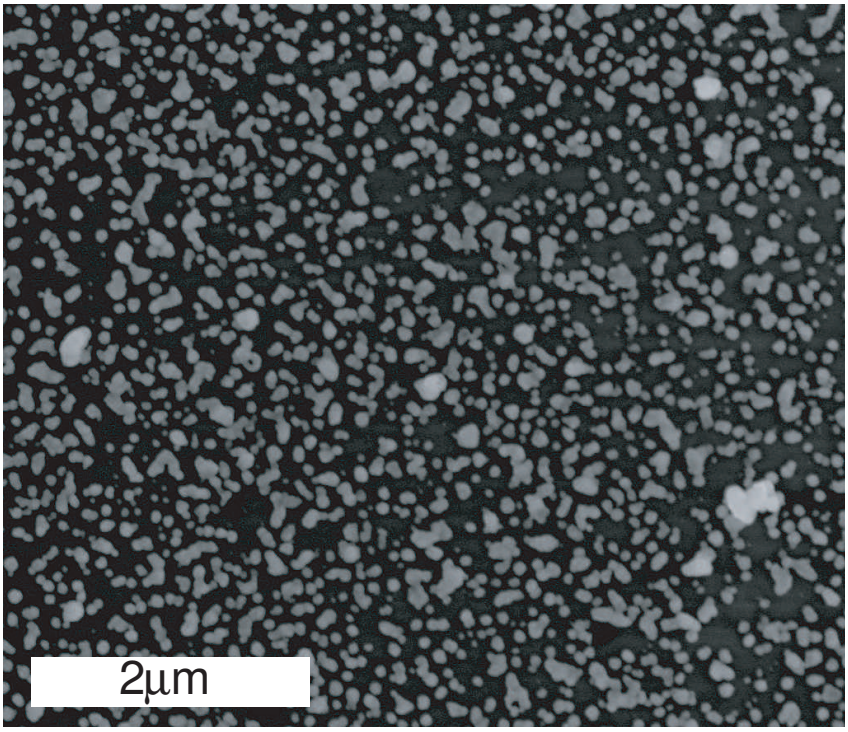

Figure 4.13. Scanning electron micrograph of a Tollen's film with $SC = 0.30$ This specific sample produced the largest PL and SERS signals of all samples measured.

range with a significantly smaller integrated area, signaling the occurrence of island coalescence.

Interface Density as a Predictor of Tollen's Film Emission

A direct implication of the sudden coalescence phenomenon is that just before it occurs there exists a high density of nanoscale gaps with small average gap distance. This effect can be seen in Figure 4.13., which shows the SEM image of a sample with $SC = 0.30$. This indicates that the projected interface density, ρ will also be maximized at this point because there exists a maximum density of islands with

relatively large perimeters. Further island growth results in a loss of ρ as the gaps are filled and islands lose perimeter in the process of coalescing. This result may be counterintuitive considering that the multiscale self-similarity present in fractal structures is typically associated with maximal interface density [195]. However, the films are not ideal fractals and their interface density is limited by finite size effects [48]. When sufficient island coalescence occurs such that a connected island network (a single island under our definition) spans the entire sample, then the *percolation threshold* is reached and the film becomes electrically conductive [48, 70, 119, 196]. The percolation threshold has been shown to occur near $SC \simeq 0.7$ in these types of films [70, 119]. The formation of large connected island networks near the percolation threshold gives rise to a fractal film structure as self-similarity at multiple scales is produced. The formation of these connected networks occurs by coalescence and thus comes at the cost of some island perimeter and ρ. Without limits on feature size, the continued addition of ρ at smaller and larger scales could continue *ad infinitum* and ρ would increase over-all. However, these films are not ideal fractals and their self-similarity is limited at the large scale by the sample size and on the small scale by the size of individual particles forming the aggregate islands. In this case the loss of island perimeter to coalescence causes an over-all reduction in ρ after onset of the coalescence stage. Consequently, the maximum ρ is measured to be near $SC \simeq 0.3$, as discussed in the following section.

Previous studies have established that the excitation EM field intensity can

be enhanced by an order of magnitude within nanoscale gaps between metallic nanostructures. Figure 4.14. shows the the EM field intensity enhacement factor produced in a $2nm$ gap between two silver nanoparticles. The figure was taken from reference [197], where the EM fields were calculated using the discrete dipole approximation[4].

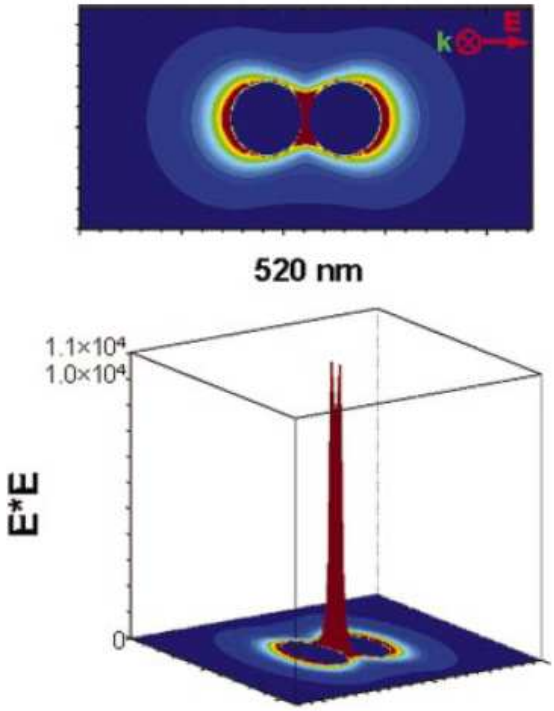

Figure 4.14. The top figure shows the electric field enhancement countours near two silver particles separated by $2nm$. The contours are shown for a plane that lies along the inter-particle axis and passes midway through the particles. The polarization of the incident electric field was parallel to this plane. The bottom figure shows 3D plots, where the axis perpendicular to the selected contour plane represents the electric field enhancement factor. The figure was taken from reference [197], where the enhancments were calculated for an incident wavelength of $520nm$ using the discrete dipole approximation.

[4]The discrete dipole approximation treats an object of arbitrary shape as an array of individually polarizable elements. The response of the object to an external EM field is found by self-consistently determining the induced dipole moment in each element.

The gap-field enhancement is known to increase non-linearly as the gap distance decreases, with the exact scaling behavior determined by the geometry of the structures. [4, 196–202]. Additionally, the EM field intensity enhancement provided by LSP excitations is localized to the silver-air interface [4]. Consequently, we expect the ensemble PL and SERS power to be relatively enhanced when the density of nanoscale gaps and interfaces are maximized and the average gap size is minimized [67]. Figure 4.15., taken from reference [67] shows SEM images of films with varied morphology and the PL images produced by the films. We see a nonmonotonic dependence of the hot spot density on growth time, indicating a nonmonotinc dependence on surface coverage. In this study the optical properties were related to growth time and the structure was not studied specifically so the density of hot spots and PL emission were only qualitatively related to the film morphology. However, we can see from the figure that the maximal hot spot density occurs at a film morphology similar to that of the sample in Figure 4.13., which produced the maximal PL signal in our study.

In order to quantitativly relate the hot spot density and light emission to film structure we investigate the relation between ρ and the PL and SERS emission. Figure 4.16. shows the dependence of the PL and SERS power on surface coverage. Here the signals have been normalized to the maximum signal measured at each respective wavelength. The measured interface density, ρ is also plotted against surface coverage for comparison. We see a striking similarity in the behavior of the

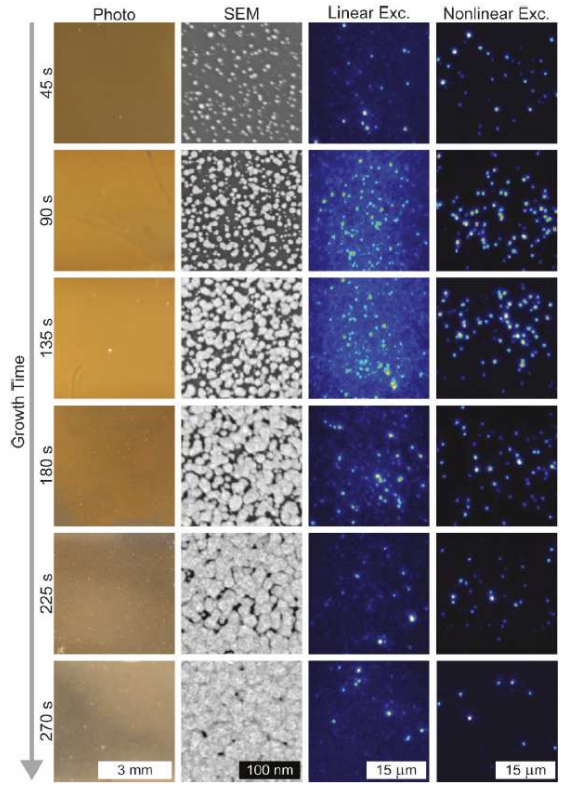

Figure 4.15. Influence of Tollen's film morphology (controlled by growth time) on the EM field hot spot density. First column are photographs of the films, second column are SEM images, third colum is linear PL emission, and fourth column is nonlinear PL emission. This figure was taken from reference [67].

independent optical and structural measurements. This indicates that ρ plays a major role in determining the PL and SERS power. We also see that ρ is maximal near $SC \simeq 0.3$, just below the surface coverage where the sudden island coalescence was seen to begin, and where the PL and SERS signals are maximal. We can also see that the relative height of this maximum in the PL and SERS signals increases with the strength of the signal dependence on P_{ex}. This suggests that their correlation with ρ is due to the role of ρ in determining the EM field enhancement properties

of the films. To investigate this further we examined how the film emission scales with ρ.

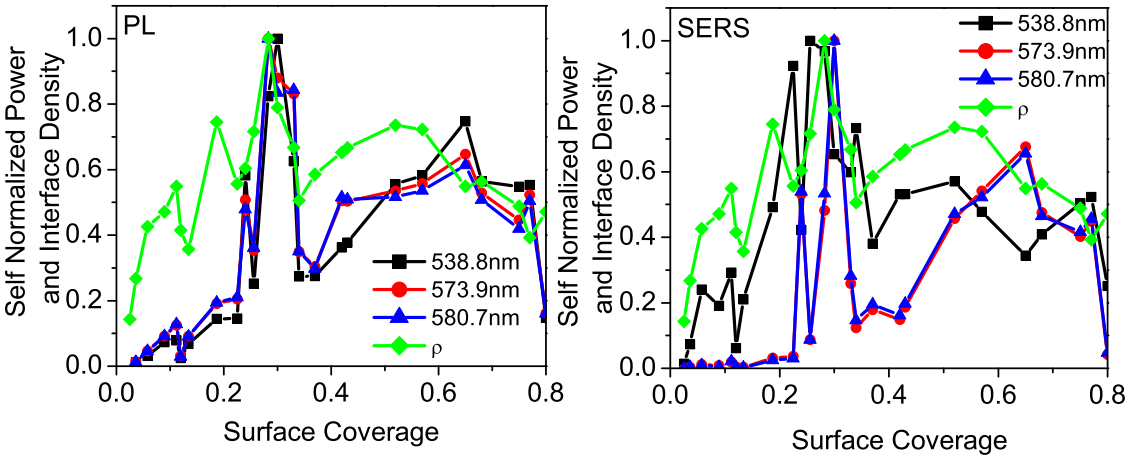

Figure 4.16. The PL and SERS power normalized to the maximum value measured at each wavelength and plotted against surface coverage. The interface density, ρ normalized to the maximum value measured in all samples is also plotted. The left panel shows the dependence for the PL and the right panel shows the dependence for SERS. We see similar behavior in the PL, SERS, and ρ across all surface coverages with a significant peak near $SC \simeq 0.3$ for all three measurements

The dependence of the PL and SERS power on ρ is non-linear as seen in Figure 4.17.. Fits to the data allow us to extract the PL and SERS to ρ scaling exponent, γ. We find that the the PL power exhibits a roughly cubic dependence on ρ while the SERS dependence is roughly quartic. The $538.8nm$ SERS signal is again the exception, showing a slightly weaker than quadratic dependence on ρ. We expect a lower scaling factor for the this peak due to the saturation behavior exhibited by its dependence on P_{ex}. Table 4.4. shows the values of the PL and

SERS to ρ scaling exponents determined for wavelengths $538.8nm$, $573.9nm$, and $580.7nm$.

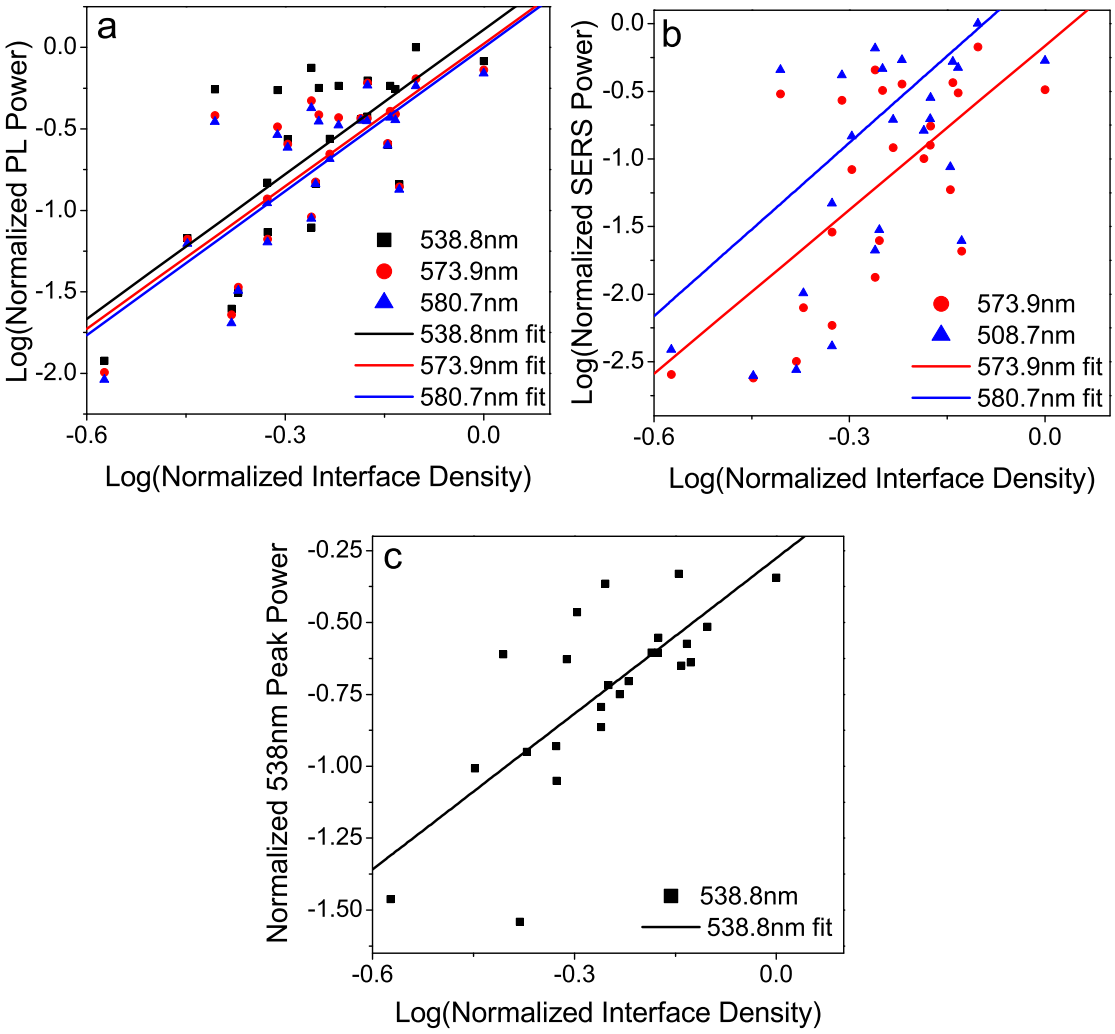

Figure 4.17. Log(Normalized PL power) and Log(Normalized SERS power) plotted against Log(ρ). Panel a is PL at wavelengths $538.8nm$, $573.9nm$ and $580.7nm$. Panel (b) is SERS power at wavelengths $573.9nm$ and $580.7nm$ and panel (c) is the $538.8nm$ peak power. The symbols are data and the solids lines are linear fits to the data.

We see significant scatter in the ρ scaling data, suggesting that ρ is not necessarily an ideal predictor of the film emission at all morphologies, despite

the similarity in their respective dependence on SC. In order to investigate the origin of this scatter we modeled the SC dependence of the emission from the films. Having measured the scaling of the PL and SERS power with ρ and with measurements of ρ at each SC in hand, we can model the dependence of the PL and SERS power on SC as $P(SC) = \beta\rho(SC)^{\gamma}$. Here γ is taken from the fits to the data for each wavelength seen in Figure 4.17.. The coefficient β is not relevant to the scaling behavior, but serves to normalize the model for comparison to the data. This model allows us to see which film morphologies contribute the scatter in the ρ scaling data in Figure 4.17., and where a model based solely on scaling with ρ breaks down. We see in Figure 4.18. that the scaling model agrees well with the measured power for $SC < 0.4$. This suggests that the scatter in the ρ scaling data comes mainly from the higher surface coverage samples with $SC > 0.4$. The model discrepancy at larger SC is greater for SERS than for PL, with the exception of the $538.8nm$ peak, which shows the least discrepancy. We attribute this result to the dependence of the EM field intensity distribution on ρ. While the density of hot spots is monotonic in ρ for $SC > 0.4$, the intensity of the hot spots is not. Prior to coalescence the average hot spot intensity increases with ρ because average gap size decreases with ρ. After coalescence the average hot spot intensity increases independent of ρ due to the continued decrease in size of the remaining gaps and voids [67, 196, 198–200]. The nonlinear excitation intensity dependence of the PL and SERS then results in greater emission power than predicted by the ρ scaling

model, as seen in Figure 4.17.. This argument is supported by the agreement between the ρ scaling model and the data for the $538nm$ SERS peak. For this signal the the scaling model does not break down at $SC > 0.4$. This is due the the weak dependence of the SERS power at this wavelength on excitation intensity, as indicated its sub-linear scaling with P_{ex} ($\alpha_{Ag-N} = 0.4 \pm 0.2$). In this case the formation of relatively high intensity hot spots does not cause the SERS signal to overshoot the scaling model prediction because the signal is insensitive to the high intensities.

Analyzing the emission and ρ data for films with $SC < 0.4$ and $SC > 0.4$ separately allows us to further examine the specific morphology dependence of the emission signals. Figure 4.19. shows these two data sets plotted separately. We see in panels (a) and (b) that there is less scatter in the $SC < 0.4$ data than in the complete data set. In addition, scaling exponents determined from this data are larger than those determined from the full data set. This is because the emission is uncorrelated with ρ for $SC > 0.40$ as seen in panels (c) and (d). This lack of correlation also explains the limited performance of the ρ scaling model for $SC > 0.4$. This behavior could arise from two effects: (i) For $SC > 0.4$ the PL and SERS signals are dominated by only a few hot spots so that changing the average hot spot density does not affect the SERS signal. (ii) The reduction in hot spot density with increased surface coverage is balanced by the increase in hot spot intensity. Further work is needed in order to illucidate the exact relations between

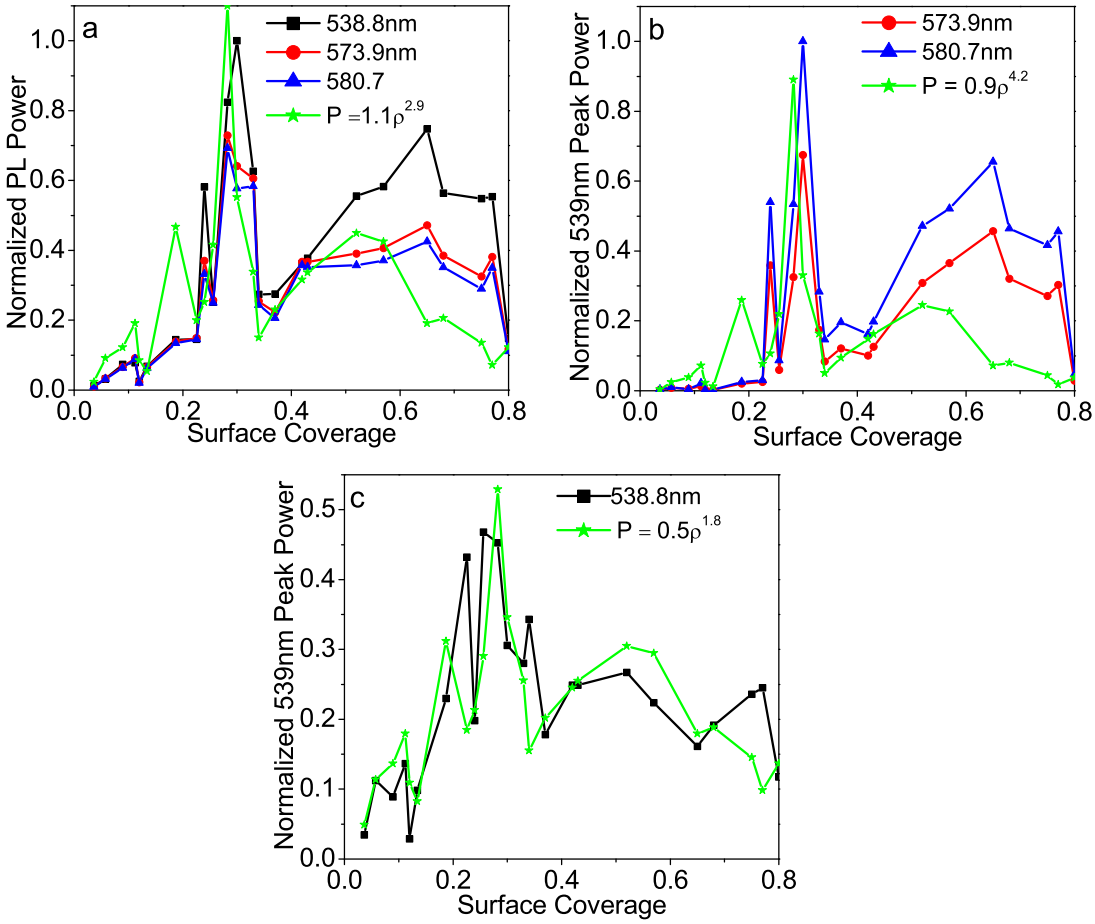

Figure 4.18. Self-normalized measured PL and SERS power plotted against SC. The green data in each panel are the emission powers calculated from measured ρ values using a scaling model. Panel (a) shows PL at wavelengths 538.8nm, 573.9nm and 580.7nm. Panel (b) shows SERS power at wavelengths 573.9nm and 580.7nm and panel (c) is for the 538.8nm SERS peak.

the density of hot spots and thier intensity across all film morphologies. Table 4.4. compares the values of the PL and SERS to ρ scaling exponents determined from the complete data set and the separated $SC < 0.4$ data.

With the scaling of the emission power with P_{ex} and ρ in hand, we can estimate how the spatially averaged EM field intensity scales with ρ. As discussed previously,

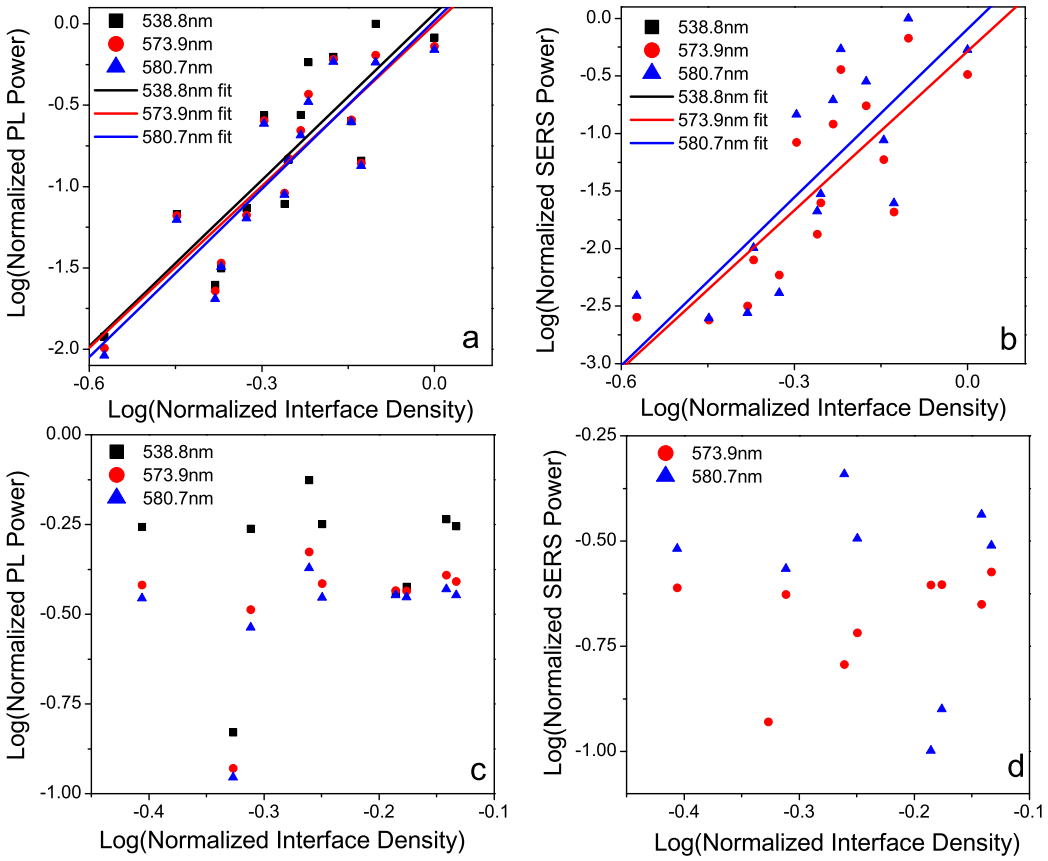

Figure 4.19. Panel (a) is Log(PL power) plotted against Log(ρ) for samples with $SC < 0.4$. Panel (b) is Log(SERS power) plotted against Log(ρ) for samples with $SC < 0.4$. The solid lines are fits to the data. Panel (c) is Log(PL power) plotted against Log(ρ) for samples with $SC > 0.4$. Panel (d) is Log(SERS power) plotted against Log(ρ) for samples with $SC > 0.4$.

Wavelength(nm)	PL to ρ scaling exponent	SERS to ρ scaling exponent
538.8	3.0 ± 0.6	1.8 ± 0.2
573.9	2.9 ± 0.6	4 ± 1
580.7	2.9 ± 0.6	4 ± 1
538.8 ($SC < 0.4$)	3.4 ± 0.6	$2.1 \pm .4$
573.9 ($SC < 0.4$)	3.3 ± 0.5	$4.6 \pm .9$
580.7 ($SC < 0.4$)	3.3 ± 0.5	5 ± 1

Table 4.4. PL to ρ and SERS to ρ scaling exponents measured at the wavelengths exhibiting SERS peaks.

the PL emission can suffer from saturation due to surface area and stoichiometric limits on the density of photoreduced nanoclusters. The $538nm$ SERS peak also exhibits saturation due to desorption of nitrogen molecules. We have used the $573.9nm$ and $580.7nm$ SERS peaks for this analysis. Given that SERS power is proportional to the EM field intensity squared, the ensemble SERS signal can be written as:

$$P_{SERS} \propto \sum_{i=1}^{N} I_i^2 \tag{IV.1}$$

Here N is the total number of molecules probed, which is surface coverage dependent, and I_i is the electric field intensity experienced by molecule i. The RMS electric field intensity is written as:

$$I_{RMS} = \sqrt{\frac{1}{N}\sum_{i=1}^{N} I_i^2} \tag{IV.2}$$

Combining equations IV.1 and IV.2 we have:

$$I_{RMS} \propto \sqrt{\frac{1}{N} P_{SERS}} \tag{IV.3}$$

The average value of the SERS to ρ scaling exponent determined from the $SC < 0.4$ data, where ρ is highly correlated with the signal, is 5 ± 1. The number of adsorbed molecules is proportional to the film surface area. The film growth simulations discussed in Chapter III indicate that the film surface area is linear in SC for $SC < 0.75$, with scaling exponent $.976 \pm 0.002$. The simulated data an fit used to determine the scaling exponent are shown in Figure 4.20.. In this case we can set $N \propto SC$ in equation IV.2. Figure also shows Log(SC) plotted against Log(ρ) and

a fit to the data. We find $SC \propto \rho^{1.6\pm0.4}$ for $SC < 0.4$. Using this data we can estimate how I_{RMS} scales with ρ:

$$I_{RMS} \propto \sqrt{\frac{P_{SERS}}{SC}} \propto \sqrt{\frac{\rho^{5\pm1}}{\rho^{1.6\pm0.4}}} = \rho^{1.8\pm0.4} \tag{IV.4}$$

We find that the RMS spatially averaged electric field intensity scaling falls between $\rho^{1.4}$ and $\rho^{2.2}$ for $SC < 0.4$. We attribute this non-linear scaling to the fact that when $SC < 0.4$, increasing ρ increases the density of nanoscale gaps and decreases the gap distance. This results in both more hot spots and larger average hot spot intensity, producing a non-linear behavior [67].

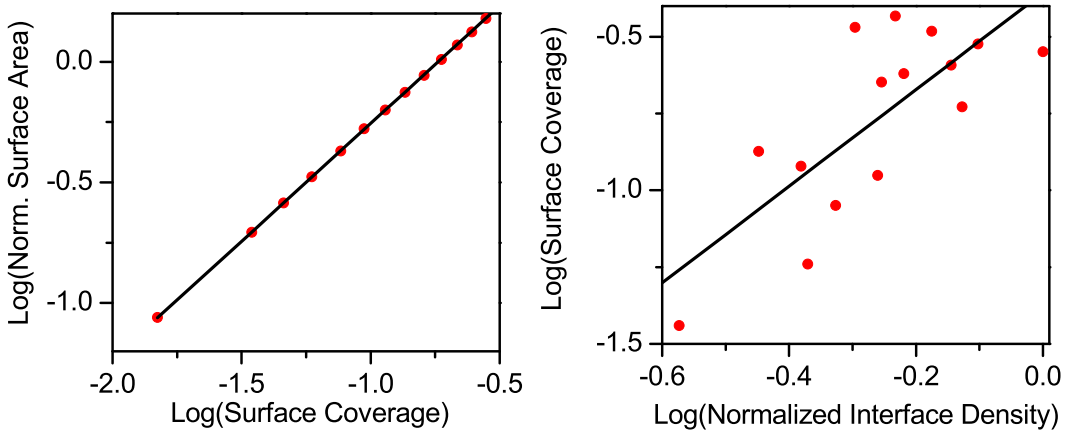

Figure 4.20. Panel (a) is simulated Log(Normalized Surface Area) plotted against Log(SC) for $SC < 0.4$. Panel (b) is Log(SC) plotted against Log(ρ) for samples with $SC < 0.4$. The solid lines are fits to the data.

Taken together, the above results point to ρ as the dominant structural feature affecting the ensemble PL and SERS power for $SC < 0.4$. The interface density determines the hot spot density and is an indicator of hot spot intensity, although the former relation is not monotonic. We can now see that control of ρ will

provide a handle for manipulating the PL and SERS power as well as the EM field enhancement. We also see that measurement of ρ may be useful in more accurately predicting these optical properties *a priori*.

Conclusions

We have shown that the ensemble PL and SERS power from silver Tollen's films is strongly correlated with the interface density in the films. Using insight provided by our previous work to understand the growth and structure of the films we have attributed this correlation to the role of the interface density in determining the spatially averaged EM field enhancement. Specifically, for $SC < 0.4$ the increased density of nanoscale gaps and reduction in gap size with increased interface density results in a non-linear dependence.

The maximization of the ensemble PL and SERS signals at $SC \simeq 0.3$ is an important result in the context of applications which use disordered nanostructured metal films for enhancement of optical processes. It has been established that the hot spot spatial and intensity distributions depend strongly on the structure of the films and that varying morphologies provide the best optical response for different applications [48, 94]. It has also been shown that films with fractal structure produce individual hot spots with the greatest local EM field intensities. Combined with the quadratic intensity dependence of SERS [49], these film geometries are known to produce huge SERS signals capable of detecting Raman scattering from

a single molecule [14, 48]. Consequently, relatively high surface coverage films showing fractal self-similarity have received the majority of attention from studies on metal films for enhancement of optical processes.

While fractal films produce individual hot spots with the greatest EM field intensity, the hot spots are highly localized [50] and their density is not necessarily maximized, which limits the spatially averaged EM field enhancement across the entire film. This type of hot spot distribution is not necessarily ideal for enhancement of ensemble optical processes across large regions of the film and/or those which have linear (or weaker) dependence on excitation light intensity. Such processes include charge carrier production in photovoltaics [203], linear PL from uniform coatings of organic dyes and quantum dots [204], and the PL of the silver films themselves [67]. We have shown that metal films near the coalescence stage may be better suited for use in these applications. This may have additional implications in large scale applications such as photovoltaics, where the reduced material requirements needed to produce the lower surface coverage coalescing films provides an additional advantage over the higher surface coverage fractal films.

The maximization of the PL and SERS signals near the onset of coalescence is an important factor in the potential use of these signals for optical bio/chemical sensing. This optical sensing potential is apparent in the high sensitivity of PL and SERS power to the interface density. In this case binding or conformational

changes of bio/chemical agents at the silver interface may induce a change to the effective interface density and gap distances. The binding agents will also change the local polarizability at the surface, which will shift the LSP resonances of the structures. The binding agents will then affect the measured PL and SERS power, *even if the the binding elements are not photoluminescent or Raman active themselves*. Near coalescence the dependence of the PL and SERS power on interface density is maximized, providing the greatest sensitivity to changes in the interface density. The PL and SERS signals are also maximized near coalescence providing the greatest integrated signal. Finally, the interface density itself is maximized near coalescence, providing the greatest opportunity for bio/chemical surface interactions to occur. This three-fold argument for the use of near-coalescence films in optical sensing applications warrants further investigation. Future directions for our work may be to investigate the use of PL from Tollen's films for bio/chemical sensing.

Additional future directions for this work will be to investigate the generality of the results. Measuring the dependence of PL, SERS, and EM field enhancement on interface density in metallic films fabricated by other methods may illuminate a universal behavior which could be used to predict optical properties in many types of films. For example, films deposited by thermal evaporation also exhibit island formation and we expect that similar coalescence behavior will result in maximized enhancement of ensemble optical processes in those films.

Methods for modification of the film structure, such as thermal annealing or photo-annealing, may allow for further maximization of the interface density. For example, thermally annealing films just prior to significant coalescence will round out sharp structures and decrease the interface density. However if this process is followed by a minimal and well controlled amount of further deposition the interface density may be enhanced above that produced by deposition alone [125]. These questions and ideas will require further study in order to determine the full potential of nanostructured metallic films for enhancement and tuning of optical processes.

This chapter concludes the detailed discussion of our efforts to understand how the optical properties of nanostructured metallic films depend on their structure and environment. In the next and final chapter we summarize our work, discuss the open questions our study has brought forth, and present possible future directions for our work which may help to answer those questions.

CHAPTER V

CONCLUSIONS

We have applied the complimentary techniques of theory, computation and experiment to study how optical properties in two types of nanoscale silver films are influenced by the structure of the films and their environment. Theoretical and experimental investigations into the influence of temperature on the surface plasmon resonance (SPR) in films with nanoscale thickness led us to develop a method for accurate measurement of fluid thermo-optic (TO) coefficient. Our SPR based method solves some of the major difficulties with measurement of fluid TO coefficients by allowing for the use of microscale fluid volumes in the measurement. The ability to accurately measure the TO coefficient in microfluidic environments is crucial to further progress in SPR based sensor development.

We have also applied the knowledge gained and the methods developed in the theoretical and experimental TO measurement work to develop an SPR based microfluid temperature sensor. The methods we developed are well suited to microfluidic applications and have potential for further miniaturization. These methods applicable to microscopic thermometry and thermal diagnostics of nanoscale systems. For example, these techniques could be used to probe the temperature of a fluid reservoir with nanoscale dimensions in contact with a metal

nanostructure. This would allow for detection of energy transfer to the structure by optical absorption. As a proof of principle we have used our setup to detect temperature changes at the interface between a microfluid and a $50nm$ thick silver film caused by excitation of surface plasmon polaritons at the interface.

Using a different setup we addressed relations between structural characteristics and light emission properties in chemically deposited silver films. We have shown that the ensemble photoluminescence (PL) and surface enhanced Raman scattering (SERS) signals seen in these nanostructured silver films can be understood in terms of their microstructure. In order to make this connection we studied the deposition and growth of nanostructured silver films chemically deposited using the Tollen's reaction. First we developed a method for characterizing film structure across a wide range of morphologies using digital image analysis of scanning electron micrographs. We then used the information gained from characterizing the film structure to develop a model for the chemical deposition of the films. We used a Monte Carlo algorithm to implement the model in numerical simulations and investigated the growth and three dimensional (3D) structure of the films. In developing and implementing the chemical deposition model we have provided another tool to researchers for studying and characterizing the growth and 3D structure of nanostructured metallic films.

We have applied the insight into film growth and structure gained from modeling and simulating the Tollen's deposition process to understand the morphology

dependence of the PL and SERS exhibited by the films. We have measured the ensemble PL and SERS signals across a wide range of film morphologies and found a non-monotonic dependence on the surface coverage in the film. We have defined the projected interface density as a structural characteristic of the films which is easily determined from SEM images. We show that the interface density measurement incorporates the structural features of the film which dominate the ensemble PL and SERS signals for surface coverages less than 0.4. We have attributed this dependence to the role of the interface density in determining the spatially averaged EM field enhancement in the films.

Together this work demonstrates the usefulness in crossing disciplines and applying complimentary theoretical, computational, and experimental techniques to solve the complex and multiscale problems present in the fields of nanoscale metallic optics and plasmonics. We hope this dissertation will provide a useful launching platform for future application of the methods we have developed to the study of pertinent questions in these fields.

Future Work

Our work has produced a number of interesting questions to be answered and problems to be solved in future work. The extension of SPR based thermometry to applications in nanoscale optical thermometry will require significant theoretical and experimental analysis. The optimal SPP coupling geometries, excitation

sources, and detection methods for a given experimental application will need to be investigated.

The Tollen's chemical deposition model has great potential for providing difficult to measure 3D structural information required for accurate prediction of optical properties in such films. Structural statistics extracted from the simulated films can be used as inputs to analytical theories while the digitized structures themselves can be used for optical simulations. This additional tool for examining the relation between structure and optical properties in nanostructured films will help us to more quickly converge on structures optimized for specific applications. Testing the full potential of this model is now a matter of running simulations, extracting needed information, entering the information into a relevant theory or simulation, and comparing the results to experiment. Doing so will tell us about both the advantages and limitations of the deposition model as well as how it might be improved and generalized. Adapting the model to describe the deposition of other materials by other methods provides an opportunity to test the general applicability of our image analysis methods in modeling film growth.

The experimental result that the maximum ensemble PL and SERS signals occurred in films at the coalescence stage of growth raises questions about which film morphologies are best suited for specific applications. The go-to answer to this question is often that fractal films are ideal for enhancing light-matter interactions. Fractal films do produce the highest hot spot intenties, however we have shown that

the largest ensemble signal enhancements occur near the coalescence stage of film growth. We understand this result in terms of the relation between interface density and spatially averaged excitation field intensity in the metal films. Specifcally, the maximization of the interface density near the coalescence stage of growth results in a maximzed average field intensity. Additional work similar to what we have done here is needed in order to determine the generality of these results. We want to know if the interface density is always a dominant factor in enhancement of ensemble optical processes in metallic films. For example, performing the same interface density and optical measurements on films fabricated by thermal evaporation, laser ablation and electrochemical deposition will begin to answer this question.

The ability to understand, predict, and thus optimize film structure for specific optical applications is a major advantage provided by the model and simulations. We found that insights provided by the modeling and simulations work were immediately helpful in understanding the general behavior of PL and SERS signals in silver Tollen's films. Understanding these experimental results in terms of specific morphological features resulting from the film growth process allowed us to envision the opportunity for exploitation of the PL and SERS signals for biochemical sensing applications. A theoretical investigation to answer questions about the feasibility, sensitivity, and fundamental limitations of such sensors is a logical next step, with sensor implementation and experimental studies to follow. The film deposition model and simulation methods we have developed might again

prove useful in the context of the biochemical sensor study. For example, one could simulate the film structure as well as deposition of biochemical agents onto the film. Sensor parameters such as adsorbed agent concentration could then be estimated and used to predict the resulting PL and SERS signal changes.

Closing Remarks

I found the combined application of modeling, computation, and experiment to our study to be a very satistfying process. I believe the whole scientific processes is greater than the sum of these individual disciplines and that omni-directional feedback between these techniques provides for the rapid pace of scientific discovery we currently experience as a society. The formation of a collaborative environment which encourages interaction between experts in theory, computation, and experiment may be one of the most important progressions of modern science and I feel privileged to be a part of that process.

The time and effort required for an individual student to explore and contribute to each of the disciplines of modeling/theory, computation, and experiment are relatively large. However, I believe the payoffs to the student in the form greater experience, intuition, and vision are worth the time and effort. I would like to express my appreciation to my advisor Miriam for allowing me to explore while watching to make sure I did not get lost. While my path may have been lengthened

by taking an exploratory route, I believe my growth as a scientist was increased as well.

APPENDIX A

TOLLEN'S FILM DEPOSITION SIMULATION CODE

The Tollen's Film Deposition Simulation program discussed in Chapter III was written in the interpreted MATLAB language. This appendix shows the main deposition simulation code as well as code from subsidiary functions called on to calculate structural properties of the simulated films. Code from the built-in MATLAB functions that are called is not shown.

```
function[topo,results] = FilmSim3D_060811(imsize,thirdd, SCend, stepsize,
initglassprob, initsilverprob, deplrate)

%simulates chemical deposited of a silver film by Tollen's method

%inputs are size of simulation space, surface coverage to simulate, surface
%coverage step size for measuring film properties and model parameters
%outputs are a 3D boolean array representing the film and the results of
%film properties calculated every "stepsize" in SC.
%%%%%%%%%%%%%%%%%%%%%%%%%%%%%%%%%%%%%%%%%%%%%%%%%%%%%%%%%%%%%%%%%%%%%%%%%%%
%INPUT:
%imsize--length of one side of the square substrate area (area of the simulation
space) in pixels
%thirdd--hieght of the simulation space
%SCend--end the simulation when this surface coverage value is reached
%stepsize--surface coverage step size between measurement and recording of
    %film properties
%initglassprob--initial value for the glass binding probability-this is G
    %in the deposition model
%initsilverprob--initial value for the silver binding probability-this is S
    %in the deposition model
%deplrate--decay constant describing the depletion of silver particle
    %concentrations-this is gamma in the deposition model

%%%%%%%%%%%%%%%%%%%%%%%%%%%%%%%%%%%%%%%%%%%%%%%%%%%%%%%%%%%%%%%%%%%%%%%%%%%
%OUTPUT
%Topo-3D boolean array where 1's representing deposited silver.
%results(:,1)-deposition time (minutes)
%results(:,2)-surface coverage
%results(:,3)-volume filling fraction
%results(:,4)-number of islands
%results(:,5)-max film thickness (nm)
%results(:,6)-average island area (nm^2)
%results(:,7)-standard deviation in island area (nm^2)
%results(:,8)-average effective island diameter (nm)
%results(:,9)-standard deviation in effective island diameter (nm)
%results(:,10)-average island (gyration radius)^2 (nm^2)
%results(:,11)-average island gyration radius (nm)
%results(:,12)-RMS island Rg (nm)
%results(:,13)-Empty legacy column
%results(:,14)-Empty legacy column
%results(:,15)-Empty legacy column
%results(:,16)-Empty legacy column
%results(:,17)-Rg to area scaling parameter (slope of linear fit to Log(Rg) vs. Log
(A))
%results(:,18)-intercept of linear fit to Log(Rg) vs. Log(A)(for use in plotting
only)
%results(:,19)-standard deviation in Rg (nm)
%results(:,20)-average film thickness (nm)
%results(:,21)-RMS film roughness (nm)
%results(:,22)-difference in RMS roughness betwen substrate and free sides of the
film (nm)
%results(:,23)-mass (pixels)
%results(:,24)-surface area per unit substrate area
%results(:,25)-average island height (pixels)
%results(:,26)-average island diameter (pixles)
```

```
%results(:,27)-total island perimeter (pixels)
%results(:,28)-average film thickness measured by AFM probe (nm)
%results(:,29)-average RMS roughness measured by AFM probe (nm)
%%%%%%%%%%%%%%%%%%%%%%%%%%%%%%%%%%%%%%%%%%%%%%%%%%%%%%%%%%%%%%%%%%%%%%%%%%%%%%%
%%%%%%%%%%%%%%%%%%%%%%%%%%%%%%%%%%%%%%%%%%%%%%%%%%%%%%%%%%%%%%%%%%%%%%%%%%%%%%%
%begin simulation code
%calculte number of steps to get to desired surface coverage
steps = ceil(SCend/stepsize);
%initialize outputs
results = zeros(steps,29);
%generate blank simulation space
topo = ~true(imsize,imsize,thirdd);
temptopo = ~true(imsize,imsize,thirdd);
%DR = zeros(steps,6);
%define simulation scale in nm/pixel
scale =24;
%initialize SC measurement and mass measurement
SC = 0;
mass = 0;
finaltime =1200;%define maximim time (iterations) to run simulation
%initialize time index and results index
resultsindex = 1;
timeindex =0;
%initialize binding probs
glassprob = initglassprob;
silverprob = initsilverprob;
%build film
while  SC < SCend && timeindex < finaltime
    %generate matrix of random numbers from 0 to 1
    parts = rand(imsize-2, imsize-2, thirdd-2);
    parts = padarray(parts, [1,1,1]);
    %get indices for the particle probabilities
    [row,col]=find(parts);
      for i =1:size(row);
          x = row(i);
          y = mod(col(i),imsize);
          z = ceil(col(i)/imsize);
          bindnum = parts(x,y,z);
          sumneighbors = 0;
          %dont bother with locations that already have particles placed
            if topo(x,y,z)==0 && z~=1
                %determine if any neighbors are silver
                % the model assumes neighbors must share a face, not just
                % an edge or a corner, so these contributions have been commented
                % out below
                    %m = topo(x+1,y+1,z);%forward right
                    %n = topo(x-1,y+1,z);%%forward left
                    %o = topo(x,y+1,z+1);%forward up
                    %p = topo(x,y+1,z-1);%forward down
                    %q = topo(x+1,y-1,z);%back right
                    %r = topo(x-1,y-1,z);%back left
                    %s = topo(x,y-1,z+1);%back up
                    %t = topo(x,y-1,z-1);%back down
                    %u = topo(x+1,y,z-1);%right down
                    %v = topo(x+1,y,z+1);%right up
                    %w = topo(x-1,y,z-1);%left down
```

```
108                     %g = topo(x-1,y,z+1);%left up
109                     %a = topo(x+1,y+1,z+1);%right forward up
110                     %h = topo(x-1,y+1,z+1); %left forward up
111                     %k = topo(x+1,y-1,z+1); %right, back up
112                     %aa = topo(x-1,y-1,z+1);%left back up
113                     %bb = topo(x+1,y+1,z-1);%right forward down
114                     %cc = topo(x-1,y+1,z-1); %left forward down
115                     %dd = topo(x+1,y-1,z-1); %right, back down
116                     %ee = topo(x-1,y-1,z-1);%left back down
117                     b = topo(x-1,y,z);%left
118                     c = topo(x+1,y,z);%right
119                     d = topo(x,y+1,z);%forward
120                     e = topo(x,y-1,z);%back
121                     f = topo(x,y,z-1);%down
122                     if z == 2
123                         f = 0;
124                     end
125                     l = topo(x,y,z+1);%up
126                     sumneighbors = (b+c+d+e+f+l);%+(m+n+o+p+q+r+s+t+u+v+w+g)+↙
(a+h+k+aa+bb+cc+dd+ee);
127
128             end
129             if  bindnum~=0 && sumneighbors >0 && bindnum < silverprob*sumneighbors;%%↙
test to see if particle should be bound
130                     temptopo(x,y,z)=1;%same
131             end
132             %now test for if the particle might bind to the substrate
133             if z == 2 && temptopo(x,y,z)==0 && bindnum~=0 && bindnum <= glassprob
134                     temptopo(x,y,z)=1;%same
135             end
136       end
137       topo = topo+temptopo;%add the particles deposited in this iteration to the↙
topography
138       topo = topo >=1;%force boolean addition
139       timeindex = timeindex+1%increment the timekeeping index
140
141       proj = proj2d(topo(2:end-1,2:end-1,:));%get the projection of the film
142       SCtemp = surfcovbw(proj);%measure the surface coverage
143
144       %if the stepsize has been met measure film properties
145         if SCtemp >= (SC + stepsize)||timeindex == finaltime
146             SC=SCtemp%print SC
147             mass = sum(sum(sum(topo(2:end-1,2:end-1,:))))/(imsize-2)^2;%compute total↙
mass per unit area
148             results(resultsindex,2) = SC;%keep SC data point
149             results(resultsindex,1) = timeindex;%keep track of depo time
150             [have,hmax,rough,drough] = aveh2(topo(2:end-1,2:end-1,:),imsize-2);%↙
measure average and max height
151             [haveprobe,proberough] = aveh_probe(scale,topo(2:end-1,2:end-1,:),imsize-↙
2,hmax);%determine average height and roughness meaured by AFM probe
152
153             ff = sum(sum(sum(topo(2:end-1,2:end-1,:))))/((imsize-2)^2*hmax);%compute↙
filling fraction using a volume defined by max height
154             %load results into output variable
155             results(resultsindex,28) = haveprobe;
156             results(resultsindex,29) = proberough;
```

```
157             results(resultsindex,3) =ff;
158             results(resultsindex,20) = have*scale;
159             results(resultsindex,21) = rough*scale;
160             results(resultsindex,22) =drough*scale;
161             results(resultsindex,5)= hmax*scale;
162             results(resultsindex,23) = mass;
163
164             %calculate properties of projection
165             [imlabeled,numObjects] = bwlabel(proj,4);%label particles
166             results(resultsindex,4)= numObjects;%track number of objects
167             partdata = regionprops(imlabeled,'Area','Centroid','PixelList');%↙
calculate particle data
168             [psize,parea] = partsize(partdata,numObjects);%get particle areas and↙
sizes
169             results(resultsindex,6) = scale^2*sum(psize)/numObjects;%calculate↙
average area
170             results(resultsindex,7) = scale^2*std(psize);%calculate std area
171             partd = scale*2*sqrt(psize/pi);%calculate effective island diamters in nm
172             results(resultsindex,8) = sum(partd)/numObjects; %average effective↙
island diameters
173             %compute standard deviation in island diameters
174             results(resultsindex,9) = std(partd);
175             [gradii,gareas] = gyration2(partdata,numObjects,psize);%calculate list of↙
island Rg and Rg^2
176             results(resultsindex,10) = scale^2*sum(gradii(1,1:end))/numObjects;%↙
calculate average island Rg^2
177             results(resultsindex,11) = scale*sum(gradii(2,1:end))/numObjects;%↙
calculate average island Rg
178             results(resultsindex,19) = std(scale*gradii(2,1:end));%calculate std Rg
179             results(resultsindex,12) = scale*sqrt(sum(gradii(1,1:end)))/numObjects;%↙
calculate rms island Rg
180
181             %fit log(Rg) vs. log(Area) to get scaling behavior
182             if numObjects >1
183                 [results(resultsindex,17), results(resultsindex,18)] = loglogfit↙
(gareas,gradii(2,1:end),0);%calculate exponent in log-log fit of Rg. vs. Area
184             end
185             if numObjects ==1% if there is only one island, keep the previous value↙
for the exponent
186                 results(resultsindex,17) = results(resultsindex-1,17);
187                 results(resultsindex,18) = results(resultsindex-1,18);
188             end
189
190             %measure silver surface area by measuring number of exposed
191             %faces
192             [row,col]=find(topo);%find silver locations
193             surfacearea = 0;
194             %run through silver locations
195             for i =1:size(row);
196                 x = row(i);
197                 y = mod(col(i),imsize);
198                 z = ceil(col(i)/imsize);
199
200                 %find neighbor locations not filled with silver
201                     if x ~=1 && x ~=imsize && y ~=1 && y ~=imsize && z ~=1 && z↙
~=thirdd
```

```
202                         b = topo(x-1,y,z);%left
203                         c = topo(x+1,y,z);%right
204                         d = topo(x,y+1,z);%forward
205                         e = topo(x,y-1,z);%back
206                         f = topo(x,y,z-1);%down
207                         if z == 2
208                         f = 0;
209                         end
210                         l = topo(x,y,z+1);%up
211
212                     end
213
214                 sumsurface = (b+c+d+e+f+l);%add up local surface area
215                 surfacearea = surfacearea + (6-sumsurface);%add to total surface area
216             end
217             results(resultsindex,24)=surfacearea/(imsize-2)^2;%record surface area↙
per substrate area
218
219             %calculate average aspect ratios of islands
220             [topolabel,numIslands] = bwlabeln(topo(2:end-1,2:end-1,:),6);%label↙
islands in 3D
221             %initialize outputs
222             avalue = zeros(1,numIslands);
223             bvalue = zeros(1,numIslands);
224
225             %loop through labeled islands
226             for i = 1:numIslands
227                 [labelrow,labelcol]= find(topolabel==i);
228                 islanda = ceil(max(labelcol)/imsize);%get max height of island
229                %convert to boolean 3D island
230                 topobool = topolabel > 0;
231                 projIsland = proj2d(topobool);% get island projection
232                 areaIsland  = sum(sum(projIsland));%get area of projection
233                 islandb = sqrt(areaIsland/pi);%get effective diameter of island
234                 avalue(1,i) = islanda;%island height
235                 bvalue(1,i) = islandb;%island effective radius
236             end
237             %average results
238             avalueave = sum(avalue)/numIslands;
239             bvalueave = sum(bvalue)/numIslands;
240             %load to output
241             results(resultsindex,25)=avalueave;
242             results(resultsindex,26)=bvalueave;
243
244
245             sumperim = perimexact(proj); %get the projected disland perimeter
246             results(resultsindex,27)= sumperim/((imsize-2)^2);%normalize to substrate↙
area
247
248             resultsindex = resultsindex + 1;%increment the index of the results array
249         end
250           %account for depletion assuming exponential decay in concentration
251         silverprob = initsilverprob*exp(-deplrate*timeindex);
252         glassprob = initglassprob*exp(-deplrate*timeindex);
253 end
254
```

```
function[SC] = surfcovbw(A)
%determine the fraction of pixels in a BW or boolean image that do not have value 0

%INPUT:
%A-image to analyze

%OUTPUT
%SC-fraction of non-zero valued pixels

%%%%%%%%%%%%%%%%%%%%%%%%%%%%%%%%%%%%%%%%%%%%%%%%%%%%%%%%%%%%%%%%%%%%%%%%%%%%%%%
%%%%%%%%%%%%%%%%%%%%%%%%%%%%%%%%%%%%%%%%%%%%%%%%%%%%%%%%%%%%%%%%%%%%%%%%%%%%%%%
[imsizex,imsizey] = size(A);%determine the size of the image
fill = A > 0;%find pixels that are not zero-valued
sumfill = sum(sum(fill));%add up non zero-valued pixels
SC = sumfill/(imsizex*imsizey);%normalize to image size
```

```
function[have,maxh,rough,drough] = aveh2(topo,imsize)
%caluculates the RMS roughness and average value of a the z-pixels in a
%boolean array with dimensions x,y,z

%INPUT:
%topo-3D boolean array with equal x and y dimensions
%imsize size of x and y dimension

%OUTPUT:
%have-average of maximum z-value at each x,y location
%maxh-max z-value in the array
%rough-RMS roughness of max z-values
%drough-RMS roughness of min z-values

[row,col]= find(topo);% find indices of locations with non-zero
maxh = ceil(max(col)/imsize);%determine max non-zero z height
%initialize surfaces arrays
maxz=zeros(imsize,imsize);%top surface
minz=zeros(imsize,imsize);%bottom surface
%loop through (x, y) locations
for i =1:length(row)
          x = row(i);
          y = mod(col(i),imsize);
          if y ==0
              y=imsize;
          end
          tempmax = find(topo(x,y,1:end), 1, 'last' ); %find the max non-zero z height at each location
          tempmin = find(topo(x,y,1:end), 1, 'first' ); %find the minimum non-zero z height at each location
          %account for bottom pixels never having any non-zero pixels (this is the substrate)
          if sum(topo(x,y,1:end)) ==0
              tempmax = 1;
              tempmin = 1;
          end
          maxz(x,y) = tempmax-1; %account for first pixel being substrate
          minz(x,y) = tempmin-1; %account for first pixel being substrate
end
have = sum(sum(maxz))/(imsize)^2;%cacluate average of max z-values including regions with no non-zero pixels in the average
minave = sum(sum(minz))/(imsize)^2;%cacluate average of min z-values including regions with no non-zero pixels in the average
%initialize RMS roughness variables
sumdiff = 0;
sumdiffmin = 0;
%loop through (x,y) locations in surfaces
for i=1:imsize
    for j=1:imsize
        %calculate square of the difference from the mean
        sumdiff = sumdiff+(maxz(i,j)-have)^2;
        sumdiffmin =sumdiffmin+(maxz(i,j)-minave)^2;
    end
end
rough=sqrt(sumdiff)/(imsize);%sum squares and normalize
drough = rough - sqrt(sumdiffmin)/(imsize);%sum squares and normalize
```

```
function[haveprobe,proberough, probetopo] = aveh_probe(scale,topo,imsize, hmax)
%simulate an AFM measurement on a rough film assuming a specific tip goemetry

%INPUTS:
%scale-simulation scale (nm/pixel)
%topo-3D boolean array representing the film
%imsize-size of x and y dimensions of the boolean array
%max non-zero z-index in the 3D array

%OUTPUT:
%haveprobe-average thicnkess measured by AFM tip
%proberough-RMS roughness measured by AFM tip
%probetopo-topography measured by AFM tip

%%%%%%%%%%%%%%%%%%%%%%%%%%%%%%%%%%%%%%%%%%%%%%%%%%%%%%%%%%%%%%%%%%%%%%%%%%%%%%%
%%%%%%%%%%%%%%%%%%%%%%%%%%%%%%%%%%%%%%%%%%%%%%%%%%%%%%%%%%%%%%%%%%%%%%%%%%%%%%%
probetopo = zeros(imsize-2,imsize-2);%initialize topo as measured by probe
%define tip geometry variables
Rnm = 10;%tip curvature
R = Rnm/scale;%tip curvature in (nm)
theta = 35;%tip angle
thetarad = theta*pi/180;%convert to radians
w0 = R/sqrt(1+(tan(thetarad))^2);%width of tip where curvature departs from↙
extrapolated tip angle
d0 = R-w0*tan(thetarad);%difference between actual tip and depth formed by↙
extrapolating tip angle

%determine if max film height is greater than d0 and assign max width to
%test accordingly

if hmax < d0
   wmax = sqrt(R^2-(R^2-hmax^2));
end
%(tip can probe full film depth at every location)

if hmax >= d0
   wmax = (hmax-d0)*tan(thetarad)+w0;
end
%(tip cannot probe full film depth at every location, the max distance that
%from the tip that will need to be tested is wmax)


%max points away to test in any direction
deltamax = ceil(sqrt(2)*wmax);

%loop through substrate area
for i =2:imsize-1
    for j =2:imsize-1
        probehmax = 0;%initialize probe depth
        %define silver height at probe location
        centerh = find(topo(i,j,1:end), 1, 'last' );
        if sum(topo(i,j,1:end)) ==0
           centerh = 1;%account for substrate pixel
        end
        %loop through points within deltamax
        for k = -deltamax:deltamax
```

```
55              for l = -deltamax:+deltamax
56                  x = i+k;
57                  y = j+l;
58
59                  %test to see if location is in simspace
60                  if  x > 0 && y > 0 && x < imsize && y < imsize
61
62                      w = sqrt(k^2 +l^2);%define distance from tip
63
64                      %define tip depth at this distance
65                      %based on region of tip and tip geometry
66                      if w < w0
67                          d = R - sqrt(R^2-w^2);
68                      end
69                      if w >=w0
70                          d = (w-w0)/tan(thetarad) + d0;
71                      end
72
73                      %find the silver height at this nearby location
74                      h = find(topo(x,y,1:end), 1, 'last' );
75                      if sum(topo(x,y,1:end)) ==0
76                      h = 1;
77                      end
78
79                      %define probe measured height, subtracting 1 for substrate
80                      %index
81
82                      if h-centerh > d
83                          probeh = h-d-1;
84                      end
85                      if h-centerh <=d
86                          probeh = centerh - 1;
87                      end
88                      %keep track of max probe height constraing for this point
89                      if probeh > probehmax
90                          probehmax = probeh;
91                      end
92
93                  end
94              end
95          end
96          %define the minimum height possibly registered by the tip at this
97          %point
98          probetopo(i,j)= probehmax;
99      end
100 end
101
102 %calculate average thickness
103 haveprobe = sum(sum(probetopo))/(imsize-2)^2;
104
105 %caculate RMSroughenss
106 sumdiff = 0;
107 %loop through (x,y) locations
108 for i=2:imsize-1
109     for j=2:imsize-1
110         %calculte square of the difference from the mean
```

```
111         sumdiff = sumdiff+(probetopo(i,j)-haveprobe)^2;
112     end
113 end
114 proberough=sqrt(sumdiff)/(imsize-2)*scale;%normalize to image size
115 haveprobe = haveprobe*scale;%normalize to image size
116
117
118
```

```
function[psize,parea] = partsize(partdata,numObjects)
%gather pixel areas from structure containing object properties

%INPUT:
%partdata-stucture containing object properties
%numObjects-number of objects

%OUTPUT:
%psize-list of object areas
%parea-total area of all objects

%intialize list of object areas
psize = zeros(1,numObjects);
%run through number of objects and record areas
 for i = 1:numObjects;
     psize(i) = partdata(i).Area;
 end
 parea = sum(psize(1:end));%sum of total area of all objects
```

```
function[gyrationradii, gareas] = gyration2(partdata,numObjects,psize)
%calculate gyration radii (Rg) of a list of objects

%INPUTS:
%partdata-structur contatining object data
%numobjects-number of objects
%psize-list of object areas

%OUTPUT:
%gyrationradii(:,1)-list of Rg^2
%gyrationradii(:,2)-list of Rg

%gareas2-list of object areas (for use in scaling analysis)

%initialize output arrays
gareas = zeros(2,numObjects);%list of object areas (for use in scaling analysis)
gyrationradii = zeros(2,numObjects);%list of object gyration radii
%loop through objects
 for i = 1:numObjects
     radiisum = 0;%initialize sum
     centlocs = partdata(i).Centroid;%get location of centroid for island i
     %redefine indices for centroid for convenience
     locx = centlocs(1);
     locy = centlocs(2);
     pixellocs = partdata(i).PixelList;%get matrix of pixel locations for island i
     pixelnumber = length(pixellocs(1:end,1));%number of  pixels in object
     %test pixel number to avoid Rg = 0 for 1 pixel objects
     if pixelnumber > 1
         %calculate gyration radii
        for j=1:pixelnumber
            d2 = (pixellocs(j,1)-locx)^2 + (pixellocs(j,2)-locy)^2;% calculated↙
sqaured distance between particle and centriod
            radiisum = radiisum + d2; %add this distance to the radii sum
        end
        gyrationradii(1,i) = radiisum/pixelnumber; %finish calculation of  Rg^2
        gyrationradii(2,i) = sqrt(radiisum/pixelnumber); %finish calculation of↙
calculate Rg
        gareas(1,i)= psize(i);%redefine areas list
     end
     %if pixelnumber is 1 then assign the Rg of a square of unit 1 area
     if pixelnumber ==1
         gyrationradii(1,i) = 1/6; %calculate  Rg^2
         gyrationradii(2,i) = sqrt(1/6); %calculate Rg
         gareas(1,i)= 1;%redefine areas list
     end
 end

 %Legacy code for dealing with Rg = 0 that occurs for single pixel objects
 %nonzero = find(gyrationradii(1,1:end) > 0);
 %gyrationradii2 = zeros(2,length(nonzero));
 %gareas2 = zeros(1,length(nonzero));
 %for i = 1:length(nonzero)
     %gyrationradii2(1,i) = gyrationradii(1,nonzero(i));
     %gyrationradii2(2,i) = gyrationradii(2,nonzero(i));
     %gareas2(1,i) = gareas(1,nonzero(i));
 %end
```

```
function[sumperim] = perimexact(BWimage)
%determine the perimeter of the objects in a 2D boolean image (number of
%interfacial pixel faces)

%INPUT:
%BWimage-2D boolean array

%OUTPUT:
%sumperim-total perimeter of the objects in the image

%initialize perimter sum
sumperim = 0;
%get image size
[X,Y] = size(BWimage);
%loop through pixels in the image
 for i = 2:X-1
     for j = 2:Y-1
         %for those pixels which are filled (1's) count number of faces
         %contacting filled pixels
         if BWimage(i,j) ==1
            a = BWimage(i+1,j);
            b = BWimage(i-1,j);
            c = BWimage(i,j+1);
            d = BWimage(i,j-1);
            %these would count in 8-connected definition, but have been
            %commented out here
            %e = BWimage(i+1,j+1);
            %f = BWimage(i-1,j-1);
            %g = BWimage(i-1,j+1);
            %h = BWimage(i+1,j-1);

            %sum up faced contacting filled neighbors
            pixelperim =  a+b+c+d;%+e+f+g+h;

            %calculate faces contacting unfilled neighbors and add to
            %perimeter sum
            sumperim = sumperim + 4-pixelperim ;
         end
     end
 end
```

APPENDIX B

QUANTITATIVE CHARACTERIZATION OF MOUSE SEARCH PATHS IN THE MORRIS WATER MAZE

Introduction

While neuroscience researchers have been productive in their attempts to understand and describe the processes that lead to successful communication between neurons in the brain, it remains a challenge to accurately relate such findings to the deficits in cognitive function that define many devastating neurological disorders. The mechanisms behind proper function in the brain are extremely complex with cooperative behavior, feedback systems, and plasticity at many levels all working in concert to generate typical behavior. Due to these complexities, a comprehensive picture of how disorders arise must include interactions from the biochemical scale to the scale of complex outward behavior. Indeed, our ability to provide treatments for many neurological disorders critically relies on our capacity to employ multi-scale approaches that accurately determine how specific, genetically controlled biochemical changes localized in time and space impact downstream complex behavior that is altered in disease states. While we are now able to induce fine scale genetic manipulations and quantify their downstream

impacts at many relevant sublevels in model organisms, we are significantly limited in our ability to accurately detect and compare impacts on many forms of complex behavior. This hinders efforts to build a comprehensive examination of gene-disease interactions. We have worked to address this notable gap by using quantitative digital image analysis methods, commonly employed in characterizing physical structures, to analyze patterns in complex animal behavior.

Excitatory synapses support the majority of communication between neurons in the brain and the genes involved in their formation and specification have been implicated in neurological disorders ranging from Autism to Schizophrenia [205–210]. The Washbourne lab at the University of Oregon is working to link the molecular mechanisms of synapse specification to behaviors often affected in these relevant diseases. In particular, Neuroligin1 (Nlg1) is a gene that has been linked to both Autism and the process of synapse specification [209, 211, 212]. Moreover, it has been previously demonstrated that course disruption of Nlg1 function in mice can affect learning and memory behaviors, which are cognitive functions that are adversely affected within the spectrum of Autism disorders [213]. Therefore, we are testing the hypothesis that Nlg1 plays a significant role in regulating appropriate synaptic specification during critical periods for the development of explicit forms of memory. Critical periods occur when a specific neural system is most susceptible to sensory inputs and experiences that will define its form and function throughout life [214–220]. Understanding whether Nlg1

differentially influences the development of memory systems during a specific time window is required to understand how the Nlg1 gene ultimately impacts complex behavior. From this understanding we might learn how and when deficits in such performance could potentially best be addressed. To answer these important questions, the Washbourne lab generated a genetically engineered line of mice in which a mutant form of Nlg1 can be conditionally expressed during distinct periods in development within targeted regions of the forebrain [221]. Expression of the mutant form of Nlg1 interferes with the functioning of normal Nlg1 in the forebrain region. The effect of Nlg1 disruption during the juvenile stage on learning and memory in adulthood has been studied by our collaborators in the Washbourne Lab. The biochemistry within genetically modified animals has been linked to successive downstream morphological changes and finally to behavioral performance, epitomizing a multi-scale approach to neurobiological research. This was accomplished by combining the results of the following studies performed in the Washbourne Lab at four relevant biological scales: (1) Measurement of the molecular composition of excitatory synapses. (2) Measurement of the spatial distribution of characteristic synaptic proteins [222]. (3) High resolution electrophysiological mapping [223, 224]. (4) Evaluation of complex outward behavior in standard learning-memory tests [225–228]. A complete description of this work is found in reference [229]. Studies (1-3) have indicated that interference with Nlg1 disrupts synapse maturation. Synaptic concentration of the signaling

protein NR2A increases with synapse maturation, while the concentration of NR2B is relatively larger in immature synapses, and the concentration of each can be used as a method for quantifying synapse maturity [229]. As a part of study (4), social behavior of mutant and control mice was assayed. The mutant mice, which showed diminished synapse maturity relative to controls, were found to exhibit immature social behavior. We hypothesized that diminished synapse maturity in adulthood caused by interference with Nlg1 in the juvenile state, and quantified by NR2B concentration, would result in adult stage learning and memory behavior more typical of juvenile mice. Here we will describe our collaborative work to quantify mouse behavior in the Morris Water Maze memory test and determine a relation between behavior and synapse maturity as a part of study (4).

The Morris Water Maze as a Learning and Memory Test

The Morris water maze is considered the gold standard of behavioral tasks to assay explicit forms of learning and memory. Two standard aspects of performance on the Morris water maze task represent learning and memory ability: (A) how long an animal persists in a large area that formerly contained an escape route (the target quadrant) and (B) how quickly they first reach the former location of the escape route. This test is conducted after a protracted period of training in which the animal may escape from a large pool of opaque water only by finding a barely submerged platform. The animals are trained to utilize spatial cues in order to

most efficiently find this platform, and control measures are taken to ensure that spatial strategies are primarily employed by the animal [227]. Figure B.1 shows a diagram of the general Morris water maze setup along with example recorded search tracks [230]. When an animal spends less time in the target quadrant during the probe trial and takes longer to reach the target location than the control animals, a learning and memory deficit is inferred. The animals are also run through a period of reversal training which tests their ability to learn a new platform location after having already demonstrated learning a previous location.

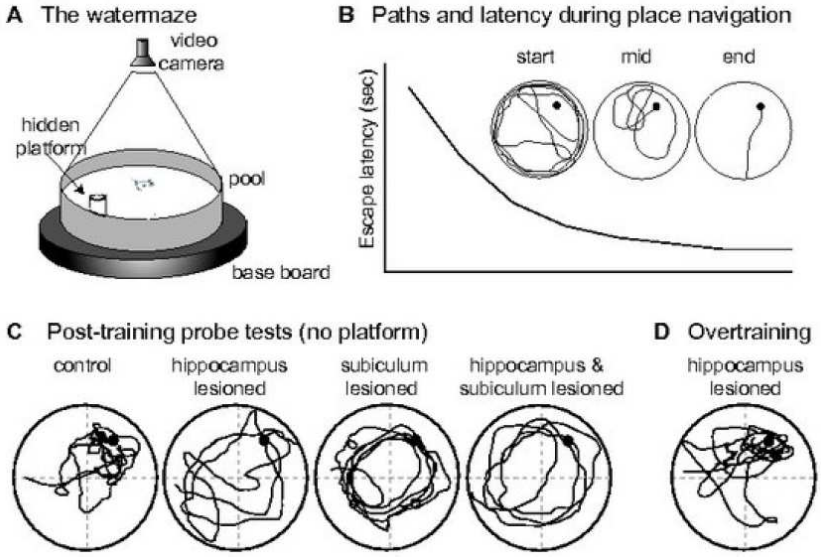

Figure B.1 The Morris water maze is an opaque pool of water from which the animal is highly motivated to escape via a submerged platform. B) Depicts the average time to locate the platform (black dot) as a function of trial period in typical animals. Typical paths taken by the animals throughout training are shown above the learning curve. C) Typical performance during probe trials reflecting the performance of mice under different treatments that adversely affect the circuitry necessary for learning and memory. D) A test condition indicating that with more intense training other circuitry can compensate. Figure adapted from reference [230].

The current state of the art with respect to analyzing Morris water maze performance is a qualitative assessment of an animals' search path as performed by an experienced human observer. Based on the observer's experiences, a search path, is classed into one of five possible patterns based on thier similarity to those seen in panels (c) and (d) of Figure B.1 [230]. The frequency at which the animals are observed to be engaged in one of the five states is then compared between test groups. This approach is highly subjective and rejects potentially significant data that may fall into ambiguous categories. Furthermore, a change in the search strategy that occurs without gross change in the two primary measures of performance, (A) and (B), is not interpreted as a change in learning and memory processes *per se*.

As new technologies arise that allow for finer manipulations of the brain and how it functions, more subtle changes in these behaviors have begun to emerge. For example we have found that behavior before reaching the target location is similar between mutants and controls, however after crossing over the former platform location their behaviors diverge. Figure B.2 shows representative probe trial tracks for control and mutant animals, demonstrating the difference in search behavior. This behavioral divergence leads to contradictory interpretation of the presence of a learning and memory deficit disorder between the two standard measures (A) and (B). These changes cannot be appropriately quantified with existing course grained, qualitative approaches such as those in Figure 1 [227, 230, 231]. These

shortcomings preclude a clear understanding of how behavioral performance is affected by Nlg1 disruption and more information is needed to accurately describe the effects of our genetic mutation and determine during what stages of life Nlg1 is most influential in producing proper cognitive development. A major contributor to these shortcomings is the inability to accurately distill the complex data set that is produced when an animal searches for a target into a tractable number of accurate and animal-centric metrics that can be compared between groups.

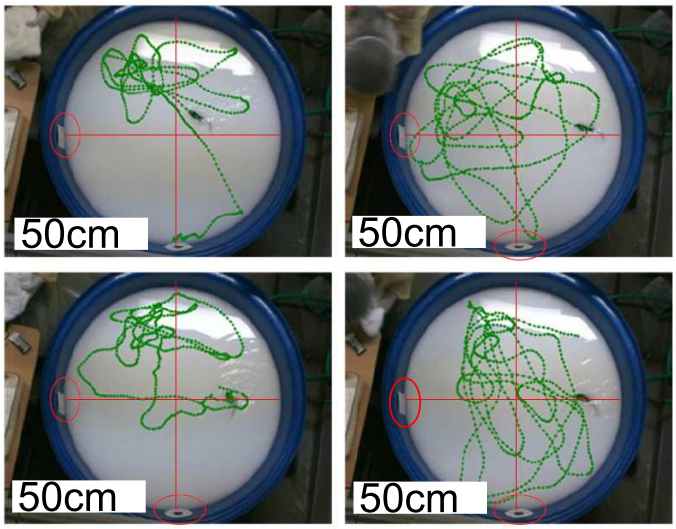

Figure B.2 Representative Morris water maze probe trial tracks for four separate control (left) and test (right) animals measured in the Washbourne lab. All animals had been trained to locate a platform using visual cues. The quadrants and visual cues are highlighted by the red lines and circles, respectively. In all cases the animal found the former platform relatively directly, however the overall search behavior after passing this location is different between control and test animals.

In the Morris Water Maze we have discovered a consistent change in behavior in our mutant mice relative to controls. Application of computerized structural characterization methods to search and exploration paths recorded in the Morris

water maze have allowed us to index complex behavior to a quantitative scale. These approaches, originally developed for analysis of non-compact, spatially extended physical structures will advance our understanding of how conditional alteration of the Nlg1 gene affects downstream complex behavior. Methods for characterizing complex data using a small number of important measures are currently used in fields such as ecology, astronomy, bioinformatics, and condensed matter physics [147, 232–234] and we propose to develop similar techniques to describe the searching behavior. These methods may provide two crucial pieces of information currently unavailable or unclear: (i) how the overall behavior of our mutants during the test trial is reliably distinct from control animals and (ii) whether the behavior consistently reflects some knowledge of the specific location of the target. These measures allow us to make more accurate inferences about the state of the memory in these animals, and to better compare specific features of their performance across age and genetic groups. This allows us for the first time to address the interesting possibility that some very specific genetic changes may lead to specific developmental delays in skill acquisition. Furthermore, such quantitative approaches that distill complex behavior during a task into condensed metrics have applications for behavioral tasks beyond the Morris water maze and our work has provided a set of prescriptions for analyzing complex behavioral patterns in general.

Digitial Image Analysis Methods

The Morris water maze experiments were performed in the Washbourne lab. The trials were recorded and commercially available ImagePro Plus image analysis software was used to track the center of mass of the test animal at 0.1 second intervals for a trial time limited to one minute. This data was used to generate a list of 600 coordinates comprising the track of the animal and this was overlaid onto the test space as seen in Figure 2. From the coordinate data we have computed various properties for behavioral characterization. For example, at each of the locations in every track the distance to target, swim speed, and angular difference between direction of motion and direction to the target were measured. For each track the center of mass (COM) and radius of gyration of the track were also measured.

Some measurements require behavioral interpretation in order to compare the results of the measurements across genetic groups and individual animals. For example, the dependence of swim speed on distance from target might indicate the animal is behaving as though searching for the platform in the learned location. A decreasing swim speed at decreasing target distances would indicate that the animal is moving differently (more slowly) near the expected target location. The distribution of angular differences between direction of travel and direction to target might indicate the animal is behaving as though memory of the platform location persists. Peaks in the distribution at 0° and 180° indicates repeated crossing over

the previous platform location and the width of the peaks indicate how sharply the animal is turning back toward this location.

Other measurements require little behavioral interpretation and simply rank the tracks in terms of thier spatial structure and proximity to the target location. For example, the level path dispersion provides information about the spatial distribution of the search pattern while distance between the COM and target location evaluates how accurately the searches are centered on the target location. We can see from qualitative examination of mutant and control tracks, such as those in Figure B.2, that a main difference in the tracks of each group is their spatial distribution. The control tracks appear more clustered and compact while the mutant tracks appeare less clustered and more spatially extended. While both mutant and control mice appear to remember the target location and proceed directly there, once this location is visited the behavior diverges. The controls persist in searching near the target location while the mutants tend to move on and explore and search other areas. This behavior difference leads to the differences in the track distributions we see between groups. In order to study these differences and minimize the need for behavioral interpretation, we measure the track dispersion (lack of clustering). This is quantified by the distribution of two-point distances between track points. The distance, r between each track point and every other point (without double-counting) is computed. The distances are then binned at a $1cm$ interval with the first bin centered at, $r = 0.5cm$. The

bin counts are normalized to the total number of distances measured, equal to $(N-1)(N-2)/2$, where N is the number of track points. Figure B.3 shows three example distributions along with the corresponding search paths.

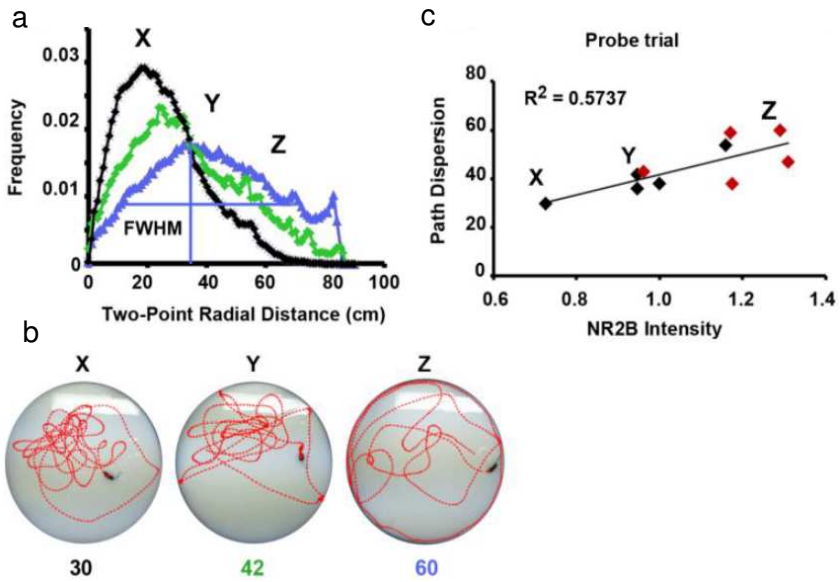

Figure B.3 Panel (a): Two-point distance distributions calculated from the tracks (X, Y, Z) seen in panel (b) and used to calculate the FWHM values of the tracks. Panel (b): Example tracks (X,Y,Z) with values of the FWHM calculated from the distributions in Panel (a). Panel (c): FWHM plotted against normalized NR2B concentration for both mutant and control groups. Figure adapted from reference [229]

The more clustered tracks produce higher, narrower distributions wth peak shifted to smaller separation distance. The less clustered tracks typical of mutants produce wider distributions with lower peaks shifted to larger separation distance. In order to capture this behavior and distill the differences in track clustering down to a single number for comparison across animals and groups we measure the full-width at half-max (FWHM) of the distributions. Larger values indicate

a less clustered more sptatially extended track typical of exploratory rather than focused search behavior. Figure B.3 shows three example tracks along with the corresponding values of the FWHM for each track.

Results

We have hypothesized that the changes in behavior we see are due to diminshed synapse maturation as indicated by relatively large synaptic concentrations of NR2B. Panel (c) of Figure B.3 shows the FWHM measured in probe trials plotted against measured NR2B concentration for both mutant and control animals. We see that the average NR2B level is greater for mutants compared to controls and that the FWHM increases with NR2B. This indicates that as synapse maturity increases the search paths become more clustered. The distance to first cross of the target location, target location dwell times, and number of target location crosses, all show no significant correlation with NRb1 level and we find no significant difference in the average values of these measures between mutant and control groups. This data supports our initial hypothesis that mutant groups are able to learn and remember the target location just as well as control groups and that the difference in their search paths is due to a divergence in behavior after the target location is visted and the platform is found to be absent [229].

Conclusions

Taken together this study indicates that: (I) The diminished synapse maturity found in mutant animals does not affect their ability to learn and remember spatial orientation information. (II) The synaptically immature mutant animals are less likely to persist in searching for the platform when it is found to be absent and they will instead begin to explore the remaining sections of the maze. (III) The lack of persistence in searching near the target location (FWHM) is quantitativly described by the synapse maturity level (NR2B concentration) over the range of levels probed in the study.

Typically, immature (juvenile) animals exhibit greater plasticity in thier behavior relative to adult animals. This leads to faster learning (adaptation) in reversal training for juvenile animals relative to adults. The mutant animals in our study exhibted faster adaptation relative to controls resulting from the divergence of the mutant and control search behavior. The less persistant behavior exhibted by the mutant animals allows them to more quickly discover a new platform location and begin to train for the new location. Examining our data in the context of plasticity, it appears the synaptically immature mutant animals are exhibiting a greater level plasticity typical of juvenile animals without a significant reduction of learning behavior. This work together with the complete muli-scale Neuroligin (NL) study performed by the Washbourne lab and described in reference [229] suggest that cellular processes governed by NL may be linked to both learning and

memory and social behavior. The work descirbed here as well as the complete study have found that disruption of synapse maturation via Nlg1 interference in juveniles leads to adult behavior which is reflective of a juvenile state. This suggests that a Nlg1 mediated behavior maturation process occurs during the juvenile stage of development.

REFERENCES CITED

[1] L. Novotny, Physics Today **64**, 47 (2011).

[2] E. Hecht, *Optics* (Addison Wesley, 2002).

[3] J. D. Jackson, *Classical Electrodynamics* (Wiley, 1999).

[4] S. A. Maier, *Plasmonics Fundamental and Applications* (2007).

[5] M. L. Brongersma and P. G. Kirk, *Surface Plasmon Nanophotonics* (Springer, 2007).

[6] D. K. Gramotnev and S. I. Bozhevolnyi, Nature Photonics **4**, 83 (2010).

[7] S. A. Maier, P. G. Kik, H. A. Atwater, S. Meltzer, E. Harel, B. E. Koel, and A. A. Requicha, Nature Materials **2**, 229 (2003).

[8] N. Fang, H. Lee, C. Sun, and X. Zhang, Science **308**, 534 (2005).

[9] W. L. Barnes, A. Dereux, and T. W. Ebbesen, Nature **424**, 824 (2003).

[10] R. Zia, J. A. Schuller, A. Chandran, and M. L. Brongersma, Materials Today **9**, 20 (2006).

[11] D. E. Chang, A. S. Srensen, E. A. Demler, and M. D. Lukin, Nature Physics **3**, 807 (2007).

[12] E. Ozbay, Science **311**, 189 (2006).

[13] A. M. Gobin, N. J. H. Min Ho Lee, W. D. James, R. A. Drezek, and J. L. West, Nano Letters **7**, 1929 (2007).

[14] K. Kniepp, H. Kniepp, and M. Moskovits, *Surface Enhanced Raman Scattering: Physics and Applications* (Springer, 2006).

[15] M. Grzelczak, J. Perez-Juste, P. Mulvaney, and L. M. Liz-Marza, Chem. Soc. Rev. **37**, 1783 (2008).

[16] M. Rycenga, C. M. Cobley, J. Zeng, W. Li, C. H. Moran, Q. Zhang, D. Qin, and Y. Xia, Chemical Reviews **111**, 3669 (2011).

[17] E. M. Hicks, S. Zou, G. C. Schatz, K. G. Spears, and R. P. V. Duyne, Nano. Lett. **5**, 1065 (2005).

[18] E. Betzig, J. K. Trautman, T. Harris, J. Weiner, and R. Kostelak, Science **251**, 1468 (1991).

[19] N. W. Ashcroft and N. D. Mermin, *Solid State Physics* (Saunders College, 1976).

[20] E. D. Palik, *Handbook of Optical Constants of Solids* (Academic Press, 1988).

[21] H. Raether, *Surface Plasmons on Smooth and Rough Surfaces and on Gratings* (Springer, 1988).

[22] J. Renger, R. Quidant, N. van Hulst, S. Palomba, and L. Novotny, Physical Review Letters **103**, 266802 (2009).

[23] B. Luk'yanchuk, N. I. Zheludev, S. A. Maier, N. J. Halas, P. Nordlander, H. Giessen, and C. T. Chong, Nature Materials **9**, 707 (2010).

[24] J. Homola, *Surface plasmon resonance-based sensors* (Springer Verlag, 2006).

[25] J. A. Dionne, L. A. Sweatlock, H. A. Atwater, and A. Polman, Physical Review B **72**, 075405 (2005).

[26] N. Engheta, Science **317**, 1698 (2007).

[27] T. W. Ebbesen, C. Genet, and S. I. Bozhevolnyi, Physics Today **May**, 44 (2008).

[28] R. Zia, M. D. Selker, P. B. Catrysse, and M. L. Brongersma, Journal of the Optical Society of America **21**, 2442 (2004).

[29] M. Kuttge, E. J. R. Vesseur, J. Verhoeven, H. J. Lezec, H. A. Atwater, , and A. Polman, Applied Physics Letters **93**, 113110 (2008).

[30] A. K. Sharma and B. D. Gupta, Applied Optics **45**, 161 (2006).

[31] W. L. Barnes, Journal of Optics A: Pure and Applied Optics **8**, S87 (2006).

[32] J. Seidel, S. Grafstrm, and L. Eng, Physical Review Letters **94**, 177401 (2005).

[33] M. A. Noginov, G. Zhu, M. Mayy, B. A. Ritzo, N. Noginova, and V. A. Podolskiy, Phys. Rev. Lett. **101**, 226806 (2008).

[34] M. A. Noginov, V. A. Podolskiy, G. Zhu, M. Mayy, M. Bahoura, J. A. Adegoke, B. A. Ritzo, and K. Reynolds, Optics Express **16**, 1385 (2008).

[35] J. Homola, S. S. Yeea, and G. Gauglitzb, Sensors and Actuators B: Chemical **54**, 3 (1999).

[36] J. Homola, Analytical and Bioananalytical Chemistry **377**, 528 (2003).

[37] R. L. Rich and D. G. Myszka, Drug Discovery Today: Technologies **1**, 301 (2004).

[38] J. Homola, Chemical Reviews **108**, 462 (2008).

[39] K. Matsubara, S. Kawata, and S. Minami, Applied Optics **27**, 1160 (1998).

[40] B. Chadwick and M. Gal, Japanese Journal Of Applied Physics Part 1-Regular Papers Short Notes & Review Papers **32**, 2716 (1993).

[41] H. P. Chiang, C. W. Chen, J. J. Wu, H. L. Li, T. Y. Lin, E. J. Sanchez, and P. T. Leung, Thin Solid Films **515**, 6953 (2007).

[42] K. Q. Lin, L. M. Wei, D. G. Zhang, R. S. Zheng, P. Wang, Y. H. Lu, and H. Ming, Chinese Physics Letters **24**, 3081 (2007).

[43] P. R. N. Childs, J. R. Greenwood, and C. A. Long, Review Of Scientific Instruments **71**, 2959 (2000).

[44] L. Davis and M. Deutsch, Review of Sceintific Instruments **81**, 114905 (2010).

[45] H. J. Simon, D. E. Mitchell, and J. G. Watson, Physical Review Letters **33**, 1531 (1974).

[46] J. C. Quail, J. G. Rako, H. J. Simon, and R. T. Deck, Physical Review Letters **50**, 1987 (1983).

[47] T. Y. F. Tsang, Optics Letters **21**, 245 (1996).

[48] V. Shalaev, *Nonlinear Optics of Random Media: Fractal Composits and Metal-Dielectric Films* (Springer, 2000).

[49] J. R. Ferraro, K. Nakoamoto, and C. W. Brown, *Introductory Raman Spectroscopy* (Academic Press, 2003).

[50] A. K. Sarychev and V. M. Shalaev, Physics Reports **335**, 275 (2000).

[51] C. F. Bohren and D. R. Huffman, *Scattering and Absorption of Light by Small Particles* (1998).

[52] R. M. Cole, J. J. Baumberg, F. J. G. de Abaj, S. Mahaja, M. Abdelsalam, , and P. N. Bartlett, Nano Letters **7**, 2094 (2007).

[53] S. Coyle, M. C. Netti, J. J. Baumberg, M. A. Ghanem, P. R. Birkin, P. N. Bartlett, and D. M. Whittaker1, Physical Review Letters **87**, 176801 (2001).

[54] J. H. Kang, D. S. Kim, and Q.-H. Park, Phys **102**, 093906 (2009).

[55] P. G. M. Righini, S. Cherukulappurath, V. Myroshnychenko, F. J. G. de Abajo, and R. Quidan, Nano Letters **9**, 3387 (2009).

[56] Z. Zhu1, T. Zhu, and Z. Liu, Nanotechnology **15**, 357 (2004).

[57] K.-H. Su, Q.-H. Wei, X. Zhang, J. J. Mock, D. R. Smith, and S. Schultz, Nano Letters **3**, 1087 (2003).

[58] A. V. Zayats and I. I. Smolyaninov, Journal of Optics A: Pure and Applied Optics **5**, S16 (2003).

[59] K. Arya, Z. B. Su, and J. L. Birman, Physical Review Letters **54**, 1559 (1985).

[60] X. Luoa and T. Ishihara, Applied Physics Letters **84**, 4780 (2004).

[61] K. L. Norrod, L. M. Sudnik, D. Rousell, and K. L. Rowlen, Applied Spectroscopy **57**, 994 (1997).

[62] G. Watson, P. Fluery, and S. McCall, Physical Review Letters **9**, 945 (1987).

[63] C. M. Aegerter, M. S. S. Fiebig, W. Bhrer, and G. Maret, Journal of the Optical Society of America **27**, A23 (2004).

[64] D. A. G. K. Seal1, A. K. Sarychev, H. Noh, V. M. Shalaev, Z. C. Ying, X. Zhang, and H. Cao, Physical Review Letters **97**, 206103 (2006).

[65] H. Cao, Journal of Physics A Mathematical and General **38**, 10497 (2005).

[66] H.Cao, Y.Ling, J. Xua, A. Burina, and R. Chang, Physica B **338**, 215 (2003).

[67] N. J. Boyrs and J. M. Lupton, The Journal of Physical Chemistry **115**, 13645 (2011).

[68] K. Aslan, J. R. Lakowicz, H. Szmacinski, and C. D. Geddes, Journal of Flourescence **14**, 677 (2004).

[69] Z. Wang and L. Rothberg, Applied Physics B **84**, 289 (2006).

[70] M. S. M. Peterson and M. Deutsch, Journal Of Applied Physics **106**, 063722 (2009).

[71] C. Girard and A. Dereux, Reports on Progress in Physics **59**, 657 (1996).

[72] P. F. Barbara, D. M. Adams, and D. B. OConnor, Annual Reviews of Materials Science **29**, 433 (1999).

[73] F. de Lange, A. Cambi, R. Huijbens, B. de Bakker, W. Rensen, M. Garcia-Parajo, N. van Hulst, and C. G. Figdor, Journal of Cell Science **114**, 4153 (2001).

[74] X. Zheng, W. Xu, C. Corredor, S. Xu, J. An, B. Zhao, and J. R. Lombardi, Journal of Physical Chemistry C **111**, 14962 (2007).

[75] V. A. Khanadeev, B. N. Khlebtsov, S. A. Staroverov, I. V. Vidyasheva, A. A. Skaptsov, E. S. Ileneva, V. A. Bogatyrev, L. A. Dykman, and N. G. Khlebtsov, Journal of Biophotonics **4**, 74 (2011).

[76] K. Aslan, I. Gryczynski, J. Malicka, E. Matveeva, J. R. Lakowicz, and C. D. Geddes, Analytical Biotechnology **16**, 55 (2005).

[77] J. Henson, E. D. J.C. Heckel, J. Abell, A. Bhattacharyya, G. Chumanov, T. D. Moustakas, and R. Paiella, Applied Physics Letters **95**, 151109 (2009).

[78] A. Glass, P. Liao, J. Bergman, , and D. Olson, Optics Letters **5**, 368 (1980).

[79] O. Kulakovich, N. Strekal, A. Yaroshevich, S. Maskevich, S. Gaponenko, I. Nabiev, U. Woggon, and M. Artemyev, Nano Letters **2**, 1449 (2002).

[80] S. Pillai, K. R. Catchpole, T. Trupke, and M. A. Green, Journal Of Applied Physics **101** (2007).

[81] D. Derkacs, S. H. Lim, P. Matheu, W. Mar, and E. T. Yub, Applied Physics Letters **89**, 093103 (2006).

[82] C. D. Geddes and J. R. Lakowicz, Journal of Flourescence **12**, 121 (2002).

[83] J. R. Lakowicz, C. D. Geddes, I. Gryczynski, J. Malicka, Z. Gryczynski, K. Aslan, J. Lukomska, E. Matveeva, J. Zhang, R. Badugu, et al., Journal of Flourescence **14**, 425 (2004).

[84] S. Kim, J. Jin, Y.-J. Kim, I.-Y. Park, Y. Kim, and S.-W. Kim, Nature **453**, 757 (2008).

[85] G. D. Dice, S. Mujumdar, and A. Y. Elezzabi, Applied Physics Letters **86**, 131105 (2005).

[86] N. M. Lawandy, R. Balachandran, A. L. Gomez, and E. Sauvain, Nature **368**, 436 (1994).

[87] H. Z. Wang, F. L. Zhao, Y. J. He, X. G. Zheng, X. G. Huang, and M. M. Wu, Optics Letters **23**, 777 (1998).

[88] W. Kim, V. P. Safonov, V. M. Shalaev, and R. L. Armstrong, Physical Review Letters **82**, 4811 (1999).

[89] K. Aslan, J. R. Lakowicz, and C. D. Geddes, Current Opinion in Chemical Biology **5**, 583 (2005).

[90] A. J. Haes and R. P. V. Duyne, Analytical and Bioanalytical Chemistry **379**, 920 (2004).

[91] L.-K. Chaua, Y.-F. Linb, S.-F. Chenga, and T.-J. Linb, Sensors and Actuators B: Chemical **113**, 100 (2006).

[92] N. J. Florous, K. Saitoh, and M. Koshiba, Ieee Photonics Technology Letters **19**, 324 (2007).

[93] G. T. Boyd, Z. H. Yu, and Y. R. Shen, Physical Review B **33**, 7923 (1986).

[94] N. Kaiser, Applied Optics **41**, 3053 (2002).

[95] C. H. Fan and J. P. Longtin, Journal Of Heat Transfer-Transactions Of The ASME **122**, 757 (2000).

[96] M. Daimon and A. Masumura, Applied Optics **46**, 3811 (2007).

[97] J. Stone, Journal Of The Optical Society Of America **62**, 327 (1972).

[98] J. Sun, J. P. Longtin, and T. F. Irvine, International Journal Of Heat And Mass Transfer **44**, 645 (2001).

[99] D. S. Peterson, T. Rohr, F. Svec, and J. M. J. Frechet, Analytical Chemistry **74**, 4081 (2002).

[100] H. A. Stone, A. D. Stroock, and A. Ajdari, Annual Review Of Fluid Mechanics **36**, 381 (2004).

[101] J. D. Suter, I. M. White, H. Y. Zhu, and X. D. Fan, Applied Optics **46**, 389 (2007).

[102] J. P. Valentino, S. M. Troian, and S. Wagner, Applied Physics Letters **86** (2005).

[103] G. Maltezos, A. Rajagopal, and A. Scherer, Applied Physics Letters **89** (2006).

[104] F. M. Weinert, J. A. Kraus, T. Franosch, and D. Braun, Physical Review Letters **100** (2008).

[105] Kikkeri, R., Laurino, P., Odedra, A., and P. H. Seeberger, Angewandte Chemie-International Edition **49**, 2054 (2010).

[106] S. Koester, F. E. Angile, H. Duan, J. J. Agresti, A. Wintner, C. Schmitz, A. C. Rowat, C. A. Merten, D. Pisignano, A. D. Griffiths, et al., Lab on a Chip **8** (2008).

[107] E. Shapira, D. Marchak, A. Tsukernik, and Y. Selzer, Nanotechnology **19** (2008).

[108] X. Li, Z. Cao, Q. Shen, and Y. Yang, Materials Letters p. 1238 (2006).

[109] F. P. Beer, E. R. Johnston, and J. T. Dewolf, *Mechanics of Materials* (McGaw-Hill, 2004).

[110] B. Frey, D. Leviton, and T. Madison, Tech. Rep. 20070018848, NASA (2007).

[111] A. Lambacher and P. Fromherz, Applied Physics A: Materials Science and Processing **63**, 207 (1996).

[112] C. T. O'Sullivan, American Journal of Physics **58**, 956 (1990).

[113] A. B. Djurisic and B. V. Stanic, Applied Optics **38**, 11 (1999).

[114] A. H. Harvey, J. S. Gallagher, and J. M. H. L. Sengers, Journal Of Physical And Chemical Reference Data **27**, 761 (1998).

[115] A. Chen, K. Hasegawa, V. A. Podolskiy, and M. Deutsch, Optics Letters **32**, 1770 (2007).

[116] D. C. Giancoli, *Physics* (Pearson Education, 2005).

[117] D. L. Powers, *Boundary Value Problems* (Harcourt Academic Press, 1999).

[118] C. Viets and W. Hill, Journal of Physical Chemistry B **105**, 6330 (2001).

[119] M. Peterson, Ph.D. thesis, University of Oregon (2007).

[120] M. Peterson, J. Bouwmana, A.Chen, and M. Deutsch, Journal of Colloid and Interface Science **306**, 41 (2007).

[121] S. I. Bozhevolnyi, V. S. Volkov, and K. Leosson, Physical Review Letters **89** (2002).

[122] H. A. Atwater and A. Polman, Nature Materials **9**, 205 (2010).

[123] M. Moskovits, Reviews of Modern Physics **57**, 784 (1985).

[124] A. Chen, K. Hasegawa, V. A. Podolskiy, and M. Deutsch, Optics Letters **32**, 1770 (2007).

[125] A. Chen and M. Deutsch, Journal of Applied Physics **109**, 093524 (2011).

[126] C. Deumi, R. Richier, P. Dumas, and C. Amra, Applied Optics **35**, 5583 (1996).

[127] T. C. Choy, *Effective Medium Theory: Principles and Applications* (Clarendon Press, 1999).

[128] S. Lowell, J. E. Sheilds, M. A. Thomas, and M. Thommes, *Characterization of Porous Solids and Powders: Surface Area, Pore Size, and Density* (Kluwer, 2004).

[129] J. Rouquerol, D. Avnir, C. Fairbridge, D. Everett, J. Haynes, N. Pernicone, J. Ramsay, K. W. Sing, and K. Unger, Tech. Rep., International Union of Pure and Applied Chemistry (1994).

[130] H. Yasuda and J. T. Tsai, Jounral of Applied Polymer Science **18**, 805 (2003).

[131] V. Lysenko, J. Vitiello, B. Remaki, and D. Barbier, Physical Review E **70**, 017301 (2004).

[132] S. Ozawa, Y. Sasajima, and D. W. Heermann, Thin Solid Films **272**, 172 (1996).

[133] G. H. Gilmer, H. Huang, T. D. de la Rubia, J. D. Torre, and F. Baumann, Thin Solid Films **365**, 189 (2000).

[134] H. Huang, G. H. G. , and T. D. de la Rubia, Journal of Applied Physics **84**, 3636 (1998).

[135] K. F. Jenson, S. T. Rogers, and R. Venkatarami, Current Opinion in Solid State and Materials Science **3**, 562 (1998).

[136] P. Bruschi, P. Cagnoni, and A. Nannini, Physical Review B **55**, 7955 (55).

[137] P. Bruschi, A. Nannini, and F. Pieri, Physical Reveiw B **63**, 035406 (2000).

[138] R. Hrach, J. Simek, and M. Kostern, Vacuum **67**, 229 (2002).

[139] S. Mao and A. G. Journel, Computers and Geosciences **25**, 845 (1999).

[140] . Kyl, G. Faeth, T. Farias, and M. Carvalho, Combustion and Flame **100**, 621 (1995).

[141] D. Novotny and R. Hrach, Vacuum **84**, 266 (2010).

[142] R. Hrach, J. Simek, and M. Kostern, Vacuum **67**, 229 (2002).

[143] Z. Zhang and M. G. Lagally, Science **18**, 377 (1997).

[144] D. L. V. Hyning, W. G. Klemperer, and C. F. Zukoski, Langmuir **17**, 3128 (2001).

[145] F. Spaepen, Acta Materialia **48**, 31 (2000).

[146] R. Carel, C. Thompson, and H. Frost, Acta Materialia **44**, 2479 (1996).

[147] D. Stauffer, Physical Review Letters **41**, 1333 (1978).

[148] C. Thompson and R. Carel, Materials Science and Engineering: B **32**, 211 (1995).

[149] C. Friesen and C. Thompson, Physical Review Letters **89**, 123103 (2002).

[150] R. Koch, D. Hu, and A. K. Das, Physical Review Letters **94**, 146101 (2005).

[151] J. E. Griffith, D. A. Grigg, M. J. Vasile, P. E. Russell, and E. A. Fitzgerald, Journal of Vacuum Science and Technology **10**, 674 (1992).

[152] G. T. Boyd, T. Rasing, J. R. R. Leite, and Y. R. Shen, Phys. Rev. B **30**, 519 (1984).

[153] K. Seal, M. A. Nelson, Z. C. Ying, D. A. Genov, A. K. Sarychev, and V. M. Shalaev, Physical Reveiw B **67**, 035318 (2002).

[154] W. Cai and V. Shalaev, *Optical Metamaterials: Fundamentals and Applications* (Springer, 2010).

[155] D. Bruggeman, Annalen Der Physik **6736**, 24 (1935).

[156] A. Shwartzberg and J. Zhang, Journal of Physical Chemistry C **112**, 10323 (2008).

[157] D. A. Weitz, S. Garoff, C. D. Hanson, T. J. Gramila, and J. I. Gersten, Optics Letters **7**, 89 (1982).

[158] R. M. Amos and W. L. Barnes, Physical Review B **59**, 7708 (1999).

[159] E. Dulkeith, M. Ringler, T. Klar, J. Feldmann, A. M. Javier, and W. J. Parak, Nano Letters **5**, 585 (2005).

[160] L. Peyser, A. Vinson, A. Bartko, and R. Dickson, Science **5**, 103 (2001).

[161] T. Gleitsmann, T. M. Bernhardt, and L. Oste, Applied Physics A: Materials Science and Processing **82**, 125 (2006).

[162] T. Gleitsmann, B. Stegemann, and T. M. Bernhardt, Applied Physics Letters **84**, 4050 (2004).

[163] J. Wilcoxon, J. Martin, F. Parsapour, B. Wiedenman, and D. Kelley, Journal of Chemical Physics **108**, 9137 (1998).

[164] J. Zheng, Y. Ding, B. Tian, Z. Wang, and X. Zhuang, Journal of the American Chemical Society **130**, 10472 (2008).

[165] C. D. Geddes, A. Parfenov, I. Gryczynski, and J. R. Lakowicz, Journal of Physical Chemistry B **107**, 9989 (2003).

[166] C. D. Geddes, A. Parfenov, I. Gryczynski, and J. R. Lakowicz, Chemical Physics Letters **380**, 269 (2003).

[167] A. Mooradian, Phsyical Review Letters **22**, 185 (1969).

[168] P. Apell and R. Monreal, Physica Scripta **38**, 174 (1988).

[169] E. Dulkeith, T. Niedereichholz, T. A. Klar, J. Feldmann, G. von Plessen, D. I. Gittins, K. S. Mayya, , and F. Caruso, Physical Reveiw B **70**, 205424 (2004).

[170] C. Blaul, Master's thesis, Technical Universtiy of Dresden (2009).

[171] C. Berglund and W. E. Spicer, Physical Review A **136**, 1044 (1964).

[172] H. Ehrenreich and H. R. Philip, Physical Review **128**, 1622 (1962).

[173] S. Link, A. Beeby, S. FitzGerald, M. A. El-Sayed, T. G. Schaaff, and R. L. Whetten, Journal of Physical Chemistry B **106**, 3410 (2002).

[174] J. Zheng, C. Zhang, and R. M. Dickson, Physical Review Letters **93**, 077402 (2004).

[175] J. Zheng, P. R. Nicovich, and R. M. Dickson, Annual Reveiw of Physical Chemistry **58**, 409 (2007).

[176] S. Link, A. Beeby, S. FitzGerald, M. A. El-Sayed, T. G. Schaaff, and R. L. Whetten, Journal of Physical Chemistry B **106**, 3410 (2002).

[177] A. Varkey and A. Fort, Solar Energy Materials and Solar Cells **29**, 253 (1993).

[178] B. Pettinger, M. R. Philpott, and I. J. G. Gordon, Journal of Chemical Physics **74**, 934 (1981).

[179] S. C. Kitson, P. Jonsson, J. G. Rarity, and P. R. Tapster, Physical Review A **58**, 620 (1998).

[180] T. Ha, S. A. McKinney, and I. Rasnik, Nature Methods **3**, 891 (2006).

[181] M. Pelton, D. G. Grier, and P. Guyot-Sionnest, Applied physics letters **85**, 819 (2004).

[182] S. Bretschneider, C. Eggeling, and S. W. Hell, Physical Review Letters **98**, 218103 (2007).

[183] T. A. Baker, J. L. Rouge, and D. J. Nesbitt, Molecular Physics **107**, 1867 (2009).

[184] C. Galland, Y. Ghosh, A. Steinbrck, M. Sykora, J. A. Hollingsworth, V. I. Klimov, and H. Htoon, Nature **479**, 203 (2011).

[185] Z. Wang and L. J. Rothberg, Journal of Physical Chemistry B **109**, 3387 (2005).

[186] S. R. Emory, R. A. Jense, T. Wenda, M. Hanb, and S. Nie, Faraday Discussions **132**, 249 (2006).

[187] Y. Maruyama, M. Ishikawa, and M. F. and, Jounral of Physical Chemisty B **108**, 673 (2004).

[188] J. Widengren and R. Rigler, Bioimaging **4**, 149 (1996).

[189] A. Weiss and G. Haran, Journal of Physical Chemistry B **105**, 12348 (2001).

[190] M. J. Walter, N. J. Borys, G. Gaefke, S. Hoger, and J. M. Lupton, Journal of the American Chemical Society **130**, 16830 (2008).

[191] R. L. Price and W. G. Jerome, eds., *Basic Confocal Microscopy* (Springer, 2011).

[192] I. D. Wolf, Semiconductor Science and Technology **11**, 139 (1996)).

[193] P. J. Moyer, J. Schmidt, L. M. Eng, and A. J. Meixner, Journal of the American Chemical Society **122**, 5409 (2000).

[194] B. Sheldon, K. Lau, and A. Rajamani, Journal of Applied Physics **90**, 5097 (2001).

[195] B. B. Mandelbrot, *The Fracal Geometry of Nature* (W.H. Freeman, 1977).

[196] P. Zhang, T. Haslett, C. Douketis, and M. Moskovits, Physical Reveiw B **57**, 15513 (1998).

[197] E. Hao and G. C. Schatz, Journal of Chemical Physics **120**, 357 (2004).

[198] Z. Wang, S. Pan, T. Krauss, H. Du, and L. Rothberg, Proceedings of the National Academy of Sciences **100**, 8639 (2003).

[199] T. Q. Y. Zhou, J. Li, W. Zhang, X. Lang, T. Cui, and P. K. Chu, Journal of Physics D: Applied Physics **42**, 175403 (2009).

[200] R. Alvarez-Puebla, L. M. Liz-Marzan, and F. J. G. de Abajo, The Journal of Physical Chemistry Letters **16**, 2428 (2010).

[201] T. Okamoto and lchirou Yamagchi, Optical Review **6**, 211 (1999).

[202] A. Sundaramurthy, K. B. Crozier, , G. S. Kino, D. P. Fromm, P. J. Schuck, and W. E. Moerner, Physical Reveiw B **72**, 165409 (2005).

[203] T. Soga, ed., *Nanostructured Materials for Solar Energy Conversion* (Springer, 2006).

[204] P. P. Pompa, L. Martiradonna, A. D. Torre, F. D. Sala, L. Manna, M. D. Vittorio, F. Calabi, R. Cingolani, and R. Rinaldi, Nature Nanotechnology **1**, 126 (2006).

[205] M. Nilsson, S. Waters, N. Waters, A. Carlsson, and M. L. Carlsson, Journal of Neural Transmission **108**, 1181 (2001), ISSN 0300-9564, 10.1007/s007020170008.

[206] T. Sigurdsson, K. L. Stark, M. Karayiorgou, J. A. Gogos, and J. A. Gordon, Nature **464**, 763 (2010), ISSN 0028-0836.

[207] H. Y. Zoghbi, Science **302**, 826 (2003), `http://www.sciencemag.org/cgi/reprint/sci;302/5646/826.pdf`.

[208] S. Cull-Candy, S. Brickley, and M. Farrant, Current Opinion in Neurobiology **11**, 327 (2001), ISSN 0959-4388.

[209] C. Betancur, T. Sakurai, and J. D. Buxbaum, Trends in Neurosciences **32**, 402 (2009), ISSN 0166-2236.

[210] S. Jamain, H. Quach, C. Betancur, M. Rstam, C. Colineaux, C. Gillberg, H. Sderstrm, B. Giros, M. Leboyer, C. Gillberg, et al., Nature Genetics **34**, 27 (2003).

[211] B. Chih, S. K. Afridi, L. Clark2, and P. Scheiffele, Human Molecular Genetics **13**, 1471 (2004).

[212] B. Chih, H. Engelman, and P. Scheiffele, Science **307**, 1324 (2005), http://www.sciencemag.org/cgi/reprint/sci;307/5713/1324.pdf.

[213] J. Kim, S.-Y. Jung, Y. K. Lee, S. Park, J.-S. Choi, C. J. Lee, H.-S. Kim, Y.-B. Choi, P. Scheiffele, C. H. Bailey, et al., Proceedings of the National Academy of Sciences **105**, 9087 (2008), http://www.pnas.org/content/105/26/9087.full.pdf+html.

[214] E. de Villers-Sidani, K. L. Simpson, Y.-F. Lu, R. C. S. Lin, and M. M. Merzenich, Nat Neurosci **11**, 957 (2008), ISSN 1097-6256.

[215] D. E. Feldman, R. A. Nicoll, R. C. Malenka, and J. T. Isaac, Neuron **21**, 347 (1998), ISSN 0896-6273.

[216] T. K. Hensch and M. Fagiolini, in *Development, Dynamics and Pathiology of Neuronal Networks: from Molecules to Functional Circuits*, edited by C. L. A. v. O. G. R. J. van Pelt, M. Kamermans and P. Roelfsema (Elsevier, 2005), vol. 147 of *Progress in Brain Research*, pp. 115 – 124.

[217] B. M. Hooks and C. Chen, Neuron **56**, 312 (2007), ISSN 0896-6273.

[218] T. Iwasato, A. Datwani, A. M. Wolf, H. Nishiyama, Y. Taguchi, S. Tonegawa, T. Knopfel, R. S. Erzurumlu, and S. Itohara, Nature **406**, 726 (2000), ISSN 0028-0836.

[219] F. M. Richardson and M. S. Thomas, Developmental Science **11**, 371 (2008), ISSN 1467-7687.

[220] X. Zhou and M. M. Merzenich, Proceedings of the National Academy of Sciences **105**, 4423 (2008), http://www.pnas.org/content/105/11/4423.full.pdf+html.

[221] M. Mayford, M. E. Bach, Y.-Y. Huang, L. Wang, R. D. Hawkins, and E. R. Kandel, Science **274**, 1678 (1996), http://www.sciencemag.org/content/274/5293/1678.full.pdf.

[222] S. Kim, A. Burette, H. S. Chung, S.-K. Kwon, J. Woo, H. W. Lee, K. Kim, H. Kim, R. J. Weinberg, and E. Kim, Nat Neurosci **9**, 1294 (2006), ISSN 1097-6256.

[223] B. Scholl and M. Wehr, Journal of Neurophysiology **100**, 646 (2008), http://jn.physiology.org/content/100/2/646.full.pdf+html.

[224] M. Wehr and A. M. Zador, Nature **426**, 442 (2003).

[225] L. Schimanski and P. Nguyen, Neuroscience & Biobehavioral Reviews **28**, 463 (2004), ISSN 0149-7634.

[226] C. V. Vorhees, H. L. Johnson, L. N. Burns, and M. T. Williams, Neurotoxicology and Teratology **31**, 1 (2009), ISSN 0892-0362.

[227] C. V. Vorhees and M. T. Williams, Nat. Protocols **1**, 848 (2006), ISSN 1754-2189.

[228] D. Zamanillo, R. Sprengel, i. Hvalby, V. Jensen, N. Burnashev, A. Rozov, K. M. M. Kaiser, H. J. Kster, T. Borchardt, P. Worley, et al., Science **284**, 1805 (1999), `http://www.sciencemag.org/content/284/5421/1805.full.pdf`.

[229] J. L. Hoy, Ph.D. thesis, University of Oregon (2011).

[230] M. Dolleman-van der Weel, R. Morris, and M. Witter, Brain Structure and Function **213**, 329 (2009), ISSN 1863-2653, 10.1007/s00429-008-0200-6.

[231] P. E. Chen, M. L. Errington, M. Kneussel, G. Chen, A. J. Annala, Y. H. Rudhard, G. F. Rast, C. G. Specht, C. M. Tigaret, M. A. Nassar, et al., Learning & Memory **16**, 635 (2009), `http://learnmem.cshlp.org/content/16/10/635.full.pdf+html`.

[232] K. H. Riitters, R. V. O'Neill, C. T. Hunsaker, J. D. Wickham, D. H. Yankee, S. P. Timmins, K. B. Jones, and B. L. Jackson, Landscape Ecology **10**, 23 (1995), ISSN 0921-2973, 10.1007/BF00158551.

[233] C. Rth, P. Schuecker, and A. J. Banday, Monthly Notices of the Royal Astronomical Society **380**, 466 (2007), ISSN 1365-2966.

[234] D. Reich, A. L. Price, and N. Patterson, Nat Genet **40**, 491 (2008), ISSN 1061-4036.